



LUND UNIVERSITY

Transmission Electron Tomography and In-situ Analysis of Nanowires

Persson, Axel

2020

Document Version:

Publisher's PDF, also known as Version of record

[Link to publication](#)

Citation for published version (APA):

Persson, A. (2020). *Transmission Electron Tomography and In-situ Analysis of Nanowires*. [Doctoral Thesis (compilation), Faculty of Engineering, LTH]. Department of Chemistry, Lund University.

Total number of authors:

1

Creative Commons License:

Unspecified

General rights

Unless other specific re-use rights are stated the following general rights apply:

Copyright and moral rights for the publications made accessible in the public portal are retained by the authors and/or other copyright owners and it is a condition of accessing publications that users recognise and abide by the legal requirements associated with these rights.

- Users may download and print one copy of any publication from the public portal for the purpose of private study or research.
- You may not further distribute the material or use it for any profit-making activity or commercial gain
- You may freely distribute the URL identifying the publication in the public portal

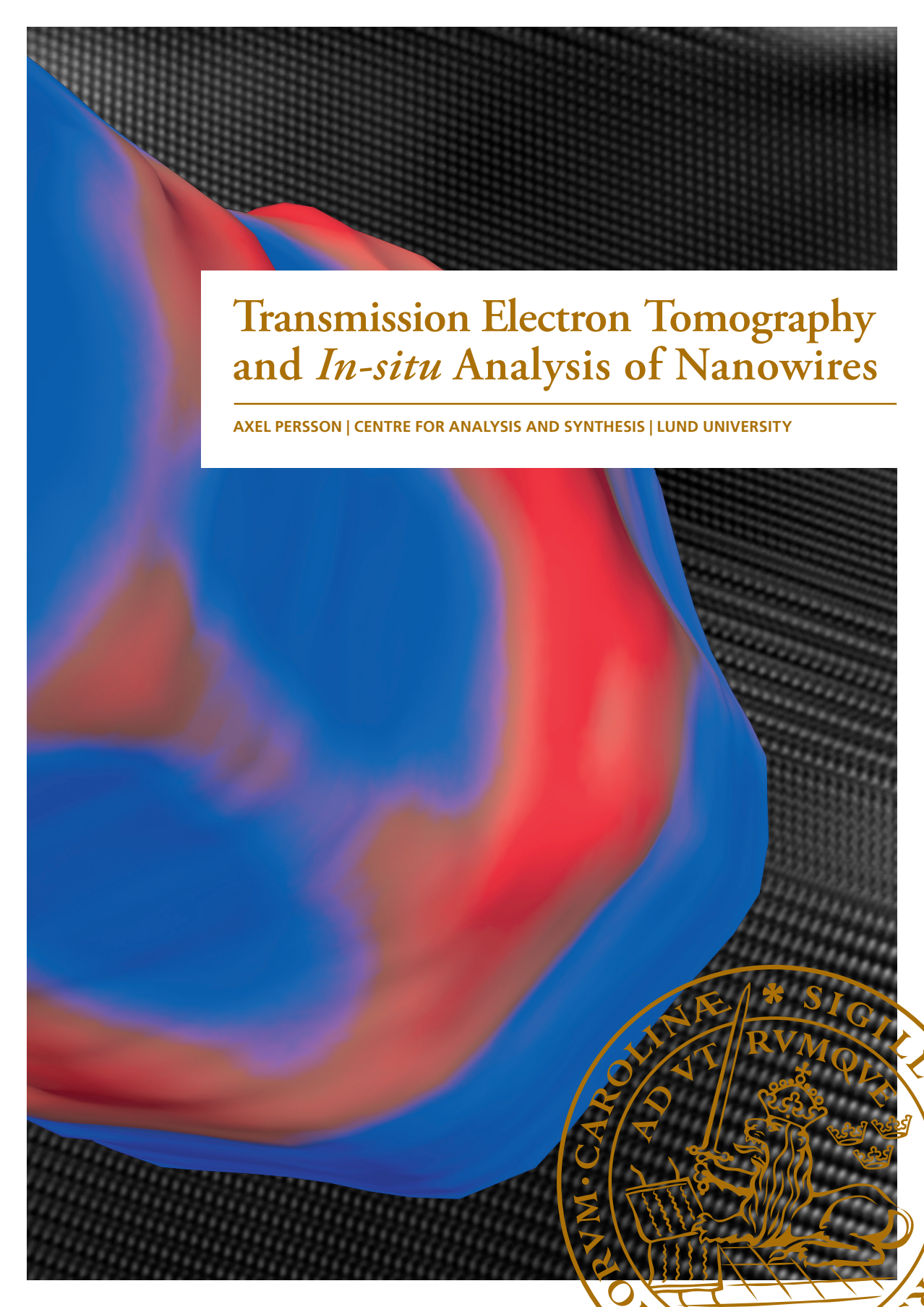
Read more about Creative commons licenses: <https://creativecommons.org/licenses/>

Take down policy

If you believe that this document breaches copyright please contact us providing details, and we will remove access to the work immediately and investigate your claim.

LUND UNIVERSITY

PO Box 117
221 00 Lund
+46 46-222 00 00

The background of the cover features a transmission electron microscopy (TEM) image of a nanowire, showing a regular grid of atoms. Overlaid on this is a 3D reconstruction of the nanowire's internal structure, rendered in shades of blue and red to represent different atomic species or phases. The reconstruction shows a complex, layered internal structure.

Transmission Electron Tomography and *In-situ* Analysis of Nanowires

AXEL PERSSON | CENTRE FOR ANALYSIS AND SYNTHESIS | LUND UNIVERSITY



Transmission Electron Tomography and *In-situ* Analysis of
Nanowires

Transmission Electron Tomography and *In-situ* Analysis of Nanowires

by Axel Persson



LUND
UNIVERSITY

Thesis for the degree of PhD
Thesis advisors: Professor Reine Wallenberg,
Associate Professor Martin Magnusson
Faculty opponent: Dr. Martien den Hertog

To be presented at Kemicentrum, Department of Chemistry, lecture hall KC:B
on Friday, the 27th of March 2020 at 13:15.

Visiting address: Naturvetarvägen 14, SE-223 62 Lund

Transmission Electron Tomography and *In-situ* Analysis of Nanowires

by Axel Persson



LUND
UNIVERSITY

A doctoral thesis at a university in Sweden takes either the form of a single, cohesive research study (monograph) or a summary of research papers (compilation thesis), which the doctoral student has written alone or together with one or several other author(s).

In the latter case, the thesis consists of two parts. An introductory text puts the research work into context and summarizes the main points of the papers. Then, the research publications themselves are reproduced, together with a description of the individual contributions of the authors. The research papers may either be manuscripts at various stages (in press, submitted, or in draft) or already published.

Cover illustration front: A spaceship towards the stars. A 3D reconstructed core–shell–shell nanowire (InAs–AlSb–InAs) is shown in color depending on the thickness of the outer InAs layer (blue: thinner, red: thicker). The background is a HRTEM micrograph of a WZ (InAs) to ZB (InGaAsSb) transition in a nanowire.

Cover illustration back: The difficulty of presenting multidimensional data in print. The data-cube contains information from figure 5.7 in chapter 5 (the top of a GaAs nanowire) and the planar dimensions represent the spatial dimensions of the spectrum image. Each colored layers' intensity represent the amount of that element/component is needed to explain a spatial point. Blue: background, green: Cu, purple: Ga, red: As and yellow: Au.

Funding information: The thesis work was financially supported by Knut and Alice Wallenberg foundation (KAW), Energimyndigheten and NanoLund.

Disclaimer: Parts of the thesis work presented here have been presented in a Licentiate thesis at the half-time point of the project. Figures or tables used here which are adapted from that thesis reference the publication in their captions.

© Axel Persson 2020

Faculty of Engineering, Department of Chemistry

ISBN: 978-91-7422-720-8 (print)

ISBN: 978-91-7422-721-5 (pdf)

Printed in Sweden by Media-Tryck, Lund University, Lund 2020



Media-Tryck is a Nordic Swan Ecolabel certified provider of printed material. Read more about our environmental work at www.mediatryck.lu.se

MADE IN SWEDEN 

"Your focus determines your reality"
– Qui-Gon Jinn, *Star Wars Episode I: The Phantom Menace*

"In my experience there is no such thing as luck"
– Obi-Wan Kenobi, *Star Wars Episode IV: A New Hope*

"Stay on target."
– Davish Krail, as Gold Five, *Star Wars Episode IV: A New Hope*

Acknowledgments

It might seem like an obligatory or forced section of a thesis to thank one's supervisors and colleagues. No matter how obligatory, it is of course one of the more important ones. Four and a half years would have been a long time performing research, laboratory work and long hours of writing without the support of knowledgeable and fun people around.

First and foremost, I would like to thank my supervisor **Reine**, who for some reason invited that student who via email from far away asked if it was possible to arrange some sort of summer-project at the electron microscopes. Said and done, you basically left me with a SEM for the summer, followed by a Master's project and now doctoral studies involving the TEMs. I do not know why you trusted me with these instruments from the start, but I am very grateful for the opportunity. Thank you for all the input about everything. No matter at what time during the day or week or how closed your door was, you have always been there with comments on grammar, colors (especially red or green) and what not.

Thank you also **Martin M.**, my co-supervisor who always have valuable input and interesting projects going. Administration around my studies has never been an issue, oh well, unless I've created them myself, with you two as supervisors.

The team at nCHREM, you have been great to work with. **Crispin**, your knowledge about the TEMs is unbeatable and if you by chance do not know about something, I bet you can find it in any lexicon, no matter its state or age. **Daniel** and **Anna**, thank you for the help and discussions about the microscopes and making my work possible. *The force will be with you, always.* My partner in crime at the ETEM, **Marcus**, thanks for joining the Jedi academy and using, if not the force at least airplanes and trains to join me in Sydney and Gothenburg. Thank you to **Carina**, **Robin** and **Kimberly** for interesting collaborations in the world of nanowires and *in-situ*. Also thank you to **Martin E.** and **Filip** for discussions about the microscopes as well as **Sudha** and **Wondwosen** for the discussions about Aerotaxy. Collaboration-wise, this section would fill the pages with names if I would name everyone. Instead, I thank you collectively. It has been a pleasure and a privilege doing microscopy in all these projects covering varying fields, all in need of electron microscopy. Thanks also to **Jonas** for the assistance with the 3D graphics, including the front cover page of this thesis.

Thank you to the department, CAS and Polymat, for the endless sources of discussions and coffee, especially **Joel**, **Laura**, **Hannes** and **Huong** who I have joined forces with the longest. Also, thank you to Dr Nano, the not so small lunch crew: **Anders**, **Axel**, **Calle**, **Emil**, **Malin**, **Martin J.**, **Mårten** and **Sara**. For some of you it's getting close to

finalizing your PhDs and others have some time left or are already done, best of luck to you all.

When not staring at computer screens, green fluorescent light in dark rooms or waiting for computers to do calculations, there will always be time for musical activities. Thank you **Folktetten** for letting me be a part of the gang, performing at pubs and churches as if there were no differences (well, some), dreaming about Germany or skiing. And of course, as tradition dictates:

HEJA ESLÖV! (with no further explanation needed)

A big thank you to my family, relatives and other friends for support. I hope this pamphlet could come in use, either as weight on the bookshelf, propping up unstable tables or actually explaining something about what I've been doing. Of course also, **Emma**. With such a large supporting role in the research, you might be asked questions. I guess now you can refer to this text and not: "[something something] inorganic chemistry". I think you know your importance to me, both for making this possible and everything else.

Contents

Acknowledgments	i
List of publications	v
Popular summary in English	ix
Populärvetenskaplig sammanfattning på svenska	xi
List of acronyms and abbreviations	xiii
1 Introduction	1
1.1 Research hypothesis and the layout of the thesis	2
1.2 An introduction to semiconductors	3
1.3 Electron microscopes and what they are good for	4
2 III–V semiconducting nanowires and their growth	7
2.1 Semiconductors	7
2.2 Crystal structure of III–V semiconductors	10
2.3 Nanowires	12
2.4 Nanowire growth methods	13
3 Transmission electron microscopy	19
3.1 The microscope	19
3.2 Produced signals	22
3.3 High-resolution TEM	22
3.4 Aberrations and correction of these	25
3.5 Scanning TEM	27
3.6 Sample preparation	29
3.7 Compositional analysis	29
3.8 <i>In-situ</i> TEM	30
4 Electron tomography	33
4.1 The principle of tomography	33
4.2 Algorithms	36
4.3 Problems with tomography in the TEM	40
4.4 Signals used for reconstruction	40
4.5 Post-processing	41
5 Compositional mapping with short acquisitions	43

5.1	The idea	44
5.2	The method described in steps	45
5.3	Simulations	46
5.4	Results and discussion of measurements	49
6	Discussion and outlook	53
6.1	High resolution and compositional data of nanowires	53
6.2	<i>In-situ</i> studies of nanowire growth	55
6.3	Electron tomography of nanowires	58
6.4	Conclusions	60
6.5	Outlook	62
	References	65
	Scientific publications	75
	My contributions	75
	Paper I: Electron tomography reveals the droplet covered surface structure of nanowires grown by Aerotaxy	77
	Paper II: Kinetic engineering of wurtzite and zinc-blende AlSb shells on InAs nanowires	87
	Paper III: Kinetics of Au-Ga Droplet Mediated Decomposition of GaAs Nanowires	97
	Paper IV: In situ analysis of catalyst composition during gold catalyzed GaAs nanowire growth	107
	Paper V: Independent control of nucleation and layer growth in nanowires	119
	Paper VI: GaAsP Nanowires Grown by Aerotaxy	139
	Paper VII: <i>n</i> -type doping and morphology of GaAs nanowires in Aerotaxy .	149
	Appendix	159

List of publications

This thesis is based on the following publications, referred to by their roman numerals:

- I **Electron tomography reveals the droplet covered surface structure of nanowires grown by Aerotaxy**
Axel R. Persson, Wondwosen Metaferia, Sudhakar Sivakumar, Lars Samuelson, Martin H. Magnusson, L. Reine Wallenberg
Small 14 (2018) 1801285
- II **Kinetic engineering of wurtzite and zinc-blende AlSb shells on InAs nanowires**
Hanna Kindlund, Reza R. Zamani, Axel R. Persson, Sebastian Lehmann, L. Reine Wallenberg, Kimberly A. Dick
Nano Letters 18 (2018) 5775-5781
- III **Kinetics of Au-Ga Droplet Mediated Decomposition of GaAs Nanowires**
Marcus U. Tornberg, Daniel Jacobsson, Axel R. Persson, L. Reine Wallenberg, Kimberly A. Dick, Suneel Kodambaka
Nano Letters 19 (2019) 3498-3504
- IV **In situ analysis of catalyst composition during gold catalyzed GaAs nanowire growth**
Carina B. Maliakkal, Daniel Jacobsson, Marcus Tornberg, Axel R. Persson, Jonas Johansson, Reine Wallenberg, Kimberly A. Dick
Nature Communications 10 (2019) 4577
- V **Independent control of nucleation and layer growth in nanowires**
Carina B. Maliakkal, Erik K. Mårtensson, Marcus Tornberg, Daniel Jacobsson, Axel R. Persson, Jonas Johansson, Reine Wallenberg, Kimberly A. Dick
Submitted to ACS Nano. arXiv: 1905.08225 [physics. app-ph]

VI **GaAsP Nanowires Grown by Aerotaxy**

Wondwosen Metaferia, **Axel R. Persson**, Kilian Mergenthaler, Fangfang Yang, Wei Zhang, Arkady Yartsev, Reine Wallenberg, Mats-Erik Pistol, Knut Deppert, Lars Samuelson, Martin H. Magnusson
Nano Letters **16** (2016) 5701-5707, ACS AuthorChoice - Open Access

VII **n-type doping and morphology of GaAs nanowires in Aerotaxy**

Wondwosen Metaferia, Sudhakar Sivakumar, **Axel R. Persson**, Irene Geijsselaers, Reine Wallenberg, Knut Deppert, Lars Samuelson, Martin H. Magnusson
Nanotechnology **29** (2018) 285601

All papers are reproduced with permission of their respective publishers.

Publications which I contributed to but are outside the scope and not included in this thesis:

Individual Defects in InAs/InGaAsSb/GaSb Nanowire Tunnel Field-Effect Transistors Operating below 60 mV/decade

Elvedin Memisevic, Markus Hellenbrand, Erik Lind, Axel R. Persson, Saurabh Sant, Andreas Schenk, Johannes Svensson, Reine Wallenberg, Lars-Erik Wernersson

Nano Letters 17 (2017) 4373-4380

Vertical InAs/InGaAs Heterostructure Metal–Oxide–Semiconductor Field-Effect Transistors on Si

Olli-Pekka Kilpi, Johannes Svensson, Jun Wu, Axel R. Persson, Reine Wallenberg, Erik Lind, Lars-Erik Wernersson

Nano Letters 17 (2017) 6006-6010

Polymer-supported palladium (II) carbene complexes: catalytic activity, recyclability and selectivity in C-H acetoxylation of arenes

Maitham H. Majeed, Payam Shayesteh, Reine Wallenberg, Axel R. Persson, Niclas Johansson, Lei Ye, Joachim Schnadt, Ola F. Wendt

Chemistry-A European Journal 23 (2017) 8457-8465

A PdII Carbene Complex with Anthracene Side-Arms for π -Stacking on Reduced Graphene Oxide (rGO): Activity towards Undirected C-H Oxygenation of Arenes

Maitham H. Majeed, Payam Shayesteh, Axel R. Persson, L. Reine Wallenberg, Joachim Schnadt, Ola F. Wendt

European Journal of Inorganic Chemistry 43 (2018) 4742-4746

In situ XAS study of the local structure and oxidation state evolution of palladium in a reduced graphene oxide supported Pd(ii) carbene complex during an undirected C-H acetoxylation reaction

Ning Yuan, Maitham H. Majeed, Éva G. Bajnóczi, Axel R. Persson, L. Reine Wallenberg, A. Ken Inge, Niclas Heidenreich, Norbert Stock, Xiaodong Zou, Ola F. Wendt, Ingmar Persson

Catalysis Science & Technology 9 (2019) 2025-2031

Template-assisted vapour–liquid–solid growth of InP nanowires on (001) InP and Si substrates

Reza Jafari Jam, **Axel R. Persson**, Enrique Barrigón, Magnus Heurlin, Irene Geijselaers, Víctor J. Gómez, Olof Hultin, Lars Samuelson, Magnus T. Borgström, Håkan Pettersson

Nanoscale 12 (2020) 888-894

Directed C–H Halogenation Reactions Catalysed by PdII Supported on Polymers under Batch and Continuous Flow Conditions

Maitham H. Majeed, Payam Shayesteh, Per Tunå, **Axel R. Persson**, Roman Gritcenko, L. Reine Wallenberg, Lei Ye, Christian Hulteberg, Joachim Schnadt, Ola F. Wendt

Chemistry–A European Journal 25 (2019) 13591-13597

Observing growth under confinement: Sn nanopillars in porous alumina templates

Gary S. Harlow, Jakub Drnec, Tim Wiegmann, Weronica Lipé, Jonas Evertsson, **Axel R. Persson**, Reine Wallenberg, Edvin Lundgren, Nikolay A. Vinogradov

Nanoscale Advances 1 (2019) 4764-4771

Popular summary in English

When producing something, anything at all, the result should ideally match the intended object. Perhaps the object should have a certain mechanical strength, have a certain color or possibly conduct electricity? Electrical components, which become smaller and smaller over time, are very sensitive to minute variations in the material. This requires precise control over their production. The composition of materials, for example, can dictate how well the material conducts electricity and its efficiency when used, for instance in solar cells or light emitting diodes (LED). This thesis deals with the analysis of small electrical components where I have imaged the positioning of their atoms, their crystal structure, and the concentrations of individual elements within. I have both studied the process when these are produced and recreated 3D images of the structures. This has led to insights into how quickly processes occur, local concentrations of elements and how these changes when parameters during production. Such parameters can be temperature and flow of material. The 3D images have given more information on how shapes and surfaces have been affected by these parameters. Illustrating images are shown in figure 1 on page x.

When electronic components reduce in size, single atoms play a larger role in the properties of the component. This further increases the quality demands of the production. A method of producing such small components is to grow the material in the form of thin wires. These *nanowires*' diameters, consisting of a couple of hundred to several thousand atoms, are in the nanometer range (one nanometer = a billionth of a meter) (see an example in figure 1c). The process of growing these is very complex and small changes can lead to completely different nanowires, both in their crystal structure and composition. This motivates the need of studying the nanowires at the atomic level to be able to find parameters producing the wires with the properties sought.

Since regular light-microscopes are limited in resolution, we instead use electrons that have much shorter wavelength (the otherwise limiting factor). Specifically, I have used so called transmission electron microscopy (TEM) (figure 1a). In TEM we send electrons through our sample and detect what is passing through on the other side. The image created has a very high resolution and it is possible to see the atoms (figures 1c-d). Modern TEMs have a point resolution better than one Ångström (a tenth of a nanometer), which is clearly useful. I have used two special types of TEM to study the nanowires: to produce the wires inside the TEM and *filming in-situ* at high resolution, and analyzing the composition at the same time. Also reconstructions of wires in three dimensions (*electron tomography*, figure 1b) were performed.

The studies in this thesis are important for gaining more knowledge of the nanowires and how to optimally grow them, optimization which allows for fine-tuning of their properties. The use and development of the different TEM techniques also highlights their advantages, disadvantages and how they can provide information, not only for nanowire applications, but also other materials.

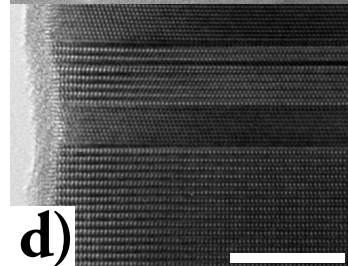
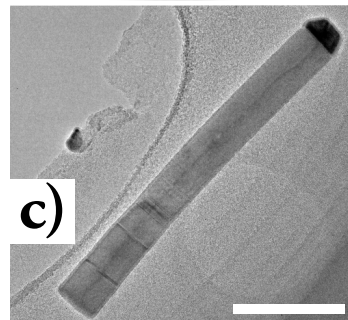
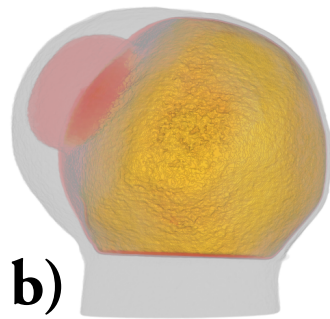


Figure 1 (English): From meters to Ångströms. a) shows one of the transmission electron microscopes at the electron microscopy center in Lund (around 4 meters from the floor to the top of the box). Observations of nanowire growth can be made in this microscope. b) shows a 3D reconstruction (electron tomography) of a particle (around 140 nm in diameter) at the nanowire-end. This has separated into multiple regions where the gray contains: gallium and tin, the red: only tin and the yellow (with visible facets) contains: gallium and gold. c) is a nanowire imaged in a TEM (white scale bar is 100 nm) and d) is a higher magnification TEM-image of the crystal structure of a nanowire (white scale bar is 10 nm).

Figur 1 (svenska): Från meter till Ångström. a) visar ett av transmissionselektronmikroskoperna vid elektronmikroskopicentrat i Lund (ca 4 m från golv till toppen av lådan). I detta kan man observera växt av nanotrådar. b) visar en 3D-rekonstruktion (elektrontomografi) av en partikel (ca 140 nm i diameter) på en nanotråds ände. Denna har separerat i flera delar där den grå regionen innehåller: gallium och tenn, den röda: bara tenn och den gula (med synliga platta ytor) innehåller: gallium och guld. c) är en nanotråd avbildad i ett TEM (vita strecket är 100 nm) och d) är en högre förstörd TEM-bild av kristallstrukturen av en nanotråd (vita strecket är 10 nm).

Populärvetenskaplig sammanfattning på svenska

När man tillverkar någonting, vad som helst, vill man ju helst få ett resultat som stämmer väl in med vad man tänkt tillverka. Objektet kanske ska ha en viss mekanisk tålighet, ha en viss färg eller kanske ska leda elektricitet till en viss grad? Elektroniska komponenter, som bara blir mindre och mindre för att få plats fler på samma yta, är väldigt känsliga för variationer i materialet och kräver mycket precis kontroll över tillverkningen. Sammansättningen av material avgör exempelvis hur väl de leder ström och hur effektiva de är i applikationer så som solceller eller lysdioder (LED). Denna avhandling handlar om analysen av små elektroniska komponenter där jag avbildat hur atomerna positionerar sig, deras så kallade kristallstruktur, och vilka koncentrationer av ämnen som finns däri. Jag har både studerat själva förloppet när dessa tillverkas och återskapat 3D-bilder av strukturerna. Detta har lett till insikter i hur snabbt vissa processer sker, lokal koncentration av ämnen, och hur dessa ändras när man ändrar exempelvis temperatur eller inflöde av material. 3D-bilderna har berättat mer om vilka former och ytor som bildas av dessa komponenter. Illustrerande bilder finns i figur 1 på sida x.

När elektroniken blir mindre så spelar enstaka atomer en allt större roll och ännu större krav ställs på tillverkningen. Ett sätt att tillverka mycket små elektriska komponenter är att växa tunna trådar av det önskade materialet. Då dessa kan vara runt några hundra till flera tusen atomer i diameter har de en storlek på nanometerskalan (en nanometer = en miljarddels meter) och kallas *nanotrådar* (se exempel i figur 1c). Dock är själva växtprocessen komplicerad och små förändringar i hur man gör kan leda till helt annorlunda nanotrådar, både i struktur och sammansättning. Detta motiverar studier av hur vi kan göra justeringar för att få nanotrådar med just de egenskaper vi söker och, i mitt fall, hur vi studerar dessa ner på atomnivå.

Då vanliga ljusmikroskop är begränsade i upplösning använder vi oss av elektroner som kan fås med mycket kortare våglängd (den annars begränsande faktorn). Mer specifikt har jag använt så kallad transmissionselektronmikroskopi (TEM) (figur 1a). I ett TEM sänder vi elektroner genom provet och mäter på andra sidan hur de passerat provet. Bilden som skapas har mycket hög upplösning och vi kan se atomerna i provet (figur 1c-d). Moderna TEM har en punkt-till-punkt-upplösning bättre än en Ångström (en tiondels nanometer) vilket givetvis är användbart. Jag har använt två speciella varianter av TEM för att studera nanotrådarna: att utföra växten av trådarna i mikroskopet och *filma* detta *in-situ* (när och där det sker) med hög upplösning och analysera kemiska sammansättningen samtidigt, samt att återskapa tråden i alla tre dimensioner (*elektrontomografi*, figur 1b).

Studierna i denna avhandling är viktiga för att få mer kunskap om nanotrådarna och hur man växer dem på bästa sätt för att ytterligare kunna finjustera deras egenskaper. Användandet och utvecklandet av TEM-teknikerna belyser hur de kan bidra med information, deras fördelar och nackdelar, inte bara för användning på nanotrådar utan också för andra material.

List of acronyms and abbreviations

Presented in alphabetical order

ADF	annular dark-field	MEMS	microelectromechanical systems
AsH ₃	arsine	MO	metal-organics
BF	bright-field	MOCVD	metal-organic CVD
BFP	back focal plane	MOVPE	metal-organic vapor-phase epitaxy
BP	backprojection	NMF	non-negative matrix factorization
cb	conduction band	OL	objective lens
CL	condenser lens(es)	PCA	principal component analysis
COM	center-of-mass	PH ₃	phosphine
CSET	compressed sensing ET	PL	projection lens(es) (also photoluminescence)
CT	computed tomography	\mathcal{RT}	radon transform
CTEM	conventional TEM	SEM	scanning EM
(p)CTF	(phase) contrast transfer function	SI	spectrum image
CVD	chemical vapor deposition	SIRT	simultaneous iterative reconstruction technique
DART	discrete algebraic reconstruction technique	STEM	scanning TEM
DF	dark-field	TEM	transmission EM
DMA	differential mobility analyzer	TMGa	trimethylgallium
EELS	electron energy loss spectroscopy	TMI _n	trimethylindium
E_g	bandgap energy	TV	total variation
EM	electron microscope	vb	valence band
ET	electron tomography	VLM	visual light microscopy
ETEM	environmental TEM	VLS	vapor-liquid-solid
FBP	filtered backprojection	WPOA	weak phase object approximation
FEG	field emission gun	WZ	wurtzite
FIB	focused ion beam	XEDS	x-ray energy dispersive spectroscopy
FL	filter lens(es)	XPS	x-ray photoelectron spectroscopy
\mathcal{FT}	Fourier transform	ZB	zincblende
HAADF	high angle ADF		
HRTEM	high resolution TEM		
IC	integrated circuit		
IL	intermediate lens(es)		
LaB ₆	lanthanum hexaboride		
LED	light emitting diode		

Chapter 1

Introduction

The quest for materials of the future is engaging many scientists from different disciplines all around the world. From theory, interesting new combinations of elements or structures can be developed, but they also need realization in order to be tested and considered interesting. In materials science a constant feedback-loop of theory, synthesis and analysis exists, which not only produces the materials but also develops theory concepts, calculations, manufacturing methods and instrumentation for analysis. In this thesis, the analysis has been in focus and especially for the analysis of semiconducting III–V nanowires using high-resolution *transmission electron microscopy* (TEM).

As an analytical tool, an electron microscope has many advantages compared to a regular visual light microscope, but the major one must be its spatial resolution. TEMs can resolve the lattice of crystalline materials down to the atomic scale, making it possible to distinguish atomic spacing, their arrangement or possible discrepancies in the arrangement. Knowing the exact atomic information of a material might in many cases be excessive, but for modern day nanotechnology it is exactly what is often needed as it dictates important properties of the material. Also, given the size of the nano-objects it is easy to understand that individual atoms play an increasingly important role in how the full object behaves when the size of the components become smaller and smaller. Since the invention of the electron microscope in the 1930's [1][2, p. 4], many advances of the design have been made, and this trend is expected to continue. With quicker and more efficient detectors, measurements are expected to be made at a higher rate and with lower intensity of the incoming electron beam, making it possible to measure material properties that only last for a short while (e.g. time-resolved *in-situ* measurements) or measure properties that are sensitive to the electron beam [3–7]. Further, the concept of correlative microscopy adds com-

plementary measurements to the already highly informative electron microscopy, i.e. combining advantages of multiple techniques in order to get comprehensive information. Advanced data processing also further increases the amount of information retrieved from the acquisitions [8, 9].

1.1 Research hypothesis and the layout of the thesis

Scaling down the size of a material will have the effect that each atomic feature contributes a larger portion to the total volume. This is an interesting effect of nanoscience in general and poses strict demands on the accuracy of the manufacturing of nanocomponents, as well as the analysis thereof. The main topic of this thesis and the work performed is on the analysis of III–V semiconducting nanowires through transmission electron microscopy and developed related techniques; time resolved *in-situ* studies and electron tomography. The hypothesis is:

I believe that adding dimensions to transmission electron microscopy (TEM), such as time (in-situ) and the third spatial dimension (tomography), will improve our understanding of nanowires, how they grow and form, as compared to the more conventional high resolution, single projection and non-time resolved TEM.

The concept of nanowires will be introduced in chapter 2, in which the special properties of the semiconductors in nanowire form will be discussed and illustrated. Also, the methods used for growing the wires will be shown, as well as how the nanowires actually look in electron microscopy (both scanning EM and TEM). After that, the following chapters will deal with the different parts of the TEM-analysis performed and refer back to the information presented in chapter 2 on what properties can be analyzed using that technique. Chapter 3 will present the transmission electron microscope, how electron micrographs (images) are formed in the instrument as well as what the different detectors can tell us about local structures and compositions. Then, sections 3.7, 3.8, chapters 4 and 5 will present the specific kind of TEM-analysis performed through this thesis and relate that to the included papers, as well as the theory on the nanowires. An introduction to the techniques, both in a practical sense and in theory, will be presented in order to discuss advantages and disadvantages. The analysis methods include high resolution TEM, compositional analysis (using *x-ray energy dispersive spectroscopy*, XEDS), real-time observations of growth events (*in-situ* TEM) and 3D-reconstructions of nanowires (*electron tomography*, ET).

1.2 An introduction to semiconductors

The politics of energy generation and consumption is difficult and a delicate area, and it is one of the major questions for humankind to answer. However, from a scientific point of view, especially materials science, there are hopeful solutions on how to cater to our energy needs by the introduction of novel materials. Devices made from these can for instance be tuned to require less energy to operate, or they can convert non-useful energy to useful, e.g. photon energy from the sun to electricity. At the forefront of this battle are semiconductors. This family of materials have applications in many fields. Most interesting for the topic of energy efficiency (in both production and consumption) are photovoltaic devices such as *solar cells* and *light emitting diodes* (LEDs). The efficiency of electrical components (*integrated circuits*, IC) can be increased by the correct choice of semiconductor [10–12]. Here, the concept of semiconductor research is introduced, and then further explained in section 2.1.

The semiconductors are, as the name suggests, electrically conducting but not as conducting as metals. This property is what makes them so interesting. As part of a device the semiconductor can be altered to, for instance, only conduct in a certain direction or under certain conditions. This in turn can be used to create charge imbalance (electrical energy) from solar photons or control over the exact energy of photon emission (in LEDs) [13]. In the case of IC components, the semiconductors have vital properties, such as their use in transistors, where the throughput currents can be controlled using only small applied voltages [12, 14].

The most prominent semiconductor by far is silicon (Si, highlighted blue in figure 1.1), which, due to its high abundance and excellent properties, is the most used element in the electronic industry today [15, p. 2]. It is a well-established standard and one of the more abundant elements, especially for electronic applications, which makes it unlikely to be replaced anytime soon. Other elements have been shown to surpass Si in certain properties, however, not to that extent that Si becomes obsolete. Instead, integration of specialized components (consisting of other elements) onto conventional Si-based circuits could be a promising way of increasing efficiency in for example solar cells and high frequency electronics [16, 17].

Examples of uses of such other elements are the so-called *III–V semiconductors*, which are commonly occurring in this thesis. These are compound semiconductors in which a 1:1 ratio of two different groups of elements (group III and V, commonly also referred to as group 13 and 15, see figure 1.1) combine to form a semiconductor. The III and V relate to the number of valence electrons in the element. Even though the ratio between the groups is 1:1, multiple combinations of more than two elements (ternary and quaternary compounds, 3 and 4 respectively) can be used to fine-tune

1 Introduction

Group →	1	2	3	4	5	6	7	8	9	10	11	12	13	14	15	16	17	18							
↓ Period																									
1	1 H																	2 He							
2	3 Li	4 Be											5 B	6 C	7 N	8 O	9 F	10 Ne							
3	11 Na	12 Mg											13 Al	14 Si	15 P	16 S	17 Cl	18 Ar							
4	19 K	20 Ca	21 Sc	22 Ti	23 V	24 Cr	25 Mn	26 Fe	27 Co	28 Ni	29 Cu	30 Zn	31 Ga	32 Ge	33 As	34 Se	35 Br	36 Kr							
5	37 Rb	38 Sr	39 Y	40 Zr	41 Nb	42 Mo	43 Tc	44 Ru	45 Rh	46 Pd	47 Ag	48 Cd	49 In	50 Sn	51 Sb	52 Te	53 I	54 Xe							
6	55 Cs	56 Ba		72 Hf	73 Ta	74 W	75 Re	76 Os	77 Ir	78 Pt	79 Au	80 Hg	81 Tl	82 Pb	83 Bi	84 Po	85 At	86 Rn							
7	87 Fr	88 Ra		104 Rf	105 Db	106 Sg	107 Bh	108 Hs	109 Mt	110 Ds	111 Rg	112 Cn	113 Nh	114 Fl	115 Mc	116 Lv	117 Ts	118 Og							
				Lanthanides							57 La	58 Ce	59 Pr	60 Nd	61 Pm	62 Sm	63 Eu	64 Gd	65 Tb	66 Dy	67 Ho	68 Er	69 Tm	70 Yb	71 Lu
				Actinides							89 Ac	90 Th	91 Pa	92 U	93 Np	94 Pu	95 Am	96 Cm	97 Bk	98 Cf	99 Es	100 Fm	101 Md	102 No	103 Lr

Figure 1.1: The periodic table of the elements with elements of interest highlighted. Red highlights group III elements, green highlights group V elements, and blue highlights silicon. Figure derived from Wikimedia Commons (Public domain): https://commons.wikimedia.org/wiki/File:White_periodic_table.svg

the properties [13, 16]. For the III–V semiconductors the used elements include, from the Triels (group III); boron, aluminum, gallium and indium, and from the Pnictogens (group V); nitrogen, phosphorus, arsenic and antimony. This means that possible III–V semiconductors include $GaAs$, $Ga_xIn_{1-x}Sb$, $InAs_yP_{1-y}$ and even more complex: $Ga_xIn_{1-x}As_ySb_{1-y}$.

The research into semiconductors and how to improve these III–V compound semiconductors include what combinations are best used for each application, how different compositions can be combined and how these should be manufactured with as few imperfections as possible. In this thesis, these questions are studied from an analysis standpoint and how these III–V semiconductors, in the form of nanowires, can be understood better with the help of TEM.

1.3 Electron microscopes and what they are good for

Visual light microscopes (VLM, figure 1.2) have proven beneficial for many branches of sciences since they help visualizing the finer details of any object. With improved manufacturing of optical lenses, the resolution has improved even further, making it possible for scientists to understand the world around, from biology to materials. However, visual light inherently has a limit of resolution set by its wavelength [2, p. 5] and is thereby not able to image finer details, such as atomic arrangement. Electron

1.3 Electron microscopes and what they are good for

microscopy (EM) breaks this limit by, instead of using visual light, using electrons that are accelerated towards the sample. These electrons have, through the particle-wave duality, a considerably shorter wavelength than visual light and hence give better theoretical resolution [2, pp. 5-6]. Therefore, EM provides more information about the micro/nanoscale, useful for material science as well as biological applications [18, 19].

Two common types of EM are *scanning EM* (SEM) and *transmission EM* (TEM) (both seen in figure 1.2). Their differences lie in how the imaging occurs. The SEM forms a fine focused probe of electrons, intended to only illuminate a very small spot at a time, and collects data from that spot before moving on to the next in a rastered pattern [20, pp. 103-108]. Using detectors situated on the top side of the sample (the same side as the electrons enter from), the electrons emitted or backscattered from the sample can be detected. The amount of electrons (counted in the detectors) determines the intensity of that point/pixel in the formed image [20, pp. 75-96].

In the TEM only very small (thin) samples are possible to analyze, since the method requires electrons to be able to pass through, only interacting to a small extent, and then form an image at the detector on the other side [2, pp. 5-6]. Such thin samples (thickness requirement depends on the acceleration voltage of the electrons) can be created by either polishing or cutting the sample before TEM-analysis (section 3.6) [21, 22].

Similar to VLM, the electrons must be able to be deflected by lenses in order to form images. While the lenses in VLM consists of glass or polymers, the EM-lenses are electromagnetic. The circular magnetic field will focus the electrons with desired focal lengths using fine tuning of the current in the electromagnetic coil and can hence be treated similarly to how photons would pass through an optical setup with positive lenses [2, pp. 91-101]. However, the setup of lenses in an EM are not without its flaws (aberrations) and these will be discussed in section 3.3 and 3.4 where also the concept of aberration correction will be presented. This will show why the TEM has high, but not infinitely high, resolution. In addition, the incoming electrons from the microscope will interact with the atoms present in the sample, either their electrons or the nuclei, interactions which are possible to detect. This gives EM further possibilities in the form of composition measurements, either by studying the energy lost by the electrons or fluorescent x-ray energies (further details in section 3.7).

All in all, the TEM and EMs in general are great tools for materials science (and other analysis) due to their high resolving power, possibility to image atomic scale features and answering questions such as: What atomic differences between these devices are causing their different properties?

1 Introduction



Figure 1.2: Three different microscopes that all have been used during the thesis. From left to right: A visual light microscope (VLM, Leica), a scanning electron microscope (SEM, Jeol JSM-6700F), a transmission electron microscope (TEM, JEM-3000F).

Chapter 2

III–V semiconducting nanowires and their growth

As mentioned in section 1.2, semiconductors have important uses in electronic applications, including energy harvesting, and it is key to be able to adjust their properties with as great accuracy as possible in order to realize complex components. This chapter will briefly present the principle of semiconductors (section 2.1), their crystal structure (section 2.2), how they are fine-tuned for specific purposes in the form of nanowires (in section 2.3), and finally how the nanowires throughout this thesis are produced (grown) (section 2.4). This description will help in understanding the TEM-analysis in the following chapters.

2.1 Semiconductors

In order to understand the special properties of semiconductors we must first look at the concept of energy bands, a feature which defines them [23, pp. 104-112]. When atomic orbitals overlap, they form electron energy states which are both higher and lower than the initial single atomic states, which hence promote bonding [23, pp. 77, 83–87]. Figure 2.1a shows a schematic over how two atomic s-orbitals form what is known as σ and σ^* states (bonding and antibonding respectively) when combined [23, pp. 77, 83–87]. However, multiple periodically ordered atoms (as in a crystal) will create multiple, tightly spaced, combined states for the electrons to reside at, illustrated in figure 2.1b (including both p- and s-orbitals) [24, pp. 185-195]. The more atoms that are included into the model, the more combined states are created, which will have closer and closer energy levels. At realistic crystal sizes the spacing

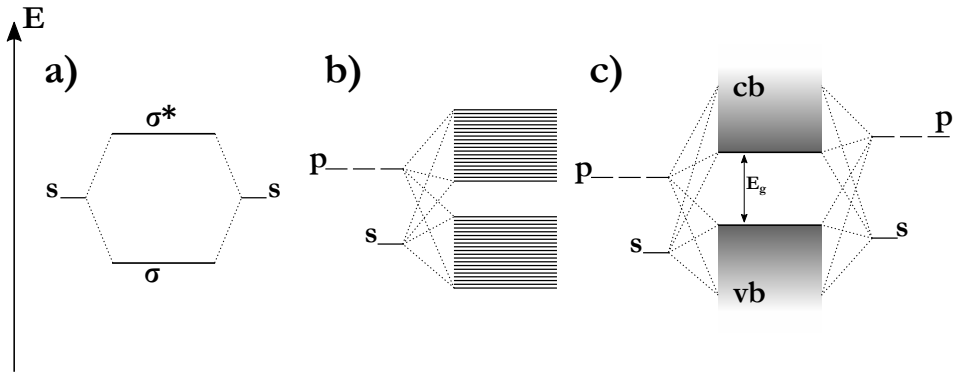


Figure 2.1: Three cases of combinations of energy states from multiple atoms. a) shows two atoms with s-levels (such as the simple case of H) which combines to form a lower and a higher energy state, σ and σ^* respectively. b) shows the case of multiple combinations of atoms of the same type and how their combinations form tightly spaced energy levels (bands) with occasional lack of states (bandgaps). c) illustrates the same case as b) but with two different elements, which will alter the position and width of the bandgap E_g . The bands are here shown as continuous energy states. N.B.: The energy axis should not be considered common for all three cases.

between these combination states are negligibly small and are considered to be continuous bands (in figure 2.1c shown as two bands, *conduction band*, cb, and *valence band*, vb) [23, p. 106].

Due to the energy levels of the original states of the individual atoms, there will be disruptions in the continuous bands of electron states from their combinations. These are referred to as *bandgaps* and they play a crucial role into the properties of semiconductors. When the electrons of the atoms, making up the crystal, fit in the energy bands they fill up to a certain level depending on the atomic number (i.e. number of electrons) or if there are multiple elements present (different number of electrons). The level to which the electrons fill, in combination with the band gap size, is crucial and will determine if the material is conducting, semiconducting or insulating [23, pp. 110-111]. For a material to conduct electrons they must be able to move (*mobile charges*), creating an electric current. In their ground state (achieved at 0 K, at which the highest filling level is referred to as the *Fermi level*) the electrons cannot move due to the energy levels of the neighbor already being filled with the corresponding energy electron. The solution to this is for the electron to gain some energy and hence being able to access the neighboring atoms' energy states at the new slightly elevated energy.

This holds true for conductors, such as metals, but the case for insulators, and more interestingly semiconductors, is that the Fermi level coincides with a band gap and there are no *empty* energy states just above. The bandgap has become a barrier for conduction. The difference between insulators and semiconductors however is that insulators' bandgaps are large and there is very little chance of electrons being excited across. Semiconductors' bandgaps are on the order of a couple of eV which can be

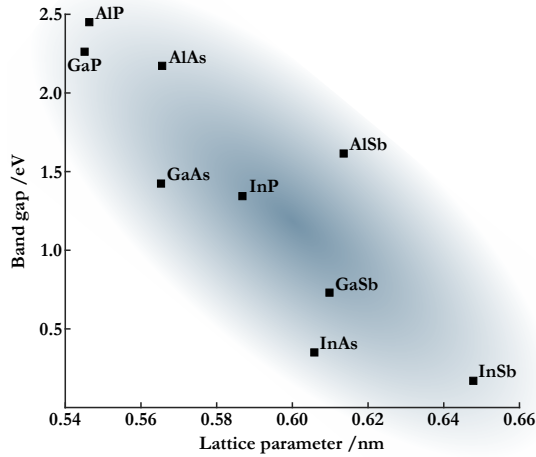


Figure 2.2: A map over some of the binary III–V compounds showing how their lattice parameters and bandgaps differ [16]. To produce III–V semiconductors with properties in between the binaries, ternary or quaternary compounds must be used. As a reference, visible light has energies between 1.65 and 3.10 eV. Figure adapted from [25].

overcome by heat or photon energy. The amount of electrons promoted to the *conduction band* determines the conductivity of the material, hence it is possible to adjust the conductivity of a semiconductor if one can control the amount of charge carriers able to conduct [23, p. 111].

When *compound semiconductors* form a crystal, just as in figure 2.1b, the energy levels of the individual atoms are different. Combining different levels will of course affect the bands' positions and the size of the bandgap [24, p. 195], illustrated in figure 2.1c. As mentioned in section 1.2, one can also combine more than two elements, as long as the ratio III:V stays 1:1. This means that it is possible to, using the highlighted elements in figure 1.1, design the exact band levels through careful compositional control.

Also important to account for is the size of the lattice itself since these III–V semiconductors are often grown using heteroepitaxy (more in section 2.4) and the otherwise perfectly repeating crystal needs to adjust its size to merge with a second lattice with another size [15, pp. 152-153]. Figure 2.2 illustrates how some of the binary III–Vs relate to each other in terms of bandgap and lattice size. Small differences in lattice size can be accounted for by straining the lattice (see figure 2.3a), resulting in slightly deformed structure (which in turn affects band structures) [12], but too large ones will cause *dislocations*, disruptions in the crystal lattice, and reduce the quality of the crystal (see figure 2.3b and c). Finally, there are other properties of the III–V semiconductors that are of interest, which motivate their use. The mobility of the electrons

2 III–V semiconducting nanowires and their growth

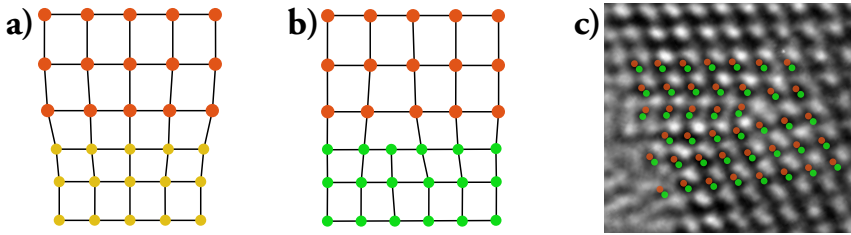


Figure 2.3: Illustration of different lattice sizes combining through straining the lattices a) and formation of a dislocation b). c) shows a HRTEM micrograph of a dislocation (nanowire structure from unpublished work), with overlaid atoms to highlight the dislocation.

in these materials, especially in InAs, have been shown to greatly surpass that of Si, meaning that currents can be switched at much higher speeds which can be useful in high-frequency electronics [17].

To be able to control the currents in a semiconductor, impurities, in the form of elements with more or fewer electrons, can be added. Such elements will disrupt the *perfect* amount of electrons that fill the valence band completely. Doping levels can be on the scale of 10^{16} to 10^{19} cm^{-3} (compared to $4.995 \cdot 10^{22}$ atoms/cm^3 for Si [26]) and are thereby very small. They do not affect the lattice to a large extent but will have great effect on the electrical properties[citation]. If an element with *too few* electrons are added, there will be vacancies in the valence band, *holes*. The semiconductor is said to be *p-doped* and with the holes as *charge carriers* it will be able to conduct electricity to an extent depending on their concentration [24, pp. 192-193]. The same principle applies for dopants that supply more electrons than what a constituent atom in the semiconductor does (*n-doping*). These electrons instead start to fill the conduction band and the electrons in that band act as charge carriers [24, pp. 192-193].

For Si, p-doping is achieved through addition of the group III elements, and n-doping from the group V elements [24, p. 192]. For the III–V semiconductors on the other hand the doping type will depend on which of the constituents it replaces. For example, GaAs can be p-doped by substituting Ga with Zn and n-doping by substituting As with S [27, 28]. However, Si and Ge can create either p- or n-doping depending on if they substitute As or Ga respectively [29]. In paper VII the n-doping concentration of a GaAs nanowire is controlled through introduction of Sn at different concentrations during growth.

2.2 Crystal structure of III–V semiconductors

All III–V compounds apart from the nitrides (III–N) adopt the cubic sphalerite structure, also known as *zincblende* (ZB), in bulk. This structure is closely related to the

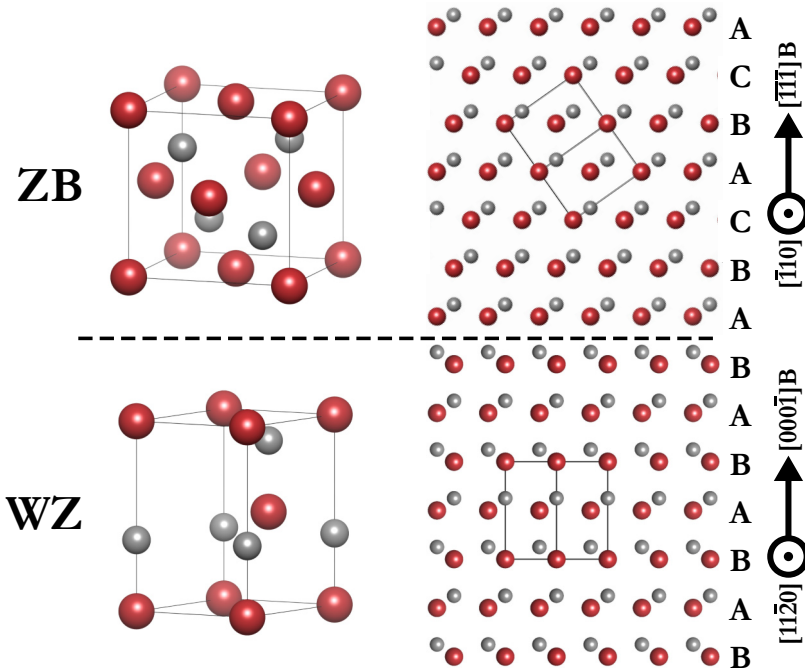


Figure 2.4: Models of the zincblende (ZB) and wurtzite (WZ) crystal structures. Each are shown in their unit cell form (left), cubic and hexagonal respectively, as well as in projection in one of the preferred viewing directions in the TEM: $[1\bar{1}0]$ and $[11\bar{2}0]$ respectively. The letters A-C indicates the different types of bilayers (their position).

diamond structure, which Si adopts [30, p. 79], so it is easy to see the similarities between these two different types of semiconductors. The ZB structure is the thermodynamically stable structure, however other versions are also possible. The other common structure is called *wurtzite* (WZ) and it has a hexagonal structure which is the thermodynamically stable structure for the nitrides but as mentioned also possible for the rest of the III–Vs under certain conditions [31, 32].

The zincblende structure is based on the cubic close packed (CCP) structure, a structure with an atom in each corner as well as on each face of the cube (red atoms in figure 2.4). For ZB the motif of each lattice point can be explained as an atom (of the first type, let us say group III) at: $0, 0, 0$ and a group V atom shifted $\frac{1}{4}, \frac{1}{4}, \frac{1}{4}$ (gray atoms in figure 2.4). The result is two CCP structures, one of each type of atom, interwoven with an atomic ratio of 1:1. Wurtzite, on the other hand, is based on the second close packed structure, hexagonal close packed (HCP). In this case the group V atom is shifted $0, 0, 0, \frac{3}{8}$ relative to the group III one (again, red and gray atoms respectively in figure 2.4), which also means the atomic ratio is 1:1. If the structures are observed as in figure 2.4, in the $[1\bar{1}0]$ or $[11\bar{2}0]$ direction for ZB and WZ respectively, one can consider the layers of each atom-type (III or V) to have different stacking order depending on the structure. ZB stacks with an order of ...ABCABC...

while WZ stacks as ...ABABAB... where the different letters correspond to where the atomic pairs (III–V) stacked on top of each other (letters in figure 2.4 mark the layers of the red atoms). ZB repeats every third layer and WZ every second [33].

Important to remember for the compound semiconductors is that the polar character of the bonds between the two constituents will create differences in polarity between surfaces [34, 35]. Some surfaces, such as the {111}, are either terminated by a layer of group III or group V atoms (bottom or top layer, red or gray atoms, in figure 2.4). For this thesis and most of the literature the surface terminated with V-atoms is considered the {111}B [36]. Other surfaces, such as the {110} or {211} (the sides of the projected ZB-structure in figure 2.4) does not have the same polar properties due to the surface consisting of equal amount of group III and V atoms. Polarity is of consideration in paper I, where the accumulation of droplets on a nanowire surface greatly depends on the polarity of the surface. Also, the polarity can play a role in the preferred facets explored in paper II.

2.3 Nanowires

At the nanoscale, individual atoms or small atomic features make out a larger part of the total volume. The so-called *surface-to-volume ratio* is very high compared to bulk materials. In the case of nanoparticles, a larger portion of the atoms are not present in the nicely ordered crystal but rather as more loosely bound, rearranged, surface atoms, with differing properties compared to bulk [16]. Also, when a dimension of the material decreases, this restricts the possible energy states of the electrons and what is called quantum confinement occurs [16, 37]. Nanowires are elongated narrow structures with a diameter in the range of a couple of nm to about 200 nm [38] (electron microscopy images are shown in figure 2.5). In this arrangement, it is possible to make use of both the high surface-to-volume ratio, quantum confinement in the radial dimension, as well as the possibility to grow *heterostructures* both axially and radially not possible in bulk.

Heterostructures are combinations of multiple different structures such as different compositions or crystal structures, for instance controlled switching between ZB and WZ crystal structures. As seen in figure 2.2 the different III–V combinations vary in lattice parameter. This results in *lattice mismatch* if two of these are to be grown onto each other, which was illustrated in figure 2.3. The amount of lattice mismatch depends on the combination of materials making up the heterostructure [39]. Nanowires have been shown to be able to accommodate larger lattice mismatch due to their small dimensions, which can expand radially to a larger extent than in bulk.

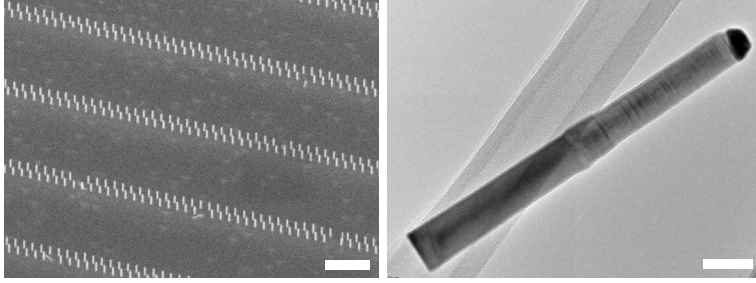


Figure 2.5: Electron microscopy images of nanowires. SEM (left) of an array of grown wires (InAs-GaSb studied in [12]) at 30° observation angle and TEM (right) of a single wire (InAs-InGaAs studied in [14]). The uneven structure in the center of the wire in the TEM-image is a change in crystal structure due to a change in composition. Scalebars are $1\ \mu\text{m}$ and $50\ \text{nm}$ respectively.

This makes nanowires a useful platform for realizing heterostructures not possible to achieve dislocation-free in bulk [40–42].

The possibility of mixing and matching materials in the form of nanowires also improves the compatibility of the III–V semiconductors with existing Si technologies [14]. Since Si has a lattice parameter of $5.431\ \text{\AA}$ [26] there are varying degrees to lattice mismatch to the III–Vs (compare to the values from figure 2.2). Therefore, careful consideration of materials and dimensions must be taken in order to create heterostructures without dislocations.

Another selling point for nanowires, apart from the possibility to combine different lattice parameters, is the possibility of crystal structure control through switching between the ZB and WZ, and other similar structures [32, 43, 44]. In section 2.2 the differences between ZB and WZ were described. Out of these, ZB is the thermodynamically more stable form in bulk for the III–Vs (disregarding the nitrides, III–N). However, due to the prevalent effect of surfaces in the confined volume that is the nanowire, how the crystal forms also must be considered. Under certain conditions, this will promote the growth of WZ over ZB due to extra energies involved in the formation of a layer, which has been shown both theoretically and in experiments. Thereby, polytypism can be controlled by the actual conditions during growth, even though the structure itself is quasi-stable [31, 44].

2.4 Nanowire growth methods

How does one realize controlled nanowire growth? Since the structures are pillar-shaped, the material should be added onto confined areas and then, continuously being added onto that small area, forming a narrow structure layer by layer. Some fundamental things to control in order to achieve nanowire growth are:

2 III–V semiconducting nanowires and their growth

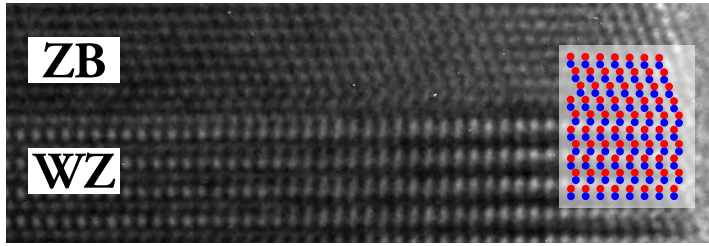


Figure 2.6: HRTEM image of switching between the two crystal structures Wurtzite (WZ) and Zincblende (ZB) with highlighted interface using red and blue circles for the atoms (compare to figure 2.4).

- The location for the nucleation of the nanowire
- The size of those areas (size of wire cross-section)
- The composition and the crystal structure of the wires
- To add the material preferentially onto the top of the wire instead of its sides or the substrate in between the wires [45]
- The time of growth (which determines the wires' lengths)

Epitaxial growth refers to the formation of layers on an already existing crystal, at which the crystal acts as a guide for how the new layer is formed. This concept is important for forming high-quality crystalline materials with known properties. If the same concept is applied to a larger surface, it is possible to add individual layers that retain the single-crystalline nature of the sample and the crystallographic type. The thickness is controlled through the time the process is run. If the material added matches the template material the same kind of crystal is continued and is referred to as *homoepitaxy*. The opposite is called *heteroepitaxy*, which makes the crystal more complex and the differences in sizes between the different layers can cause a mismatch.

Since control over where the epitaxial growth occurs is key for forming nanowires, the planar growth must be suppressed, or the energy of forming growth at specific sites must be reduced. A common method, and the one used for all the nanowires in this thesis, is called *vapor–liquid–solid* (VLS) [46]. This principle is characterized by a droplet of a catalyst metal on top of the substrate. The growth material is added as a vapor-precursor, being cracked to its atomic component and alloying with the liquid catalyst, and finally nucleating epitaxial growth at the liquid–solid interface (going the path of vapor to dissolved to solid) [47]. Seen in equation 2.1 is the net-formula for production of solid InAs from TMIIn and AsH₃ using the VLS method. Using VLS, epitaxial growth is performed at very well-defined areas, at the interface between the liquid droplet and the crystalline substrate, and thereby many of the requirements in the list starting at page 14 are fulfilled: Controlling the amount, positions and sizes of

the particles will determine the number density, positions and diameters of the wires. In addition, the composition and crystal structure of the wire will be determined by the added growth material, in combination with parameters such as temperature and pressure. To be able to fulfill the other requirements, growth conditions are chosen so the liquid stays on the wire top during growth and the time of growth will determine its length.

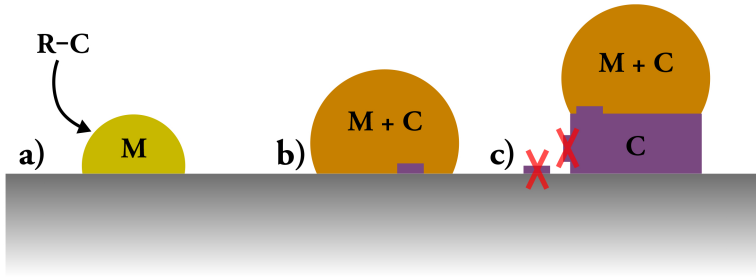
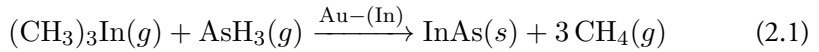


Figure 2.7: Sketch showing the effect of the seed particle on the nucleation event. a) shows the seed particle containing a metal (M) and how a metal-organic precursor of the component C is added (R-C). In b) the metal and component C has formed a liquid alloy and a nucleation event occurs where the component C forms an epitaxial layer on the substrate. c) shows the growing wire of C, also showing where nucleation sites to suppress in order to grow a straight wire.

For VLS to be the method of growth it must be energetically favorable to form a new *bilayer* (both group III and V added) at the liquid–substrate interface, rather than on the non-covered surface. To form a bilayer, *nucleation* must occur, where a collection of adatoms starts to form epitaxial growth on the surface. However, this step is energetically unfavorable since this creates new surfaces with associated surface energies [47] (figure 2.7). The advantage of forming the nucleus is however to reduce the amount of growth-atoms in the liquid droplet. When the precursors impinge at the particle and crack to release its growth component to dissolve into the droplet, the excess, or *supersaturation*, will be energetically unfavorable to remain in the droplet [47]. Using the flow rate of the precursors and adjusting the temperature accordingly, it is thereby possible to control the growth rate and find a balance between uptake and nucleation in the seed particle. This has been shown to play a part in controlling the diameter and crystal structure of the nanowire [31, 44, 48]. This concept is of course made more complex when a second component is added (as in III–V materials). Then the combined energy will play a role in determining if a nucleation occurs since their solubilities might differ substantially [49]. The growth can also be limited by either of the constituents, which is discussed in paper v, and to actually form a new layer

2 III–V semiconducting nanowires and their growth

can be limited by both the energy overcoming the barrier of nucleation as well as for all the atoms to arrive at the growth site quickly enough (kinetic limitations).

The *metal-organic chemical vapor deposition* (MOCVD, sometimes also referred to as *metal-organic vapor-phase epitaxy*, MOVPE) system is a set of sources, controls for gas-flows and a reaction chamber with heating that enables precise control over the epitaxial growth. In this thesis only the wires from paper II are grown in what should be considered a conventional MOCVD-reactor. The wires in papers I, VI and VII are grown using Aerotaxy while the rest are grown in a MOCVD-like system integrated with a TEM. However, they all share some major properties.

The supplies of precursors for growth are handled through a mixing setup which can control the amount of each precursor to add, as well as possible dilution from hydrogen (H_2). Examples of different precursors are listed in table 2.1, which also highlights that extra care should be taken when handling these chemicals. Some of these precursors are gaseous and can be supplied as is, however, some (especially the metal-organics, MOs, e.g. TMGa) are liquids/solids and require a carrier gas, H_2 , that bubbles through them and carries the evaporated precursor to the reaction chamber. The environment created at the reactor chamber, in combination with the possibility to heat the sample, will initiate the reactions and hence controlled growth of nanowires can be achieved.

Table 2.1: List of example precursors for the different elements, including the precursor for Si. All the Global Hazard System (GHS) hazard pictograms for the respective chemicals are also shown.

Element	Group	Precursor	Dangers/pictograms
Aluminum	III	Trimethylaluminum (TMAI)	
Gallium	III	Trimethylgallium (TMGa)	
Indium	III	Trimethylindium (TMIn)	
Silicon	IV	Silane (SiH_4)	
Phosphorus	V	Phosphine (PH_3)	
Arsenic	V	Arsine (AsH_3)	
Antimony	V	Trimethylantimony (TMSb)	

Still to be presented is the growth method for the nanowires of papers I, VI and VII. It is a variant of the conventional MOCVD system where the substrate is removed. Nucleation of nanowire growth is occurring from free flowing catalyst particles, so far only Au [27, 50–53]. The method is shown in figure 2.8, in which first Au is evaporated to form Au agglomerates which are size-selected using a *differential mobility analyzer*

(DMA) and formed into single particles by flowing these through a heating furnace. Growth itself is carried out by a continuous flow of the particles through additional furnace(s) where the precursors are added into the stream, creating growth conditions similar to a conventional MOCVD but without the crystalline substrate [50].

The main advantages of Aerotaxy compared to conventional MOCVD includes that it is a continuous process. The wires are collected on a suitable substrate, placed in the stream. The substrates can easily be replaced during a run. In addition, since the substrate onto which the nanowires are collected has nothing to do with the growth, as opposed to the epitaxial template in conventional nanowire growth, there is no need for using single crystalline substrates. These can, especially for the III–Vs, be very expensive [52]. The growth rate of a wire is also very high compared to conventional MOCVD and does not diminish at higher temperatures [50].

The method has so far been able to produce high-quality nanowires [50], including n-doping [51] and p-doping [27], as well as p-n-junctions [52], which are all promising for realizing alternatives to the batch-based process of MOCVD nanowire growth, without expensive single-crystalline substrates.

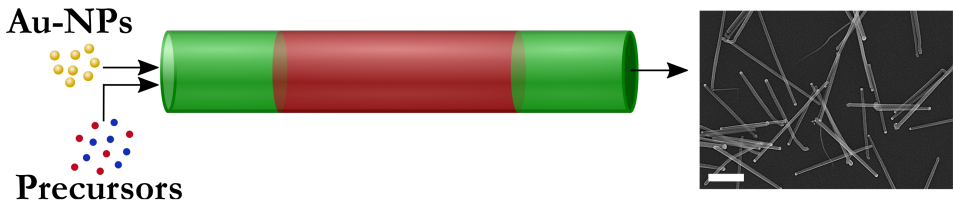


Figure 2.8: Schematic illustration of Aerotaxy. The seed particles, in this case Au, are inserted in the furnace with the precursors and VLS-growth is initiated and proceeding very quickly. Lastly, the wires are collected onto a substrate (SEM-image, scalebar is 1 μm). SEM-Image courtesy: Wondwosen Metaferia. Figure adapted from [25].

Chapter 3

Transmission electron microscopy

The transmission electron microscope (TEM) is the instrument used in this thesis to analyze the structures presented in chapter 2. While the instrument is quite complex, the main principle is rather easy: to send electrons into a sample and analyze what is coming out. In the case of transmission EM, this especially means analyzing the transmitted electrons and how these are affected by the sample. However, there is more to the TEM than this and in this chapter the principles of the microscope (section 3.1), different modes of imaging and ways to achieve high resolution (sections 3.2 to 3.5) are presented. This is followed by a section on sample preparation to produce thin enough samples for the TEM (section 3.6). The chapter ends with compositional analysis and *in-situ* measurements (sections 3.7 and 3.8 respectively).

3.1 The microscope

A TEM setup consists of a source of electrons, a series of electromagnetic lenses for focusing the electrons and creating images, some apertures to restrict some electrons from participating in the analysis, and detectors that either interpret the electrons passing through the sample or other emitted signals, such as emitted x-rays (section 3.7). Using the different signals, information about the sample in the form of crystallography, composition and shape can be obtained. Figure 3.1 shows one of the TEMs used for the results in the thesis next to a schematic drawing.

The path of an electron starts at the electron-gun, the emitter which in most modern TEMs is a narrow tip made from W, possibly with some coating of zirconia [54, p. 88]. The electrons are extracted using a high electric field (*field-emission gun*, FEG) which produces electrons with narrow energy-spread and small spatial origin [2, p. 74, 81].

3 Transmission electron microscopy

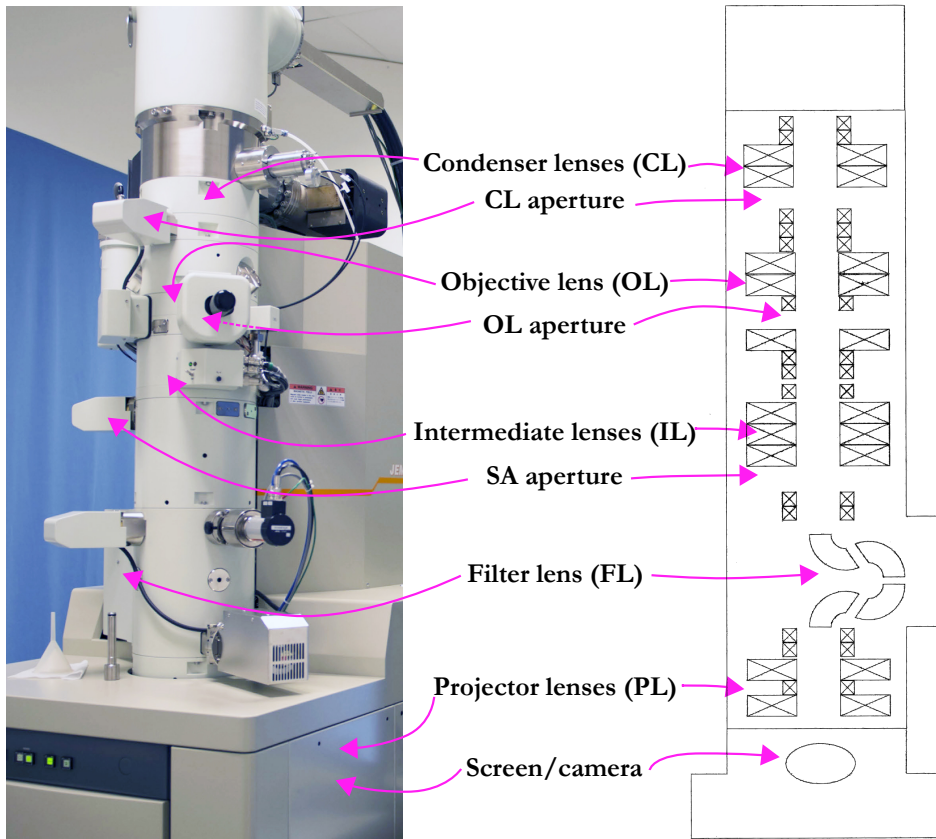


Figure 3.1: A photo and schematic drawing of a Jeol 2200FS TEM. Arrows are indicating the positions of the different lenses and apertures. The drawing to the right is adapted from the manual of the microscope.

Variants of the (cold-)FEG include the heat-assisted FEG (Schottky-FEG), which reduces the contamination on the tip, but gives a broader energy-spread of the emitted electrons [2, p. 81]. Other types of guns, used in older microscopes or ones with less resolution requirements, include thermionic guns (made from W or LaB₆) which emit electrons using only heating of the filament.

When the electron has been emitted, it is accelerated to the desired energy using high voltage (commonly 80-300 kV in modern TEMs). This is followed by focusing onto the sample. This first part of the lens system can be referred to as the *illumination system*: the gun, apertures and lenses responsible for bringing the electrons onto the sample. Smaller apertures will make use only of well-defined electrons, while substantially reducing the intensity.

The next part of the microscope is the *imaging system*, which includes the sample and the most important lens in conventional TEM: the *objective lens* (OL). This lens

is responsible for the majority of the magnification and its focusing quality hence plays a vital role in the performance of the microscope. In section 3.4, the main lens aberrations are presented, and most important to correct for are the ones from this lens. Finally, additional lenses of the *projection system* bring the transmitted electrons to the intended detectors, commonly first a fluorescent screen, at which screening of the sample and adjustments are made, before raising it and exposing a CCD camera to the electrons to record the data. Non-pixelated detectors are generally used for recording the signal in scanning TEM (STEM, section 3.5). These detectors only measure intensity per pixel scanned and does not provide a whole image per pixel. However, newer techniques have introduced pixelated detectors also for STEM, which is useful in advanced phase-retrieval methods as the whole 2D scattering from one point can be recorded [55].

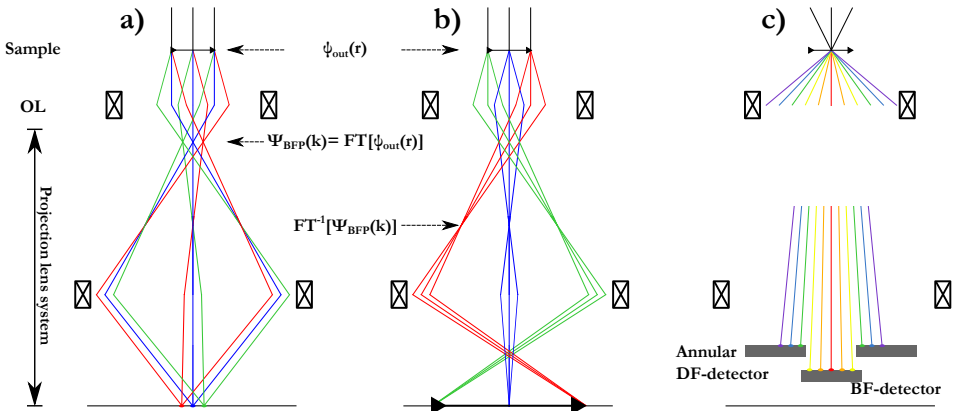


Figure 3.2: a)-c) shows three modes of operating the TEM used in the thesis. a) shows electron diffraction with a parallel incoming beam which results in a diffraction pattern in the back focal plane (BFP) of the objective lens. This plane is then imaged onto the detector at the bottom. b) on the other hand, shows exactly the same incoming wave but instead the image plane of the objective lens is imaged onto the detector, resulting in a magnified image of the sample. The difference being in the strength of the lens after the objective lens. Note for both these cases how the lines of same color coincide at the detector. The objective lens performs a Fourier transform (FT) of the incoming signal, formed at the BFP. Continuing to the image plane this transform is inversely transformed (FT^{-1}) back to real space. Finally, c) shows the concept of STEM, where a focused beam hits the sample and the differently scattered electrons are projected onto the annular (DF) and BF-detectors. The projection lenses define which angles end up on which. Figure adapted from [25].

Figure 3.2 shows different modes of operations for the TEM where the difference is in the settings of the illumination and projection lens systems. For electron diffraction and imaging (figure 3.2a and b) the illumination system provides a parallel beam onto the sample while for STEM the beam is focused to a point. The difference between the diffraction and imaging mode depends on what planes on the optical axis is focused onto the detector. For diffraction, the back focal plane of the objective lens is chosen, providing information on what crystal plane distances are present in the sample through Bragg reflections [2, pp. 201-207]. However, for imaging, the chosen plane is the image plane of the objective lens. In STEM, the projection lenses

dictate which angles are detected at which detector, the direct detector or the annular one (see figure 3.2c), and can thereby dictate which information is recorded (more in section 3.5). For this thesis the modes used are imaging, for high resolution data and crystal structure analysis, and STEM for tomography (chapter 4) and compositional analysis mapping (section 3.7). The diffraction mode has mainly been a useful tool for tilting the crystal to the correct zone-axis.

3.2 Produced signals

The incoming electron can interact with the sample it is entering. However, it is likely that an electron passes through the sample without any interaction (assuming the sample is of the correct thickness for TEM-analysis), and only a small chance of scattering. When an electron scatters elastically it keeps its energy, but its direction can be deflected, usually when interacting with the nuclei of the sample atoms. Inelastic scattering is the kind of scattering events that cause the electrons to lose energy through interaction with the electrons and the electron states in the sample. Here, the coherence of the electrons is lost. However, these interactions and the amount of lost energy of the electron is indicative of the chemistry in the sample. Exiting the sample, hence detectable, are a multitude of signals:

- The unaffected electrons
- The coherently elastically scattered electrons at angles depending on the periodicity of the sample (Bragg scattering [2, pp. 197-208])
- The incoherently elastically scattered electrons at high angles (HAADF in section 3.5)
- The inelastically scattered electrons that have lost energy due to excitation of electrons in the sample (used for spectroscopy, but not in this thesis)
- The secondary x-rays which are formed after the previously mentioned excitation event (XEDS in section 3.7)

3.3 High-resolution TEM

The contrast in an image acquired in conventional TEM mode can depend on multiple factors. High resolution stems from using the wave-properties of the electrons and achieving phase contrast in the images [54, pp. 211-218]. However, first we consider

other forms of contrast possible. Absorption contrast is the simplest one to understand conceptually since it is essentially a shadow cast onto the image. Denser and thicker materials absorb/scatter electrons more, which will be translated into darker areas in the image (achieving mass-thickness contrast) [54, pp. 196-201]. In addition, diffraction contrast is possible. This stems from the wave-properties of the electrons which diffract when encountering a repeating lattice producing Bragg intensities (diffraction pattern) in the back focal plane (see figure 3.2). It is possible, using an aperture (objective aperture), to only include parts of the diffraction pattern, e.g. specific intensities. Hence, only areas responsible for that intensity will show up in the image. The imaging is referred to bright-field (BF) if the central spot is included and dark-field (DF) if it is not.

High-resolution TEM however relies on the detection of the weak phase shift the electrons experience when passing through the potential of the sample, hence called phase contrast [54, pp. 211-218], and this is vital since the absorption, and thereby the absorption contrast, is minimal for thin samples. If the sample is sufficiently thin the amount of absorption can be neglected and the electron wave passing through only experiences a phase shift, as a function of the potential it passes through [2, p. 486]. This effect is assumed weak for thin samples, referred to as the *weak phase object approximation*, WPOA, meaning most of the intensity will remain in the direct beam ($\mathbf{k}=0$) [2, p. 486]. In Appendix A on page 161 a longer derivation is shown while here only the concepts are discussed:

A wave of electrons ψ passing through the column, without a sample, has an amplitude (A_ψ) and a phase (ϕ), $\psi = A_\psi e^{i\phi}$. When detected as an intensity however, the phase is lost:

$$I_i = |\psi_i|^2 = \psi_i \psi_i^* = A_\psi^2 \quad (3.1)$$

The incoming wave is normalized, and the phase is set to 0 ($\psi_{in} = 1e^{i0} = 1$). For phase contrast imaging the aim is to retrieve the phase shift caused by the sample ($e^{-i\sigma V_t(\mathbf{r})}$), where the factor $\sigma V_t(\mathbf{r})$ describes how the shift varies as a function of position on the sample, \mathbf{r} (V_t being the projected potential, i.e. what we want to image). The wave exiting the sample can now be described as:

$$\psi_{out}(\mathbf{r}) = \psi_{in}(\mathbf{r})e^{-i\sigma V_t(\mathbf{r})} = e^{-i\sigma V_t(\mathbf{r})} \approx 1 + (-i\sigma V_t(\mathbf{r})) \quad (3.2)$$

By using the assumptions of the sample being very thin and only contributing with a phase shift the wave can be described as a direct beam (1) and a scattered beam ($-i\sigma V_t(\mathbf{r})$). Figure 3.3a illustrates this exiting wave in the complex plane with a unit circle (*Argand diagram*). The red vector shows the direct wave ($1e^{i0} = 1$) while the blue vector shows the scattered part ($-i\sigma V_t(\mathbf{r})$) at a certain \mathbf{r} . When the objective lens focuses the scattered beams into a point \mathbf{r}' on the image plane, the wave is once

3 Transmission electron microscopy

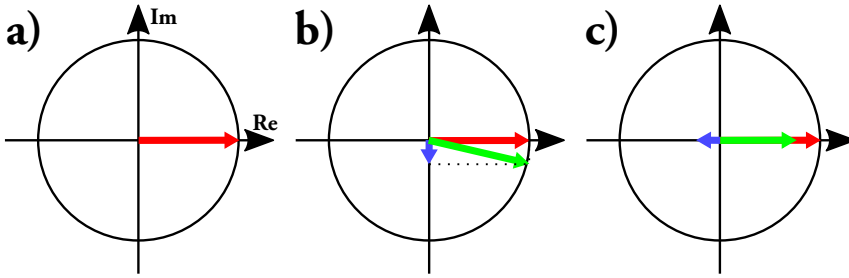


Figure 3.3: Argand diagrams in the complex plane to illustrate the electron wave passing through a sample. a) The initial incoming wave is assumed normalized and plane (red vector, amplitude: 1 and phase shift 0). b) Scattering can occur to the wave when passing the sample, described as a small phase shifted part (blue vector). The resulting wave after the sample is described by the interaction of the direct beam, which is assumed unchanged in amplitude, and the phase shifted scattered wave. This resulting wave will have negligible effect on the intensity. c) However, if the scattered waves are phase shifted a further $-\pi/2$ the amplitude will be directly decreased and hence the intensity goes down. Phase contrast!

more described as direct plus scattered beam. This case is shown in figure 3.3b and the resulting vector is shown in green. However, when the intensity in this point \mathbf{r}' is calculated, according to equation 3.1, it will not differ much from the case of $\psi_i = 1$, i.e. no contrast will be caused by the phase shift.

Phase contrast imaging instead relies on the scattered component (blue vector in figure 3.3) subtracting from the direct beam, creating a darker contrast in an image point \mathbf{r}' , which relates to the point on the sample \mathbf{r} at which the initial phase shift occurred. This would look like in figure 3.3c which results in a shorter green vector describing the recorded electron wave at the image. The detected intensity (remember equation 3.1) depends on the amplitude squared which will now be reduced. Phase contrast has been achieved. In order to get the case in figure 3.3c all scattered electrons must experience a phase shift of $-\pi/2$ radians relative the direct beam and it falls on the objective lens to perform this shift.

The scattered electron wave $\psi_{out,s}$ is affected as a function of \mathbf{k} , which is the spatial frequency. The smaller the details in the image, the larger the \mathbf{k} , and the higher the scattering angle into the objective lens, which means different paths depending on the spatial frequency information carried in that beam. As seen in figure 3.2 the back-focal plane of the objective lens describes a Fourier transform (\mathcal{FT}) of the information in the sample. The scattered wave can hence be described using a Fourier transform (equation 3.3) which clearer describes the transfer of information since it is a function of \mathbf{k} . The larger features are described by small \mathbf{k} and the finer details in the imaging require the higher \mathbf{k} s to fully describe them. The transmission of the scattered wave through the objective lens is described by some additional factors according to equation 3.4.

$$\Psi_{out,s}(\mathbf{k}) = \mathcal{FT}[\psi_{out,s}(\mathbf{r})] \quad (3.3)$$

$$\Psi_{BFP,s}(\mathbf{k}) \longrightarrow A(\mathbf{k})D(\mathbf{k})e^{i\chi(\mathbf{k})}\Psi_{out,s}(\mathbf{k}) \quad (3.4)$$

Here $A(\mathbf{k})$ describes a cutoff at which higher angles are not transmitted. This is done by introduction of an aperture in the back-focal plane (mathematically a top-hat function that sets all frequencies, \mathbf{k} , above certain value to 0). The dampening function $D(\mathbf{k})$ is a collection of functions that describes an envelope of dampening higher frequencies. This is due to chromatic aberrations (due to energy spread of the electrons) or spatial coherence due to imperfections in the gun. The most important part however is the phase shift factor $\chi(\mathbf{k})$ (section 3.4). The calculations of the detected intensity at the image simplifies to equation 3.5 which makes sense in light of figure 3.3. If the phase transfer term $\chi(k)$ is 0 the phase information σV_t is not transmitted ($\sin(\chi) = 0$). However, if the term adapts to the ideal transferred phase shift of $-\pi/2$ the intensity is reduced as $\sin(\chi) = -1$.

$$\mathcal{I}_i(\mathbf{k}) = \delta + 2\sigma\hat{V}_t A(\mathbf{k})D(\mathbf{k})\sin(\chi(\mathbf{k})) \quad (3.5)$$

3.4 Aberrations and correction of these

$\sin(\chi)$ is known as the *phase contrast transfer function*, pCTF (or just CTF), which gives an expression describing how the microscope transmits the different waves for different \mathbf{k} s. Deviation from transfer without phase shifts are called *aberrations*. However, for phase contrast we want a transfer at $-\pi/2$. The term $\chi(\mathbf{k})$ describes these shifts and is a sum of factors. These factors describe symmetries of the phase changes and are collected in Appendix B on page 163 [56]. Equations 3.6 and 3.7 describe the summation from Appendix B where the most prevalent factors for an uncorrected microscope are C_1 and C_3 , *defocus* and *spherical aberration* respectively. The sum according to equations 3.6 and 3.7 for just C_1 and C_3 gives equation 3.8.

$$\chi(\mathbf{k}) = \frac{2\pi}{\lambda}W(\omega), \quad \omega = \lambda\mathbf{k} \quad (3.6)$$

$$W(\omega) = \Re \left\{ \sum [Aberration\ factor] \right\} \quad (3.7)$$

$$\hat{\chi}(\mathbf{k}) = \pi C_1 \lambda \mathbf{k}^2 + \frac{1}{2} \pi C_3 \lambda^3 \mathbf{k}^4 \quad (3.8)$$

As seen in figure 3.4 the pCTF adopts different characteristics depending on how the defocus C_1 is chosen. In the ideal case (figure 3.4a) the pCTF becomes -1 (or close to it) for as large a band of different \mathbf{k} as possible, hence letting the phase contrast contribute fully to the image formation. However, this is not achievable in a real case and the pCTF oscillates across $\sin(\chi) = 0$, which means that some frequencies will in fact have the reversed effect on the intensity in the image, which is obviously

3 Transmission electron microscopy

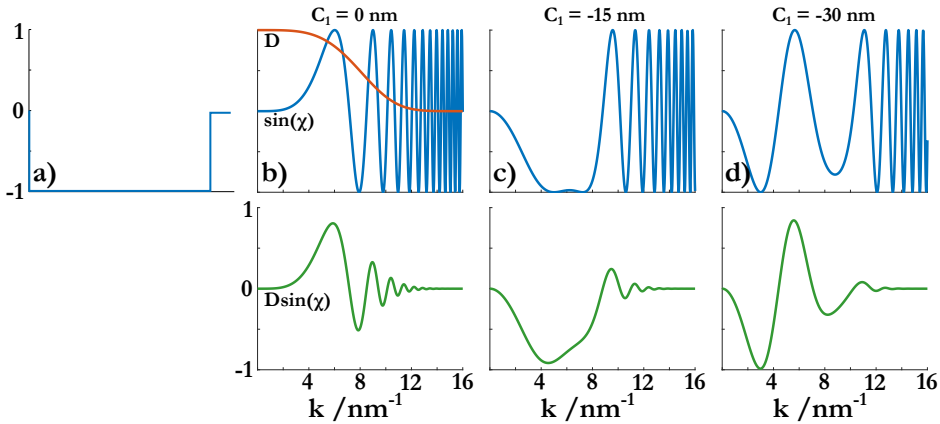


Figure 3.4: The pCTF illustrated in 2D for the case in equation 3.8. a) shows an ideal pCTF where $\sin(\chi)$ equals -1 and is doing so for a large band of k . b-d) show real examples from different settings of C_1 , defocus. The bottom green curves show how the function looks if the dampening function $D(k)$ (red curve in b)) is included. Image adapted from [25].

non-ideal. C_3 is a fixed value for uncorrected microscopes, given by the lens setup. In this case the ultimate setting is achieved by balancing the spherical aberration with the defocus (equation 3.8) to obtain something close to figure 3.4c, where an as large as possible band of k are transmitted. Such an optimized focus is called *Scherzer focus* [2, pp. 490-491]. When the defocus is changed too much the band decreases in size (figure 3.4d). When the pCTF crosses $\sin(\chi) = 0$ no transmittance occurs and these spatial frequencies are lost. This point at which the pCTF crosses 0 for the first time is referred to as the *resolution limit* [2, p. 490].

If the TEM is *aberration corrected* however, as in the case of the Hitachi HF-3300 ETEM in Lund, introduction of non-symmetrical lenses (quadrupoles, hexapoles and octupoles) can distort the electron wave in such a way that aberrations are reduced [57] (figure 3.5). This corrector is installed below the sample to correct for the aberrations introduced by the objective lens. Minimization of the aberrations is vital for highly resolved images [58]. The simple case in equation 3.8 and figure 3.4 does no longer hold and more aberrations have to be accounted for when C_3 is reduced. The aberrations both depend on higher orders and non-symmetric factors [56, pp. 221-222]. Practically at the TEM it is important to know about what aberrations are present, either for an uncorrected microscope so that defocus can be selected correctly or for a corrected microscope to use the calculated defocus given by the corrector software.

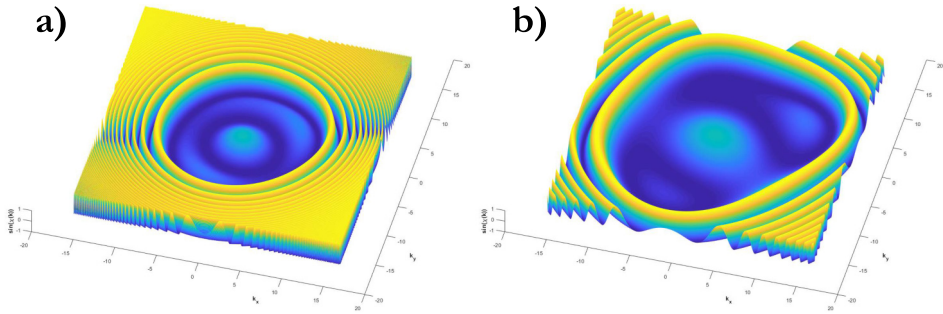


Figure 3.5: An illustration of how the pCTF looks in 2D, comparing uncorrected (a) and corrected (b) functions. Turquoise shows where the function is close to zero and no transfer of spatial information occurs. a) shows a symmetric case which is limited by the spherical aberrations illustrated in figure 3.4 while b) shows a case where spherical aberration has been reduced and now non-symmetric and higher order aberrations dictate. The band (area) of transmission is enlarged and the resolution limit is increased for all directions. Image adapted from [25] and the script for plotting these are included as Appendix C, page 165.

3.5 Scanning TEM

In scanning TEM mode, compared to the conventional TEM, the quality of the image depends mostly on the illumination system. The image is formed by scanning a fine probe of electrons across the sample and measuring intensity of the signals as a function of position. The magnification of the image will depend on the size of the scanned area and the resolution will depend on the distance between each pixel in the image and how broad or deformed the probe is.

Many TEMs have the capability to switch between CTEM and STEM, which means the techniques can be used to complement each other. For instance, the commonly higher resolution of CTEM (for microscopes not equipped with aberration correctors) can be complemented by compositional mapping performed in STEM. This has been used in this thesis in paper I and II, where the CTEM images with crystal structure information has been used to complement the non-lattice resolved tomograms. However, with the introduction of *probe correctors* (aberration correctors for the probe, positioned above the sample) routine atomic resolution STEM imaging is possible, with the drawback of slow image acquisition and noise compared to CTEM. This has made it useful to produce dedicated STEM units, which only operate in scanning mode. The scan itself can also be affected by disturbances, for instance electrical fields and vibrations, which lowers the image quality. Successful attempts have been made to remove these scan-disturbances through post-processing [59].

As the resolution in STEM mode depends on how small the probe can be made, it is the aberrations in the illumination system that dictates the resulting resolution. Deviations from an ideal spherical wave front will reduce the quality of the image, just as for CTEM. Those aberrations now prevent the system from forming a well-

3 Transmission electron microscopy

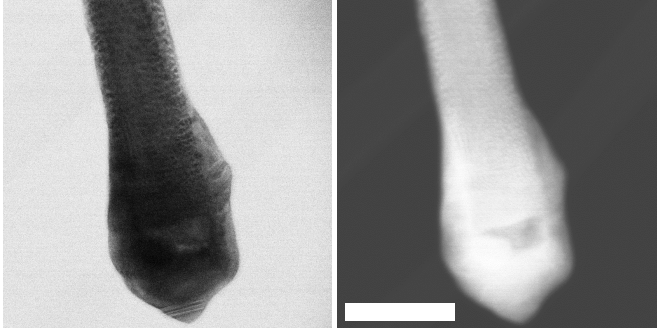


Figure 3.6: An example on how bright-field (BF, left) and dark-field (DF, right) differs in contrast, mainly inverted. The imaged nanowire end shows some faint diffraction contrast (stripes at the bottom-tip) in the BF image. Since these are not visible in the DF image, the collection angles might be sufficiently high to be considered HAADF. Image adapted from [25] (scalebar: 100 nm). Image courtesy: Daniel Madsen.

defined point onto the sample. Instead, the probe is slightly enlarged and deformed (how much depending on the aberrations), which means the probed area is slightly smeared and possibly unevenly spread. The probe corrector fixes this and has provided substantial improvement in resolution for STEM [60].

Finally, the intensity detected at each pixel depends on the detector. As seen in figure 3.2, the projection lenses bring the scattered electrons to detectors that either could be placed in the direct optical axis or annularly around the same axis (bright-field, BF, and annular dark-field, ADF, detectors respectively). Depending on the detector (and what collection angles are set by the projection lens system), the information collected differs. When the probe is not passing through anything in its path, the electrons will not scatter, and all the intensity will fall on the bright-field detector (conversely the intensity will be zero on the dark-field detector). When an object is inserted into the path of the beam, the electrons scatter. The intensity will drop at the BF detector and some will show up at the DF detector. The same object is imaged using both techniques in figure 3.6, which highlights the differences. Importantly, the collection angles should be chosen carefully to include the contrast sought. In the BF images and DF with low collection angles, the intensity will depend on density but also diffraction contrast from crystalline objects. A common method for easily interpreted STEM images is to use ADF and select large enough collection angles not to include the diffracted intensities from the sample, hence only collecting highly scattered electrons (> 50 mrad). This is referred to as *high angle ADF* (HAADF) and its intensity is purely based on the density and thickness of the material [2, pp. 379-381]. When STEM is used throughout this thesis, HAADF is the imaging mode, e.g. for electron tomography in papers I and II.

3.6 Sample preparation

One of the requirements for a sample in the TEM is that it is sufficiently thin. Electrons should be able to pass through the sample with some interaction and the amount of interaction needed/wanted depends on the application. For instance, the thinner the sample, the higher resolution in atomic imaging since the resolution is purely phase contrast, and absorption contrast is minimized [2, pp. 486-487]. However, for analytical purposes (see chapter 3.7) a thinner sample produces less signal (low signal-to-noise-ratio) so a thickness must be chosen for the specific purpose of the acquisition.

All samples analyzed in the included papers in this thesis are nanowires and such structures are on the order of about 5 to 200 nm [38]. This is thin enough for the accelerating voltages used (200-300 kV, however not for pure phase contrast). Hence, the preparation is rather simple and includes mechanically transferring them. In more simple terms, the preparation I have performed includes pressing the Cu TEM-grid onto the substrate and dragging it along the surface while pushing down to break off the wires. An alternative method is to use a tissue (that does not shed fibers, like a cleanroom tissue) with a cut sharp corner, which can be used to transfer the wires from a specific position on the substrate to the TEM-grid. Indeed, a simple method.

Alternatively, more elaborate methods of sample preparation include mechanical thinning methods, or using a focused ion beam to polish the sample thin enough [61]. The focused ion beam (FIB) instrument combines the imaging mode of an SEM with a source of ions (for instance Ga or Ar [61]) that are used to polish thin lamellas of a bulk sample otherwise not electron transparent. Using high energy ions (substantially higher than the electrons from the SEM) to do the major cuts, followed by lowering the voltage for the polishing, the damage on the sample can be minimized and the desired thickness can be achieved (down to a couple of nm [61]).

3.7 Compositional analysis

As mentioned in section 3.2 the electrons can interact in different ways with the sample. In a TEM there are multiple ways to detect composition, which is used among others for papers VI and VII. This is due to the electrons' interaction with the sample and not all of these being elastic. Compositional and even bonding information can be achieved by analyzing the signals from inelastic events. The more common methods used are *electron energy loss spectroscopy*, EELS and *x-ray energy dispersive spectroscopy*, (X)EDS [62]. The former detects the primary electrons as they have passed through the sample and measure their loss of energy. This loss can be characteristic

3 Transmission electron microscopy

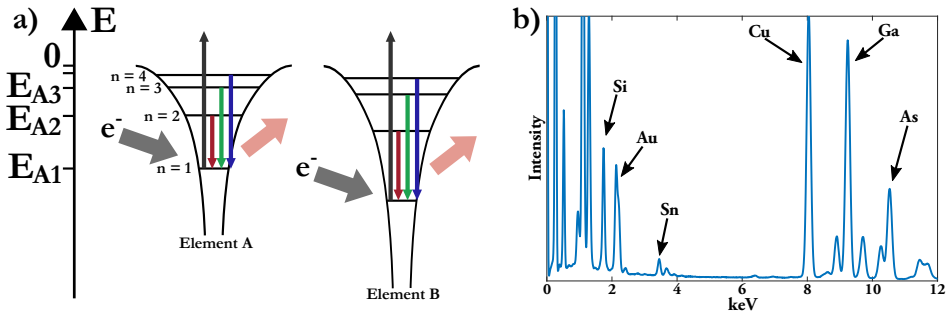


Figure 3.7: Illustration of how the XEDS signal is created and what it looks like. a) An incoming electron (e^-) can excite core-state electrons from their energy level. Electrons with higher energy-states can then take its place by releasing energy in the form of an x-ray photon. The energy of this photon is indicative of the element as the energy levels are discrete and different (compare element A and B). b) The emitted x-rays are detected as a spectrum where the peaks can indicate the presence and concentration of an element. (Figure adapted from [25])

of many different parameters: thickness of sample, bonding arrangements, hybridization, bandgaps (for semiconductors) and also the elements [63]. This requires some form of energy filter that can bend the path of the electrons, which will highly depend on their energy. The electrons are then collected as a function of how much they have been deflected, as a spectrum [54, pp. 115-118].

However, the method used during this thesis work has been XEDS, a technique which detects secondarily emitted x-rays from the sample during electron illumination. Here, the electrons interact with core-state electrons, exciting them above the threshold of the work function and an empty electron-state is formed. This is quickly filled by a higher energy electron, which through emission of energy quanta (x-ray), fills the empty site. The emitted x-ray is characteristic of the element, as different elements have different energy levels [2, pp. 581-584] (figure 3.7). All the x-ray photons are collected and form a spectrum, in which peaks of intensity indicates presence of certain elements and their relative intensity can be correlated to certain concentrations of the respective elements [2, pp. 639-641]. This technique is very powerful, especially if used in STEM-mode where a spectrum is collected for each pixel in the image, making it possible to map the occurrences of elements and their relative concentration [2, pp. 658-659].

3.8 In-situ TEM

In-situ is not a method of its own but rather the concept of studying on site, used in papers III, IV and V. This is done by either adding an analytical instrument to an existing setup or adding capability to control heat, mechanical stress/strain (*microelec-*

tromechanical systems, MEMS) or exposure to chemicals in an instrument such as the TEM. A TEM with such capabilities is referred to as an *environmental TEM* (ETEM).

Heating is one of the most common parameters to control in an ETEM due to the quite simple design of such a holder. To heat the sample no moving parts or added chemicals, which can disturb the operation of the TEM, are needed. Instead, heating is achieved through resistive heating [64]. Such setups have been used for the analysis of phase transformations [65–67], melting [68, 69] and degradation [67, 70, 71] among others. Mechanical forces have also been added to samples [72]. Doing this while observing at atomic resolution has made it possible to study atomistic behavior during strain [73, 74], crack-propagation [75] and fracturing [76]. Chemical reactions can be recorded by controlling liquids or gases, sometimes combined with heating, to be inserted at the observed sample.

Controlling such parameters, one still has to remember the delicate nature of the TEM. It should operate in high vacuum and space is restricted due to the precise placement of electromagnetic lenses. A couple of the considerations to remember when designing ETEM-setups are that it should:

- Be small enough to fit in the designed position of the sample
- Be precise enough to perform the mechanical, heating or chemical adjustments on the sample with precision
- Be electron transparent to allow high resolution imaging and potentially allow for compositional analysis (i.e. not blocking emitted x-rays for XEDS)
- Not affect the beam or other detectors by introducing larger magnetic or electric fields
- Not disturb/destroy the vacuum system or components requiring high vacuum, e.g. the electron gun

When it comes to controlling the environment around the sample, special *in-situ* holders are common. These holders can (in the case of liquids, and often also gases) have an enclosed volume (cell) with electron transparent windows for observation. In this, the environment can be controlled, either by inserting liquids or gases [77–79]. Since the new environment does not affect the TEM vacuum these can be adapted to already existing microscopes. However, the setup used in this thesis (figure 3.8) does not operate using holders with cells. Instead the high-resolving TEM (aberration corrected, spatial resolution down to 86 pm in CTEM) is designed to manage the inserted gases through pumping. Gases can be inserted via a gas-handling system and entering close to the heated MEMS-chip where the sample is placed on thin SiN_x

3 Transmission electron microscopy

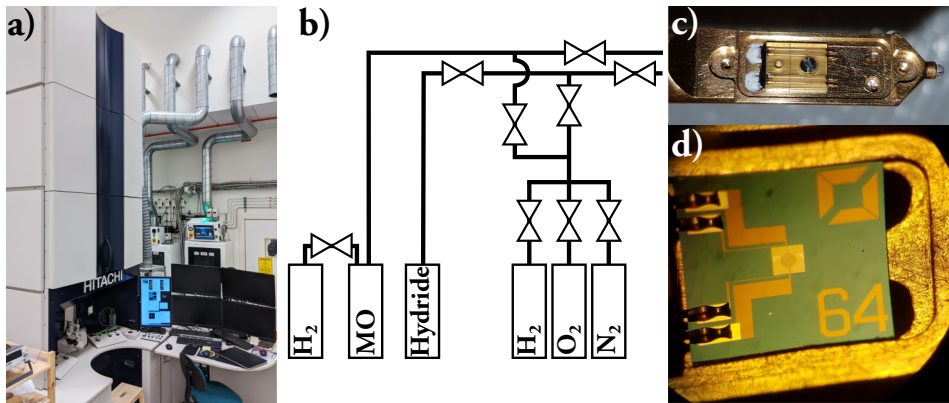


Figure 3.8: a) The ETEM in Lund specially made for *in-situ* studies of nanowire growth. b) A simple sketch of how the different precursor sources, metal-organics (MO), hydrides and H₂/N₂/O₂ are connected to the holder. The MOs are inserted using bubblers in which H₂ is used as a carrier gas. c) A holder tip where the gas-lines end up and d) a holder with a heating-chip mounted. Image courtesy (c-d) Daniel Madsen.

windows, with holes for high-resolution observation. Hence, this setup still fulfills the requirements from the list above without using a closed cell. The focus of the microscope is on the study of III–V semiconductors and the idea is to keep these precursors, the III and the V, separated until they reach the sample (shown in the very basic sketch in figure 3.8b). The setup is constructed to be as similar as possible to an industrial CVD-setup. Other gasses, such as N₂, H₂ and O₂ can be added as well, which means the setup can be used to study phenomena such as oxidation and reduction or burning of carbon allotropes [80]. Figure 3.8b shows a very basic sketch on how the CVD system (hydride-source and metal-organics, MO, with a hydrogen flow through the bubbler) connects to the holder tip and how this tip looks at close-up (with and without the heating chip, figure 3.8c and d respectively).

Chapter 4

Electron tomography

Using the TEM as a high-resolving tool has been and still is vital for many applications, solving atomic arrangements, morphologies and identifying defects. However, an inherent drawback of TEM is the fact that the analysis is performed as a projection through a sample. Even though samples need to be thin, and for the HRTEM theory presented in section 3.3 very thin, many samples exhibit changes along the projected volume. This chapter will present the theory and concept of *electron tomography* (ET) and correlate that to the more commonly known x-ray tomography. First the concept and the mathematical background of both acquisition and reconstruction are presented in sections 4.1 and 4.2, followed by sections on how this is practically performed in the TEM in sections 4.3 and 4.4. Finally section 4.5 will briefly mention the kind of post-processing performed on the tomographic reconstructions in this thesis.

4.1 The principle of tomography

Since the word tomography only refers to the data produced (tomo: slice/section, graph: to write something) an easier way to visualize the tomographic process is to look at a tomograph more commonly used than an electron microscope. At hospitals, a method of internal imaging of patients is the technique of *computed tomography* (CT, sometimes referred to as *computed axial tomography*, CAT-scan) [81, 82]. In such a machine, the patient is imaged from all directions. In fact, the toroid design houses an x-ray emitter and on the opposite side a detector, which are rotated and continuously passing x-rays through the patient [83, p. 1-2]. After such a session (or in parallel

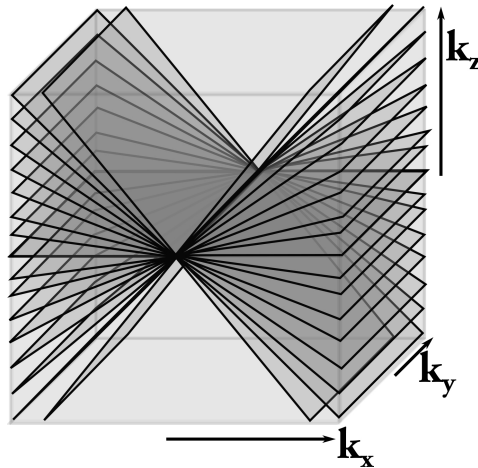


Figure 4.1: Fourier space illustrated with its coordinates k_x , k_y and k_z . The shown planes illustrate how different projections will probe this space (as a slice perpendicular to the projection direction). This results in a tilt-series only probing discrete positions in the Fourier space and further from the center (high resolution information) it is probed even more sparsely.

for modern machines) the individual projections are calculated *backwards* to get a 3D-reconstruction, a *tomogram*, of the original object, in this case the patient.

The many projections of one object, acquired from different projections reveal the changes in the projected direction otherwise missed from single projections. The data from a single projection visualizes the spatial frequencies perpendicular to the projection, as discussed in chapter 3.3, while spatial frequencies along the projection are not seen. Extending the Fourier transform to 3D, also the spatial frequency space is 3D, and when acquiring a single projection image, a slice of the Fourier space is recorded, according to the *Fourier slice theorem* (figure 4.1) [83, pp. 194-195]. Thereby, when multiple projections are recorded, we also start to record a larger part of the Fourier space. The more of these different projections acquired, the less ambiguous the reconstruction becomes. Thus, the quality of the reconstruction improves when using more projections, smaller tilt-increments and a larger tilt-range. This makes sense since an infinite amount of images at all angles will continuously probe the whole of the Fourier space (out to the resolution limit of the microscope). Note that (also in figure 4.1) the further from the center of the Fourier space, the larger the gaps are between the slices. This means the higher resolution components are sampled worse than the low resolution ones, deteriorating the reconstruction [84]. In addition, there might potentially be obstacles to fully rotate the sample $\pm 90^\circ$. This might be due to shadowing or limits on the rotation stage and it results in a large part of the Fourier space not being probed at all. In figure 4.1 this is seen as a wedge at the top and bottom not being probed and is referred to as *missing wedge of information* [82]. This missing data will cause smearing in that direction.

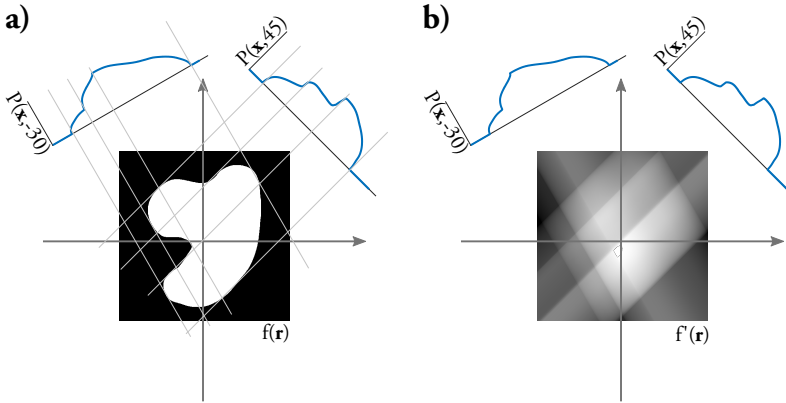


Figure 4.2: An illustration of how the Radon transform is performed. a) shows how the projected intensity of $f(\mathbf{r})$ falls onto two projected lines, one at -30° and the other one at 45° . As described in equation 4.2 the intensity is described as a function $P(x, \theta)$. b) shows the opposite case where these two projections $P(x, \theta)$ are backprojected according to equation 4.3, creating an image $f'(\mathbf{r})$. This backprojected image will not be similar to $f(\mathbf{r})$ due to only two projections being used.

Similar to the Fourier transform, which maps the spatial frequencies of a signal in real space to its frequency components in reciprocal (frequency) space, the process of tomographic acquisition is described with the *Radon transform* (\mathcal{RT}). An object in object space is described by its intensity in a certain property (for instance density) as a function of position (coordinate) $f(\mathbf{r})$. As the Radon transform describes the projected intensities of this object as a function of detector position and projection angle it can be written as (transformed to) $P(\mathbf{x}, \theta)$. The dimensionality of \mathbf{x} is one less than of \mathbf{r} (for example an 3D object, described by the coordinate \mathbf{r} , is projected onto a 2D image, described by the coordinate \mathbf{x} , equation 4.1). The mathematical definition of the Radon transform for a 2D object projected onto 1D (and the inverse transform) is shown in equation 4.2 (and 4.3). This was published by Johann Radon in 1917 [85, 86] (second reference is the translated version, 1986, of the first) adapted for astronomy [87] and later medical imaging [88].

$$P(\mathbf{x}, \theta) = \mathcal{RT}[f(\mathbf{r})], \quad \mathbf{r} \in \mathbb{R}^n, \quad \mathbf{x} \in \mathbb{R}^{n-1} \quad (4.1)$$

$$P(x, \theta) = \iint f(\mathbf{r}) \delta(r_1 \cos \theta + r_2 \sin \theta - x) d\mathbf{r} \quad (4.2)$$

$$f'(\mathbf{r}) = \iint P(x, \theta) \delta(r_1 \cos \theta + r_2 \sin \theta - x) dx d\theta \quad (4.3)$$

Figure 4.2 shows how equations 4.2 and 4.3 work in practice, producing a projection of the object onto an image. This means the acquisition of the tilt-series is the Radon transform and the reconstruction $f'(\mathbf{r})$, the calculations performed, are based on the inverse transform.

4.2 Algorithms

Equation 4.3 describes the *backprojection* (BP) performed to recreate the already projected object. However, such a simple operation will have difficulty in recreating advanced structures of the object. Since the BP adds the intensity of each projection at all positions along the projection, smearing will be seen. Again, figure 4.1 shows how high resolution components (high k) values of Fourier space are probed sparsely, producing a subsequently essentially low-pass filtered (blurred) reconstruction [89]. A commonly used measure for this is to high-pass filter each projection before BP. Such a high-pass filter can be adjusted to ones needs and the technique is simply called *filtered backprojection* (FBP) [83]. Here, edge features become more pronounced in each projection and hence also in the resulting tomogram. A comparison of some algorithms can be seen in figure 4.3 where the advantage of FBP over BP can be clearly seen. Both for BP and FBP the absolute value in each pixel depends on how many projections were performed and does not relate to the specific property imaged, which can be a drawback in quantitative analysis.

The interest in improving the reconstructions have led to extensive development of additional algorithms which can both reconstruct with less artefacts and reduce the effects of noisy projections, large missing wedge or larger tilt-increments [90–92]. Luckily, the algorithms work independently of the signal, and algorithms developed for x-ray tomography can also be used for electron tomography and vice versa [93]. Throughout this thesis the ASTRA toolbox, a free scripting toolbox for Python and MATLAB [94–96], has been used for applying the reconstruction algorithms.

Iterative techniques have gained popularity due to their capability to improve the tomogram through computing the difference between the original projection images and the resulting reconstruction [97], which is becoming easier with more powerful computers. Through backprojection and reprojection multiple times, a reconstruction that better fits the projections can be found, and this generally happens after 20-40 iterations [98, 99]. The most common one of these is the *simultaneous iterative reconstruction technique* (SIRT) [100]. It projects (Radon transform) the initial reconstruction back at the same tilt-angles as the original projections and compares the projection images. This difference is then inversely Radon transformed to describe the error in the reconstruction as a function of position $C_{\theta}^{q+1}(\mathbf{r})$. This value C is then averaged, \bar{C} , for all the projections θ and the pixel (or voxel) value in \mathbf{r} is updated. This process is repeated iteratively according to equation 4.4 where q denotes the current reconstruction and $q + 1$ the updated, after the iteration [100].

$$f'^{q+1}(\mathbf{r}) = f'^q(\mathbf{r}) + \bar{C}^{q+1}(\mathbf{r}) \quad (4.4)$$

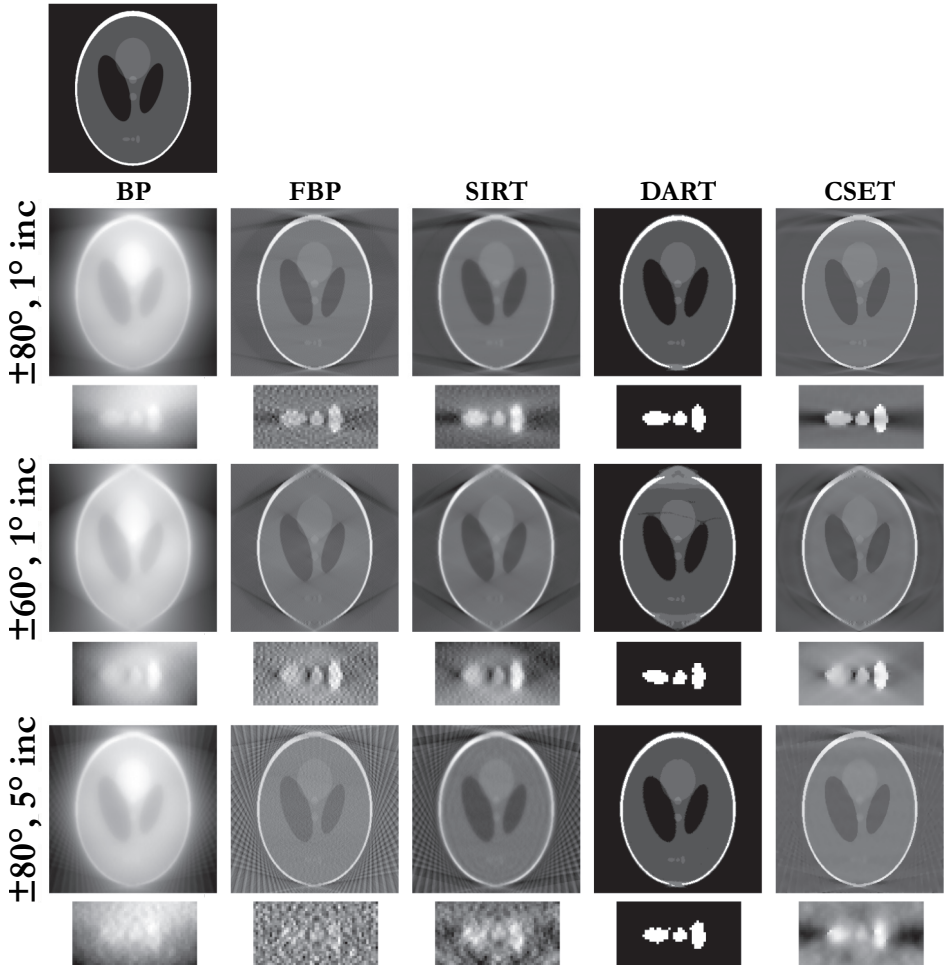


Figure 4.3: A comparison of the different algorithms used in this thesis. For different tilt-range and tilt-increments between the acquisitions, the five algorithms are shown reconstructing the 2D phantom shown at the top-left. Below each reconstruction a small area containing small weak-contrast features are shown (with auto-adjusted gray-scale).

SIRT can improve the reconstruction relative to FBP (figure 4.3), especially when fewer images are used or for noisier original projections (see the slight improvement when comparing the lower images of FBP and SIRT in figure 4.3). However, the effect of the missing wedge (the pointed top and bottom of the phantom in figure 4.3) can still be seen. In comparison to FBP and BP the pixel (or voxel) value in SIRT will relate to the physical property imaged. If the projection is of an object $f(\mathbf{r})$ the reconstruction will produce a resembling value in the same location of the reconstruction ($f'(\mathbf{r}) \approx f(\mathbf{r})$).

Another iterative technique that has been proven useful is the *discrete algebraic reconstruction technique* (DART). In this case, *a priori* (already known) information is used for each iteration of the reconstruction. The intensities in the sample and hence the tomogram is assumed having only a few discrete values. It uses SIRT initially and then assigns each pixel to a certain value. Each iteration only updates the edges between regions which in turn can have huge benefits on reducing the effect of the missing wedge (figure 4.3) [98, 101]. Obvious drawbacks however are the incapability to reconstruct gradients and the intensity levels must be known and carefully chosen. An initial SIRT reconstruction can be used to get an idea of what intensities to choose (peaks in an intensity histogram), hence giving the *a priori*. Seen in figure 4.3, the DART algorithm provides superior reconstructions for the phantom used. However, one must remember that the phantom is an ideal case with very defined intensity levels that are known, which might not be the case for real reconstructions.

Finally, an additional reconstruction technique that has been used is *compressed sensing electron tomography* (CSET) described by Leary et al [102]. This algorithm uses the SIRT algorithm which, as mentioned, in contrast to DART does not require prior knowledge of the intensity levels or the assumption that only discrete levels are present. However, it introduces penalty terms to the final reconstruction:

$$\hat{f}_{\lambda,\gamma} = \arg \min_{\hat{f}} \left\{ \|\Phi \hat{f} - b\|_{l_2}^2 + \lambda TV(\hat{f}) + \gamma \|\Psi \hat{f}\|_{l_1} \right\} \quad (4.5)$$

The final reconstruction \hat{f} is reconstructed using SIRT, but penalty terms on the *Total variation* and *L1-norm* are introduced so that the expression is minimized with some restrictions. $\Phi \hat{f}$ is the inverse Radon transform of the reconstruction \hat{f} into the domain of the initial projections b . Their difference is minimized, i.e. the expression using this first term is similar to what conventional SIRT performs. TV is the total variation, a sum of the gradients in the reconstruction, and $\Psi \hat{f}$ describes the transform of the reconstruction to a domain which is assumed sparse (many elements are 0). In many forms of compressed sensing this can be in the Fourier domain, or similar, but for electron tomography the reconstruction intensity itself can be considered sparse in the case of a clear background (value = 0) [102]. Ψ then becomes the identity matrix, a matrix containing all zeros apart from the diagonal elements which are one (multiplication with an identity matrix returns the same matrix). l_1 and l_2 denote the L1- and L2-norms respectively. Actually, the correct method would be to use the L0-norm for the last term, but it is difficult to iteratively minimize and L1 has been found to replace it sufficiently well [103]. The terms λ and γ are selected manually for the best reconstruction. The whole expression becomes a minimization of the error between the reconstruction and the original projections added with the total gradient and the number of non-zero elements. As seen in figure 4.3 the CSET reconstruction is similar to SIRT, which is expected (SIRT-based method). However,

Table 4.1: A comparison table of four of the presented techniques and their advantages, disadvantages, and how the pixel/voxel value relates to the original sample. Table adapted from [25].

Techniques	FBP	SIRT	DART	CSET
Brief explanation	A simple, high-pass filtered version of BP in order to enhance sharp features such as edges.	Iterative technique that re-projects the new reconstruction and compares with the original one in order to improve after each iteration.	Same as SIRT but with set discrete values that each voxel/pixel is assigned to.	Same as SIRT but with imposed penalties for non-zero pixels/voxels and gradients.
Voxel/Pixel value	Sum of projections, no meaning	True value related to object	Value (discrete) related to object	True value, possibly smoothed
Resolution	Improved over BP	Good	Good	Good
Missing wedge	Large effect	Some effect	Less effect	Less effect than SIRT
Heavy calculations	No	Yes	Yes	Yes(!)
Advantage	Easy, quick and relatively high contrast	Improving by each iteration	Same as SIRT, less effect from missing wedge	Similar to SIRT but with reduced streaking.
Disadvantage	Some smearing	Heavier calculations than FBP	Same as SIRT but also requires known discrete values	Heavy calculations and λ/γ must be set manually

due to the penalty terms, the reconstruction reduces the streaking artifacts (less features in the background) and some smoothing is applied. The selection of the terms λ and γ are not perfect for this example but parts of the reconstruction are made clearer than for SIRT. In table 4.1 a brief summary of all these mentioned algorithms are listed.

Important to remember is also to have each individual projection (image) shifted before performing any reconstruction. This is to account for drift or lateral shift after tilting, in order to make sure differences between each projection only depend on the observation angle. Instabilities in the holder when tilting might cause shifts, which must be adjusted. Otherwise, these can cause smearing or streaks in the reconstruction. In cryo-ET or soft-matter ET it is common to use high-contrast Au (or similar) metallic nanoparticles as markers (*fiducials*), which can both be used to track shifts and tilt-axis orientation [104]. The alignment method used in this thesis however is

an algorithm developed by Sanders et al. [105], which shifts the projections according to their *center-of-mass* (COM). The result is a series of images with minimized shifts, which can then produce better tomograms when one of the reconstruction algorithms described above (or others) are applied.

4.3 Problems with tomography in the TEM

Before exploring the disadvantages of applying tomography in the form of ET, first consider a clear advantage: how the object to be reconstructed can be treated. An apparent drawback of the CT-scanner in the medical field is that the machine should be able to operate without the patient being subjected to uncomfortable treatment (both for comfort and for running the risk of causing changes in the patient, either from gravity or stress). Hence, the x-ray setup is rotating around the stationary patient, creating mechanical disturbances (vibrations) and wear. Since the same considerations are not needed for most TEM-samples, the instrument can remain stationary and stable, and the sample is the one being rotated inside the setup.

In the TEM the sample is inserted at a very defined position along the electron path through the column. Tilting the sample is done by rotating the holder, and possibly tilting the sample in the other direction if dual-axis tomography is wanted (reduces the missing wedge to a missing pyramid) [106]. Since the sample in the TEM is most often positioned on a grid, which in turn sits on a holder, observation from 90° is not possible. Hence, inherently the tomographic reconstruction will suffer from a missing wedge. Measures have been taken, such as sawing the holder in half permitting a larger tilt-range [107]. Also, the *pole-piece gap* might be too narrow to permit large tilt as a smaller gap is beneficial for reducing the spherical aberration. Additionally, the high magnification used for electron tomography requires an exceptionally good tilting stage. Such a stage should, at eucentric height (no lateral or axial movement when tilting) provide a stable tilt without *large* (relative the imaging area) shifts over a large tilt-range. Practically this means the tilt-series in a TEM is performed with the maximal possible range with as many projections as time allows. Careful alignment and setting of eucentric height should also be used.

4.4 Signals used for reconstruction

One advantage of using the TEM for tomography is the vast amount of different imaging modes and detection settings. The detected signal in each projection will be the signal that is reconstructed in the final tomogram [62, 108] and high-resolution

data from each projection will provide high-resolving tomograms. If the projections contain compositional data, such as mapping from XEDS or EELS, each individual voxel in the tomogram will contain data of its contribution [62].

The different imaging modes and data types cannot be used indiscriminately. They must all fulfill the *projection requirement*, which states that the signal that is projected must contribute equally, no matter the observation angle. The signal intensity should monotonically depend on a physical property, e.g. density, and increase monotonically with thickness [106, 108, 109]. This poses a problem for CTEM of crystalline samples as the signal can depend on diffraction contrast, something that heavily depends on the observation angle. A reconstruction using this mode for a crystal might be filled with artifacts, such as streaks, due to certain tilt-angles producing very different intensities, and hence tricks the reconstruction algorithm [106].

Some examples of signals that can be used for tomography in the TEM are:

- CTEM, if the intensity only depends on absorption or phase contrast, such as for amorphous samples, including biological structures [109].
- STEM-HAADF, as this signal detects the elastically scattered electrons at higher angles than the Bragg-diffraction spots, hence not dependent on the crystal rotation. Also, the density will be the reconstructed signal as the HAADF signal approximately is a function of Z^2 [2, p. 378].
- XEDS-maps, as the fluorescent signal is transmitted independent on observation angle. However, considerations might be needed to account for absorption of low energy x-rays originating from positions further from the surface [110].

Having this in mind, the signal chosen for electron tomography in this thesis has been STEM-HAADF. The tomograms will provide voxel values that can be related to composition, or at least relative density, making it possible to distinguish different compositional volumes.

4.5 Post-processing

The resulting tomogram is a 2D/3D matrix with intensity values for each pixel/voxel. It is important for the subsequent analysis to know what imaging mode was used during acquisition in order to correlate the intensity data to a measurement of a physical property. As in all imaging sciences it is easy to illustrate qualitative data. Shapes and distributions can be shown visually and compared. However, quantitative data usually requires some form of processing.

4 Electron tomography

Segmentation is the process of assigning the different parts of an image/tomogram to a class. For instance, the simple case is to assign what is background and what is the sample. Also, additional segmentation-classes can be added depending on the intensity in the original image. Here it becomes clear that the quality of the reconstruction algorithm greatly affects the segmentation. For instance, streaks and noise can wrongly be assigned to a certain class. Clearly, the DART-algorithm produces already segmented data, i.e. the segmentation is part of the reconstruction, which can be of great benefit. Smoothed data from CSET and high noise tolerance SIRT can remove the segmentation error due to individual pixels and as FBP can provide clear boundaries between different regions it can be used to define edges.

The segmentation itself can be used to improve the assignment of pixel/voxel class by refining how the boundaries are drawn. *Graph-cut* is a method used to minimize the amount of boundaries between regions of different value. This is done by, similarly to CSET, adding a penalty value for creating a border [111]. If the penalty-factor is chosen correctly, the segmentation becomes natural and noisy pixels/voxels are ignored. If it is too low the segmentation becomes noisy and too high the regions become too smoothed. Segmentations of tomograms were performed both in paper I and II.

Chapter 5

Compositional mapping with short acquisitions

The *in-situ* projects at the ETEM (included papers III to v) consisted of HRTEM imaging of nanowire growth showing momentary rates at which layers of atoms were grown or removed as functions of temperature and gas-flows. In addition, compositional analysis using the electron beam and manually focusing it onto the seed particle was conducted in order to correlate the actual conditions in the seed particle to the gas flows. However, when focusing the beam no spatial information can be recorded and such a measurement will only generate a single data point on the composition, which works for studying constant conditions (such as the quasi steady-state growth of nanowires during stable conditions in paper IV). When using an ETEM, conditions can be dynamic and changes occur in the sample, which would be interesting to track.

For this project, I wanted to see if it would be possible to use the compositional mapping capabilities (XEDS, section 3.7) of the ETEM for acquiring successive frames with both compositional and spatial information. Ideally, this would be an acquisition that resulted in fully quantifiable *spectrum images* (SIs) for each frame. However, elemental mapping usually requires long acquisition times and the time-resolution therefore will be poor if high signal-to-noise ratios are to be achieved. One way would be to apply filtering to the acquired spectra to remove noise, which could result in better, more reliable analysis. For nanowires, this could give the composition in both the seed particle and the wire in parallel while also recording any major changes in growth direction or shape of the seed particle. Of course, the method will also be applicable on other materials systems. This chapter will describe the outline of this

project (section 5.1), the step-by-step method (section 5.2), simulations (section 5.3) and finally some results acquired on nanowires using this technique (section 5.4).

5.1 The idea

Inspired by papers that uses *principal component analysis* (PCA) and similar factorizations to filter spectra from noise [112, 113] I wanted to subject the noisy acquisitions through a filtration similar to such a process. PCA is a dimensionality reduction technique that finds the components that describe a dataset, sorted in order of how much they describe the dataset, and then projects the data on these components. If only the major components are used the noise is reduced and the data can be described with fewer dimensions [113].

$$\mathbf{D} = \mathbf{S}\mathbf{L}^T \approx \mathbf{S}'\mathbf{L}'^T \quad (5.1)$$

Where the original data \mathbf{D} can be described by the *score matrix* \mathbf{S} multiplied with the known components \mathbf{L} , the *loading matrix*. \mathbf{L}' describes only the major components of \mathbf{L} . In the case of spectrum imaging (XEDS) the components are intuitively, which has also been shown [113], the different elements or combinations thereof. The idea is then to, through a few known components \mathbf{L}' , filter the noisy data acquired from the short acquisition time. The known components are acquired by performing *non-negative matrix factorization* (NMF), a non-negative version of PCA [62, 114], on longer maps (either acquired beforehand or after the *in-situ* acquisition). From the theory of compressed sensing presented in the case of tomography (CSET) [102] I introduced penalty terms for the fitting of the known components. Hence, smoother results are obtained, and overfitting of the components is reduced [115]. The minimization for each frame becomes:

$$\mathbf{S}'_{\lambda,\gamma} = \arg \min_{\mathbf{S}'} \left\{ \|\mathbf{S}'\mathbf{L}'^T - \mathbf{D}\|_{l_2}^2 + \lambda TV(\mathbf{S}') + \gamma \|\mathbf{S}'\|_{l_1} \right\} \quad (5.2)$$

A solution \mathbf{S}' is found that minimizes the expression with respect to the chosen factors λ and γ . The first term fits a solution that should be close to the measured noisy data \mathbf{D} . The second term minimizes the gradients in the solution, making the solution smoother pixel-to-pixel. Finally, the last term aims to minimize the number of non-zero values in \mathbf{S}' , hence reducing overfitting. As this method is reducing the need for counts, it is promising both in acquiring fast spectra and also for low-dose applications (sensitive samples). Examples are shown in figure 5.1 where noisy spectra (points) are acquired and then filtered (lines of same color as their corresponding noisy spectra). This is compared to a spectrum of the same site (black) with realistic acquisition time (all spectra are normalized).

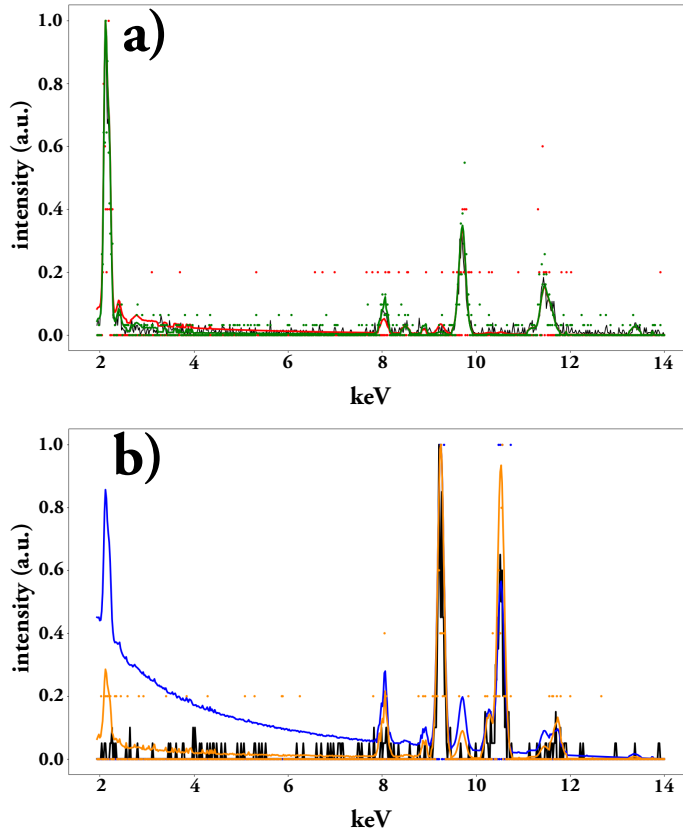


Figure 5.1: Two example spectra that have been filtered using the described method. The black curve is a longer acquisition of the same site while single points (noisy data) mark the raw measurements. The colored lines represent the filtered versions of the noisy data of the same color. a) shows the spectrum from a gold particle while b) shows GaAs. The noisy data consists of very few counts: green: 565 counts, red: 70 counts, orange: 83, and blue: 7, with deteriorating result of the filtered spectrum for fewer counts.

5.2 The method described in steps

In the ETEM, the experiment is set up by loading the sample of interest, heating it to the specified temperature and introducing the gasses. In the cases tested, Au nanoparticles were loaded onto the SiN_x windows of the heating chips, the sample heated to 420°C and TMGa, TMIIn and AsH_3 were introduced. The XEDS software was set up to collect spectrum images, one after the other (single frame) while intermittently checking for drift (which in this case is tracking the seed particle as it moves during growth and correcting via an autocorrelation function). All spectra are cut so that only energies between 1.94 and 14 keV are included. This includes all the peaks of interest without any contribution from Si or N (the SiN_x windows).

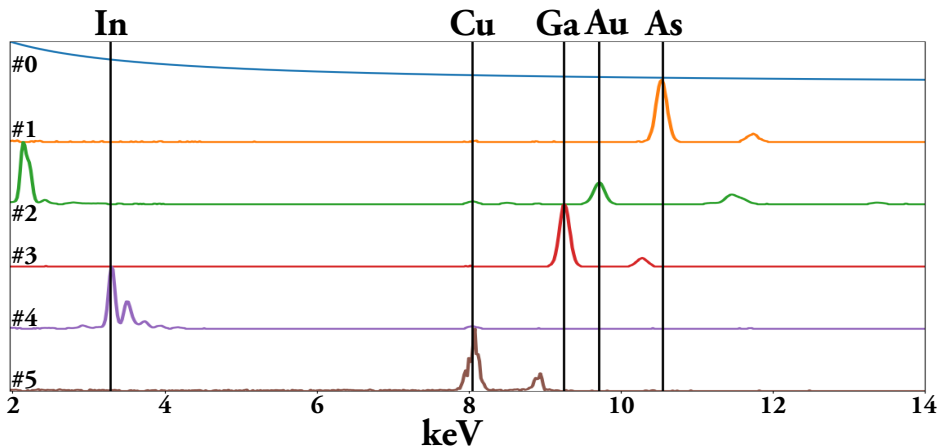


Figure 5.2: The 6 components used for filtering. Component 0 is a simulated background from Kramer’s law and the rest are extracted from NMF using long acquisitions of samples known to consist of the sought elements.

After the acquisition, the frames are run through the filtering script. First, the components L' are acquired from long-acquisition maps of the sample after the experiment or similar setups using the same materials (As, Au, Ga and In in the form of nanoparticles or nanowires on SiN_x windows in this example, components shown in figure 5.2) using NMF. The developed script performs the calculations on each frame:

- The frame is described as the contribution of each component in each pixel.
- The frame is described as S' , the components L' and the noisy measurement is D .
- The measured frame D can optionally be binned, both spatially (merging neighboring pixels) or temporally (merging frames) to increase number of counts.
- The minimization in equation 5.2 is performed using *CVXPY*, a minimization solver for Python [116, 117].
- The solution S' is then imaged and quantified using *Hyperspy*, a multidimensional data library for Python [118].

5.3 Simulations

In order to check if the quantification actually produces reliable results and offers an improvement, we performed two sets of simulations: Firstly, a 20×20 frame is simulated with a common spectrum in all pixels (As: 52.4, Au: 1.9, Ga: 18.9, In: 26.8 at%).

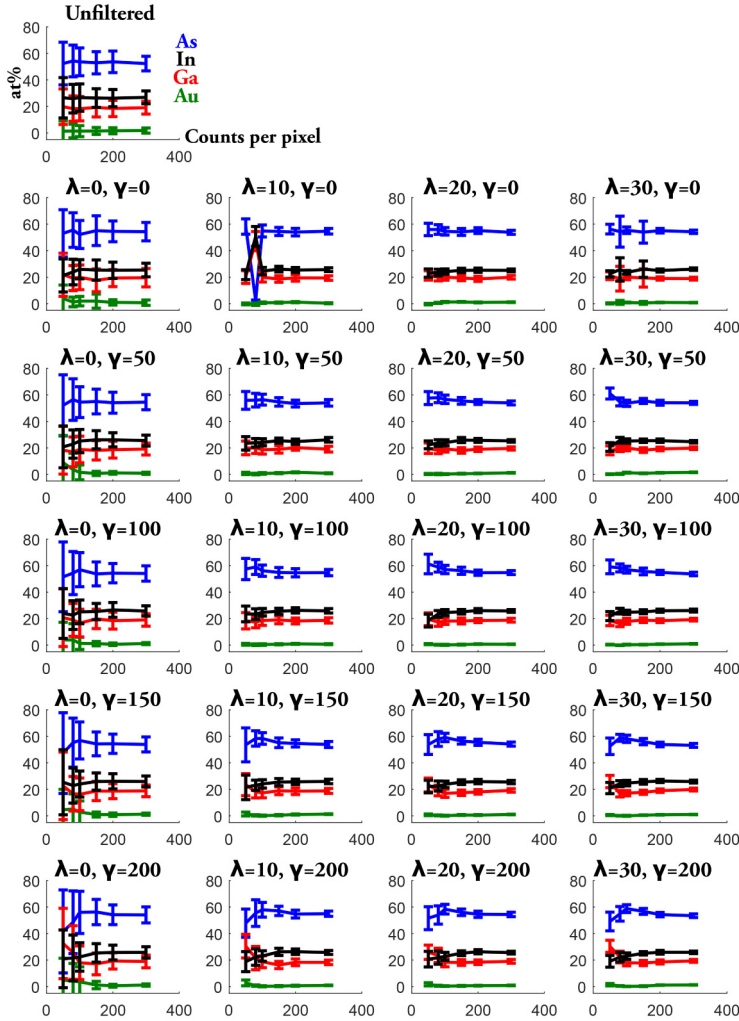


Figure 5.3: The quantification of a 20×20 frame as a function of number of counts per pixel. The error bars indicate the standard deviation of the pixels, which is reduced when the filtering method is applied. Different combinations of λ and γ are shown.

Each spectrum is randomly sampled from the distribution with a certain number of counts to create a simulated short acquisition spectrum in each pixel, which is then filtered and quantified. In figure 5.3 the distribution of the quantification for each frame is shown. The mean value is shown as a function of number of counts simulated and the error bars indicate the standard deviation. Secondly, a similar setup is used where instead three different regions make up the spectrum image, emulating a core-shell structure embedded in a matrix with very small differences in composition: a center region (As: 43.1, Au: 0.3, Ga: 56.5, In: 0.1 at%), shell-like struc-

5 Compositional mapping with short acquisitions

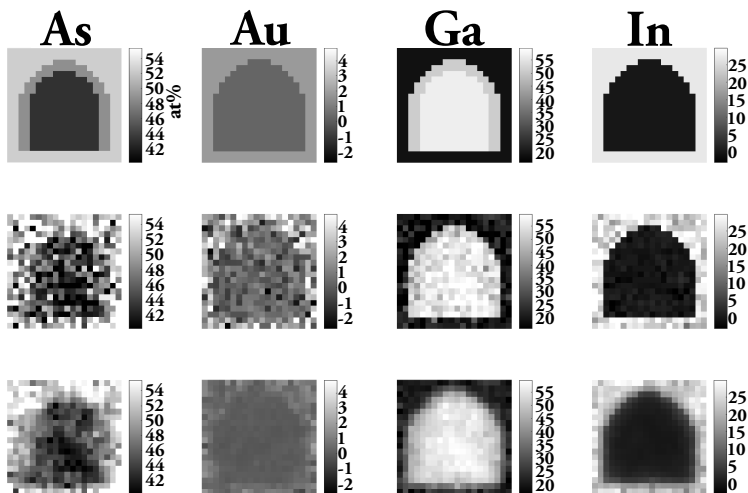


Figure 5.4: A simulated image with three regions with varying concentration of the four elements according to the grayscale and colorbar to the right of each image. The top row shows the reference case, the middle row shows the unfiltered and the bottom shows the case after applying the filtering method ($\lambda=10$, $\gamma=150$). Note that the colorbar is different for each element but the same for all three images of one element.

ture (As: 48.7, Au: 0.3, Ga: 50.9, In: 0.1 at%) and a background (As: 52.4, Au: 1.9, Ga: 18.9, In: 26.8 at%). These are sampled for 300 counts per pixel and the reference, unfiltered and filtered ($\lambda=10$, $\gamma=150$) images are shown in figure 5.4.

The sizes of the error bars in figure 5.3 are reduced drastically when the filtering method is applied, especially when increasing λ . This is expected since λ controls the smoothing and less variation should occur with more smoothing. However, already a low λ gives this effect. From these graphs it is concluded that around 150-300 counts are needed for a reliable quantification using the filtering method as the quantification flattens and the error bars are small (± 2 at%, with $\lambda=10$, $\gamma=50$, compared to ± 7 at% for the unfiltered, both for In using 150 counts). The effect of γ is not as drastic as for λ but using it makes the minimization often converge faster. The solution not converging can be a problem when using $\lambda > 0$ and $\gamma = 0$. Also in figure 5.4 the advantage of the filtering method can be seen. The smoothing is kept low so that distinct features such as the rounded top and sharp bottom corners can still be seen. The grayvalues of the filtered case match the reference very well, especially compared to the unfiltered case. Here the difference between regions can clearly be seen, even though the difference is small, e.g. for Au. The shell-like region is difficult to make clear, but for Ga it can faintly be observed (the grayvalue matching) but the smoothing almost hides it. The quantification of As ended up being a bit off, however, still better than the unfiltered case.

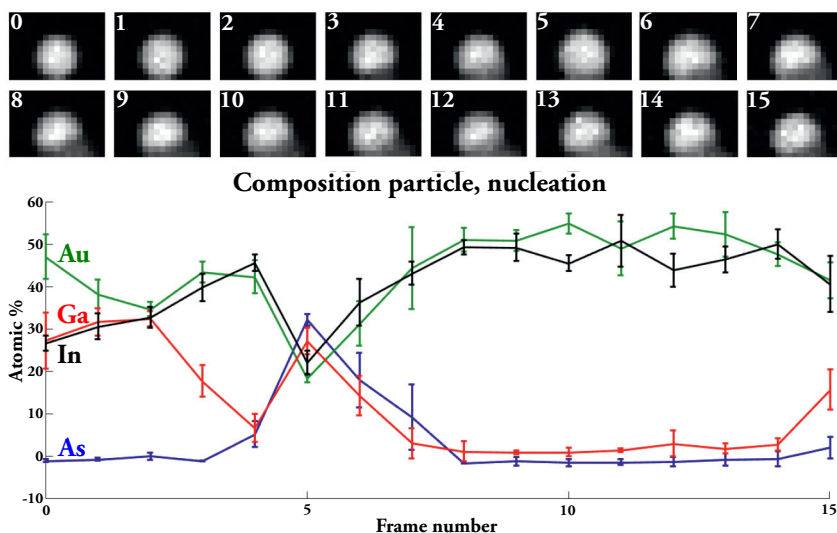


Figure 5.5: A nucleation event recorded by the short EDS-mapping. Pixel intensity depend on the number of x-ray counts per pixel. Spectrum images are then filtered, and the pixels of the seed particle are quantified for each frame, leading to a time-series of quantification both before and after the nucleation has occurred. Acquisition time per frame is 43s and $\lambda = 20$ and $\gamma = 200$.

5.4 Results and discussion of measurements

Firstly, a nucleation event was recorded where the initial Au nanoparticle was residing on the SiN_x window. It was heated to 420°C and initially TMIn and TMGa were inserted, which alloyed with the Au and turned it into a liquid droplet. After liquefying, no intentional supply of TMIn was used. However, In remained in the particle as the supply of AsH_3 started. The recorded frames (figure 5.5, frame intensity is based on number of x-ray counts in that pixel) show at first a high ($\sim 25\%$) Ga-concentration in the particle followed by the initial nucleation event (frame 3), where the Ga-concentration drops due to formation of GaAs. In and Au levels in the particle remain high while Ga is kept at a low level. Just after the initial nucleation the concentration of both Ga and As increase (frame 4-6 in figure 5.5). Since this is both Ga and As, it is believed that the newly formed GaAs has rotated into the line of projection (either above or below) of the liquid seed particle. The flow of TMGa was lowered after the initial nucleation as higher flows were used to quicker reach the supersaturation.

Secondly, a steadily growing (or so it seemed) wire was recorded, which produced data on how the conditions in the seed particle and the newly formed wire related to each other over time (figure 5.6). The wire is from the same batch that nucleated in the previous experiment, however not the same wire, and is fed TMGa (the flow

5 Compositional mapping with short acquisitions

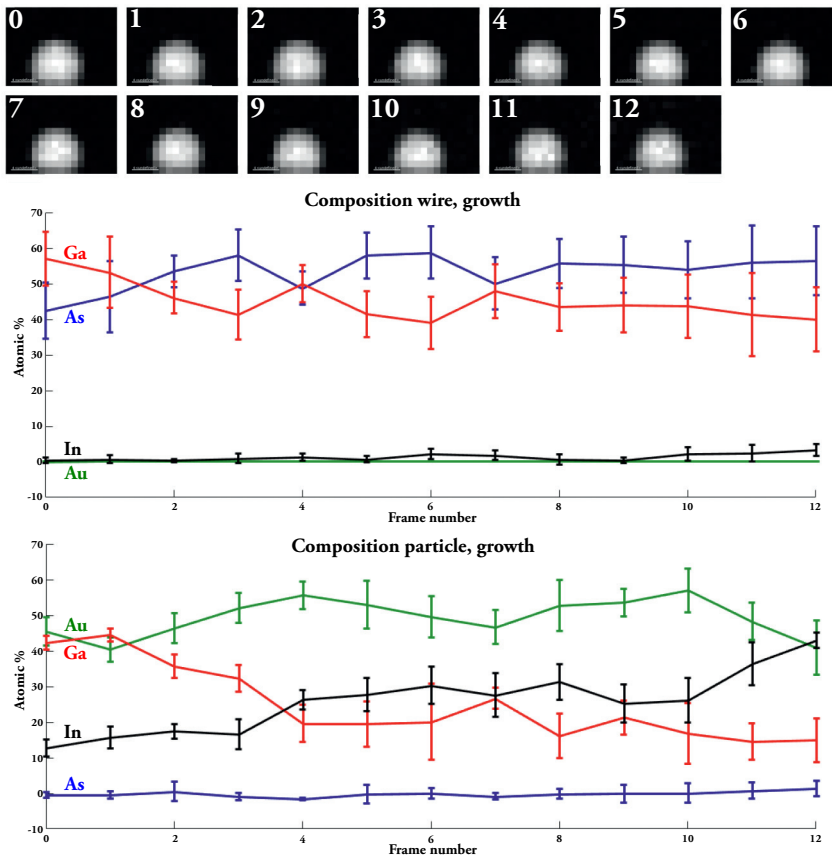


Figure 5.6: A presumed steadily growing wire where the composition can be monitored both in the catalyst and in the wire in parallel. Pixel intensity depend on the number of x-ray counts per pixel. The composition, and especially the Ga and In concentrations, differs between the wire and particle which shows how the incorporation of Ga into the wire is much larger than for In. Acquisition time per frame is 43s and $\lambda = 20$ and $\gamma = 200$.

is lowered during the acquisition) and AsH_3 at 420 °C. In is observed in the seed particle but in very low concentration in the resulting wire. Figure 5.6 shows how the In and Ga concentrations differs between the seed and wire during growth. Here, we are comparing the composition of two different areas at the same time, something not possible if the beam was just focused at one position. The Ga-concentration in the particle is constantly dropping during the acquired series due to the lowered supply of TMGa during the acquisition. Therefore, even though the growth appeared stable by observation, the composition in the particle was measured to changing gradually. However, this did not affect the concentration in the wire to a large extent.

For both these examples, the ideal number of counts per pixel was not known which resulted in that binning, both spatially and temporally, had to be used. $\lambda = 20$ and $\gamma = 200$ was used for both. This resulted in frame-times of about 43 s, which is non-ideal

for the potentially much faster transient events in the ETEM. During both of these growths it is possible that some unintentional TMIn was inserted due to it remaining in the gas-lines.

Later tests, after the simulations were performed, gave more information on the number of counts per pixel needed for a reliable quantification (150-300). This was used to optimize the acquisition, primarily using fewer pixels during acquisition. This reduced the acquisition time per frame down to 4 s with similar number of counts per pixel. Using some temporal binning for better quantification (acquisition time per frame: 16 s) another growth event was quantified with higher spatial resolution. $\lambda = 20$ and $\gamma = 700$ was used for this case. This time the flow of TMGa was increased substantially for a GaAs wire during growth (no TMIn added). The result is shown in figure 5.7, where the Ga-concentration steadily increases until the particle swells and falls off to its side (frame 34-37, the wire has kinked). This is followed by growth with another direction (towards top-left, frame 38-46) until it falls back on itself. Note that the In concentration is calculated to be zero throughout and that the sharp increase of Ga coincides with the kinking seen in the frames. In addition, some As can be seen in the particle, possibly from the grown GaAs being under/over the particle, especially when the wire folds back on itself. 5.6.

With the more optimized acquisition, it is shown that the acquisition time per frame could be lowered down to 4-16 seconds, with similar number of counts as deduced from the simulations. All in all, this filtering technique is promising for tracking transient events that need reliable composition with spatial resolution in the TEM. However, a drawback is the manual selection of the parameters λ and γ which can require much trial and error. Also, a choice in spatial vs. temporal resolution must be made in order to achieve enough counts per pixel at short times per frame. When these parameters are found, the technique can be used for comparing multiple regions at the same time (as in figure 5.6), detecting possible gradients or for mapping the composition as frames in a video. This is useful not just for studies of nanowires *in-situ* but also for other materials systems undergoing transitions.

5 Compositional mapping with short acquisitions

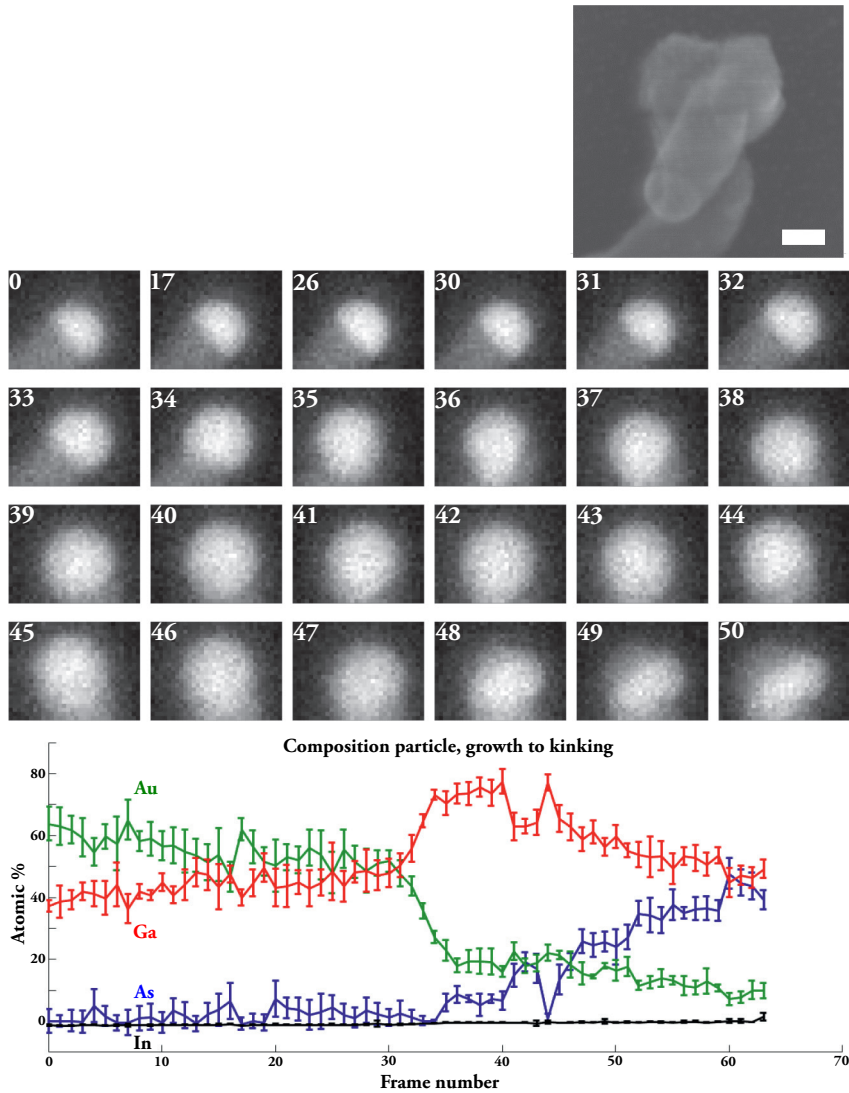


Figure 5.7: A nanowire kinking during growth. Pixel intensity depend on the number of x-ray counts per pixel. The composition of the particle is tracked during this event and shown in atomic percent as a function of frame number. Time per frame is 16 s and $\lambda = 20$ and $\gamma = 700$. At frame 34 the particle swells and falls off the wire front resulting in the first kinking event. This is followed by another kink which folds the wire on top of itself. After the growth, the wire is imaged using secondary electron STEM shown at the top (scalebar 20 nm).

Chapter 6

Discussion and outlook

In this chapter the presented introduction and theory from the previous chapters are related to the acquired data from the included papers (I to VII). The results will be presented by the papers in reverse order in an *increased* complexity, starting from HRTEM and compositional analysis where the crystal structure and compositional variations are analyzed for nanowires grown using Aerotaxy (papers VII and VI). This is followed by the addition of time-considerations of the growth, where nanowires *in-situ* are analyzed in the ETEM and the addition or removal of crystal planes is related to the composition in the seed particle (papers V, IV and III). Finally, the application of electron tomography on nanowires will be shown (papers II and I), followed by concluding remarks and an outlook.

6.1 High resolution and compositional data of nanowires

Papers VII and VI are similar in that they are studying the growth of nanowires using Aerotaxy (section 2.4). In paper VII, n-doping is achieved through adding TESn to the TMGa and AsH₃ mixture for growing GaAs nanowires. Increased added concentrations of the dopant precursor resulted in increased amount of incorporation into the wires. As the concentration is increased to the higher end however, the quality of the produced wires starts to deteriorate. Inspection through HRTEM concluded the crystal type to be ZB grown in $\langle 111 \rangle$ (as all the reported cases for Aerotaxy). Using the higher concentrations of TESn caused higher concentration of stacking faults (compare figures 6.1a and b). The stacking faults, seen as disruptions in the lattice, might be an indication that the growth is not perfectly stable. Also seen using HRTEM are indications of radial growth, as a layer of more disordered growth is ob-

6 Discussion and outlook

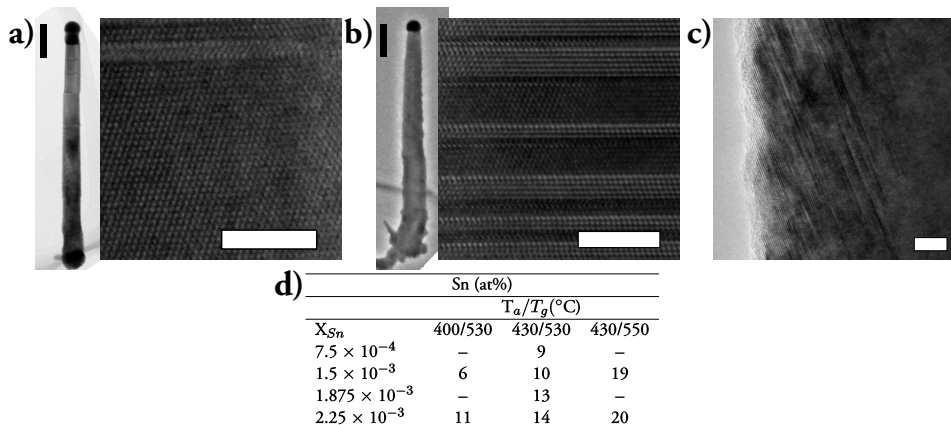


Figure 6.1: The increased Sn causes more stacking faults in the nanowires shown in a) for low precursor concentration and in b) for high. Also, for the higher concentrations, radial growth is seen, indicated in c) by the stacking faults seen at the edge of the wire. The final concentrations of Sn in the particles for the different growth conditions are seen in d). Scalebars are 200 nm for the overview images and 5 nm for the high magnification images.

served on the sides of the wire. Since the images are projections, the interpretations become difficult as this radial growth wraps the wire, but it can be distinguished by the non-ideal surface in figure 6.1c.

Due to the concentration of Sn in the wire ($10^{19} / \text{cm}^3 \approx 0.02 \text{ at}\%$) being below the detection limit of the XEDS-detector, the compositional analysis was focused on what was left behind in the seed particle. Since we were interested in seeing how much of the Sn actually was incorporated (dissociating from its precursor state and entering the catalytic particle) the study proved useful in seeing the temperature trends. Shown in the table in figure 6.1d the Sn incorporates as a function of both higher precursor molar fraction and higher growth temperature.

In paper VI the fine tuning of ternary (Ga, As and P) III–V semiconductor Aertotaxy nanowires was achieved through varying the precursor concentrations for the group V components. The flow of the III component (TMGa) was fixed while the ratio between PH_3 and AsH_3 was changed in order to correlate that ratio with what was actually incorporated into the formed wire. In addition, the temperature was altered to detect if it had any effect on the resulting composition in the wire. Figure 6.2b shows a compositional profile (of the wire in figure 6.2a, shown in counts, not at%) acquired along a wire, showing the constant composition along its axis. The XEDS analysis in combination with *photoluminescence* corroborated each other in the quantification, which led to an expression for x in the ternary description $\text{GaAs}_{1-x}\text{P}_x$:

$$x = \frac{\alpha X_g}{1 + X_g(\alpha - 1)} \quad (6.1)$$

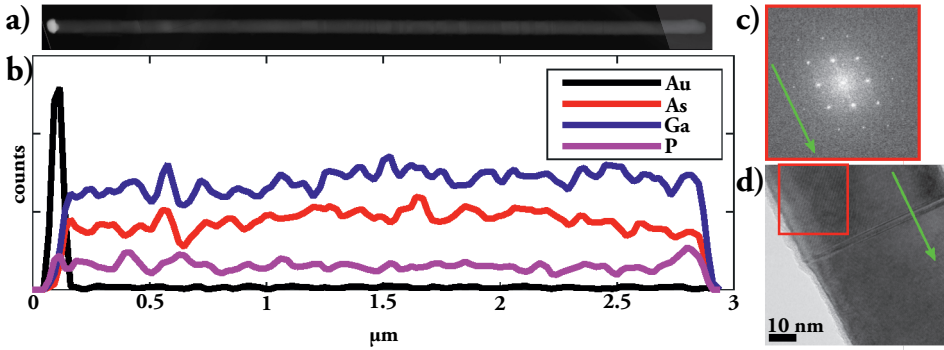


Figure 6.2: Compositional and HRTEM analysis of a GaAsP nanowire. a) TEM image of a nanowire and b) the XEDS signals (counts, not at%) along the length of the nanowire. The profile is achieved by mapping the whole wire followed by integrating the results across the wire. c) The FFT of the HRTEM image in d), which shows a ZB structure grown in the $\langle 111 \rangle$ direction (green arrow).

Where α is the ratio between the incorporation factors for P and As. X_g is the ratio of input gas fluxes ($\text{PH}_3/(\text{AsH}_3+\text{PH}_3)$) and α was determined to be 0.26 for this setup. For $X_g = 0.5$ this means that x becomes 0.2. The HRTEM images confirmed the crystal structure to be ZB and grown in a $\langle 111 \rangle$ -direction (see figure 6.2c and d).

All in all, the HRTEM and compositional analysis gave enough information to determine that the composition control and dopant incorporation for the grown wires were successful (however the exact dopant concentration was not achieved from XEDS). Also the structural quality of ZB wires grown in $\langle 111 \rangle$ were kept for the parameters used, with some deterioration at higher flows of TESn. The analysis hence answered the questions: Which elements form the wire, at what ratios and how do they arrange on an atomic scale? The Aerotaxy growth method is interesting since it produces wires at extremely high rates compared to conventional MOCVD. The wires sometimes have a rough *start*-end due to the lack of a guiding substrate. Looking at figure 6.2b there might be a hint of P being higher at that end (right side). Possibly the unstable conditions at this initial growth might favor a higher incorporation of P compared to the rest of the wire, something not studied further. This initial growth in Aerotaxy would be of interest to study systematically using an ETEM. Then the different parameters of temperature and gas pressures could be correlated to specific behaviors such as how the nucleation occurs, how quickly a preferred growth direction is found or composition in the particle and wire.

6.2 In-situ studies of nanowire growth

From papers VI and VII (especially VII where seed particle composition was measured after growth), it is clear that some data is not obtained when analyzing the wires post

6 Discussion and outlook

growth, after they have cooled down. For instance, details of how growth occurs and how the composition in the post-growth seed particle relates to the value during growth. Paper v focuses on the growth process of forming a layer of GaAs at the seed particle-wire interface. It is found, in contrast to previous assumptions, that the process is controlled by two steps: a collection of material in the particle: *incubation time*, and the formation of the layer: *layer completion time*. Since the time-resolution is around 0.05 s per frame it is possible to measure a *start* and *stop* of when the layer forms at this growth rate and compare these to the different conditions used. The incubation time and layer completion time as functions of TMGa and AsH₃, separately, are shown in figure 6.3.

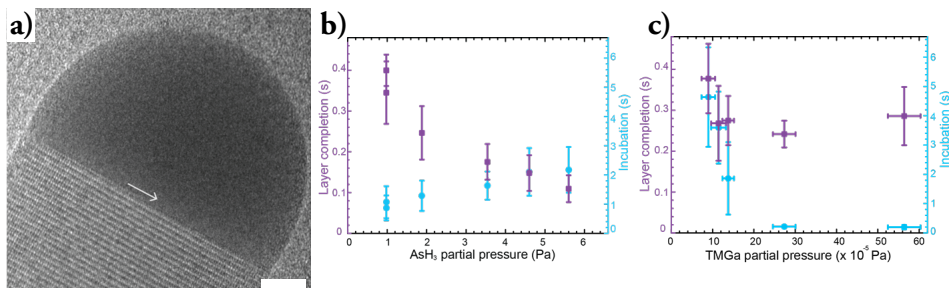


Figure 6.3: a) HRTEM frame of a growing NW with the growth-front of the layer marked by an arrow (scalebar: 5 nm). b) The layer completion time and incubation time as functions of AsH₃ partial pressure. c) The layer completion time and incubation time as functions of TMGa partial pressure.

It was expected for the growth-rate to increase when the flows were increased, as material would reach the seed particle quicker, hence reducing the incubation time. However, it was determined that the commonly assumed rate-limiting step of incubation time could actually be shorter than the layer completion-time and that these two times depended on the two components (Ga and As) separately. Since the solubility of As is low in the seed particle it will reach its equilibrium quickly and the incubation time is dictated by how quickly the Ga can reach the seed particle. On the other hand, the low concentration of As in the particle might limit how quickly the layer forms when it has started to form, possibly depleting the content of the particle and relying on how quickly more As can arrive.

Paper IV reports on the composition of the seed particle (also Au catalyzed GaAs) at different conditions during growth. XEDS was performed by focusing the beam at the site of interest (in this case the seed particle) and hence no spatial data was recorded during the composition measurement (compare to the project presented in chapter 5). Instead, the temperature and pressures are set, and the wire is allowed to equilibrate to these. Compositions are measured over a long period during which the conditions are stable. The Ga concentration is observed to increase with increased temperature and increased flux of TMGa, which also results in a higher growth rate

(both illustrated in figure 6.4). The growth rates of the wires were measured from the HRTEM images with short (0.05 s) acquisition time.

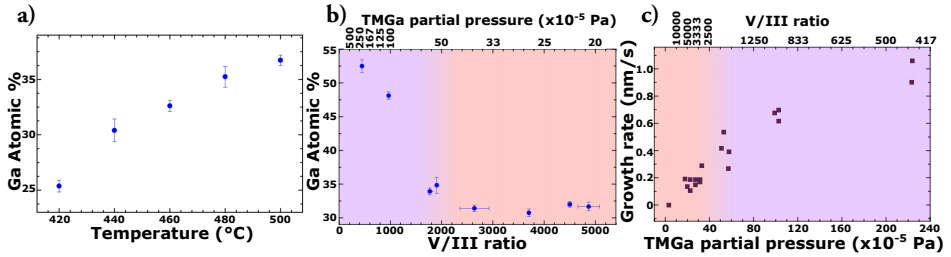


Figure 6.4: a) The Ga composition (at%) in the seed particle as a function of temperature during growth. b) The Ga composition as a function of V/III ratio during growth. c) The growth rate as a function of the TMGa partial pressure.

The composition was also measured in paper III. In this case, we studied the decomposition of the nanowire, i.e. the successive removal of layers. The effect of interest was how the activation energy for removal of a layer was lowered at the presence of the seed particle. This activation energy ($\Delta E = 116$ kJ/mol) was measured using the rate of removal at different temperatures which followed an Arrhenius expression. The equilibrium Ga concentration in the particle for a given temperature was found to increase with temperature (figure 6.5a). This resulted in transient periods just after changing the temperature when the particle is at non-equilibrium and the current chemical potential of Ga in the Au-Ga alloy dictates the removal rate from the wire. When increasing the temperature, the layer removal time is shorter and gradually increased to reach equilibrium (figure 6.5b) due to more Ga being needed to go into the particle. When decreasing (figure 6.5c), an initial increase in layer removal time is instead seen, followed by a decrease since the particle now has *too much* Ga in it.

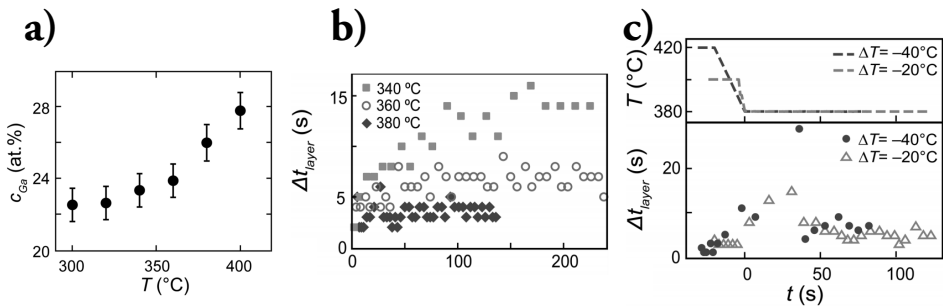


Figure 6.5: a) The Ga composition in the seed particle as a function of growth temperature. b) Time it takes to fully remove a layer for three different temperatures (increasing with 20 ° to the specified temperature). The x-axis is the time after temperature change and the y-axis the layer removal time in seconds. c) Time it takes to complete a layer as a function of time when the temperature is lowered.

The results show how powerful *in-situ* observations of nanowires in a TEM are, where their behavior during exposure to heat and chemicals can be recorded. With time-

resolution, and the possibility to correlate the data to certain conditions, the HRTEM and compositional data from the ETEM can give information about states otherwise missed. For example the transient events in figure 6.5b and c would be missed. Also rate dependent factors could be estimated directly from observations and not relying on *ex-situ* observations and assumptions.

6.3 Electron tomography of nanowires

In-situ TEM is undoubtedly useful in combining the regular detectors and imaging modes from TEM with the added dimension of time-resolution. However, in some cases projection images of nanowires are not enough to fully understand the structure unequivocally. The third spatial dimension needs to be reconstructed as well, which means electron tomography can be applied for these special cases of nanowires.

Paper II reports on the growth of kinetically tuned radial growth of AlSb onto an InAs core (grown WZ-ZB-WZ, axially in the growth direction). WZ AlSb, which otherwise prefers ZB, is formed by lowering the temperature of growth which prevents the adatoms to reach the thermodynamically favored ZB and instead forming a layer on the first grown WZ (as this is closer to the bottom of the wire, shorter diffusion length). The thickness of the WZ AlSb layer can then be tuned by adjusting the temperature, hence changing the diffusion length. However, from the projected TEM/STEM images the morphology was not unambiguously determined. Electron tomography was here used to reconstruct the shape of each layer in detail (including their interfaces), how they change in thickness and exposed facets along the wire, using the SIRT algorithm. HRTEM imaging was combined with the tomograms to deduct which crystallographic facets were seen.

Figure 6.6 clearly shows the internal morphology for two different wires grown with differing times of AlSb growth. 6.6a-c depicts a wire with the AlSb layer grown for longer than 6.6d-f. The denser InAs is seen as brighter than AlSb. Intensity depends on the projection images and since these are HAADF-STEM the intensity in each voxel depends on Z (or an average Z in the case of compounds). The AlSb is found to have different preferred facets compared to InAs. While the latter prefers $\{1\bar{1}00\}$, AlSb adopts $\{11\bar{2}0\}$ facets. This is especially clear if the two wires in figures 6.6a and 6.6d are compared. 6.6d apparently tried to adopt to this (starts changing preferred facets) but did not fully form. For the thicker wire the full change of preferred facets is clearly seen (compare figures 6.6b and e). Additional information (not included in the paper) on the outer layer (also InAs) could be found by measuring its thickness for the whole reconstructed tomogram. This data was reconstructed using CSET to additionally smooth for the segmentation and remove streaking effects. A colormap

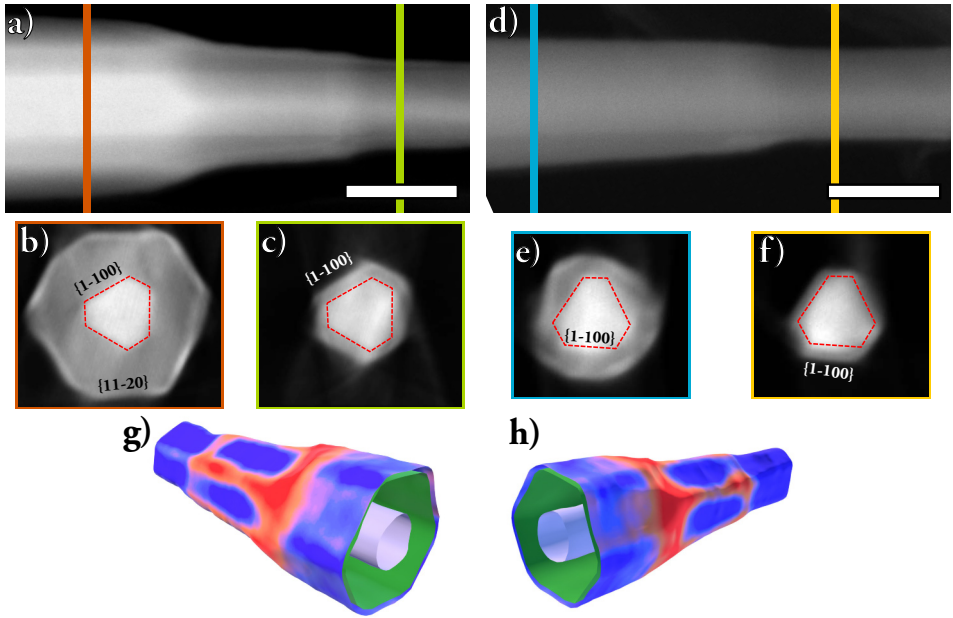


Figure 6.6: Tomographic reconstructions of two wires (paper II). In a)-c) the AlSb-shell has been growing for a longer time than for d)-f) (30 vs. 15 min), hence forming a thick AlSb-layer fully adapting to its preferred facets. g)-h) shows the same wire as in a)-c), here with a color coded surface indicating the thickness of the outermost InAs (thin to thick: blue to red).

in figure 6.6g and h (same wire as figure 6.6a-c) shows how the thickness varies from thick (red) to thin (blue), which indicates how the outer layer of InAs again tries to form its preferred facets and hence does not grow evenly.

Finally, paper I reports on surface features formed at the very high level of Sn-doping for GaAs wires grown by Aerotaxy. Here, the wires' surfaces had become covered by particles of unknown composition and with not completely random distribution. The projection images and compositional analysis provided information on the crystal structure (ZB, grown in $\langle 111 \rangle$) and that the particles were pure Ga. However, electron tomography was used to fully image the distribution of the particles on the surface. Using the SIRT algorithm (and also, but not included in the paper, DART) the wires grown using different concentrations of TESn were reconstructed and analyzed (figure 6.7). Data could be obtained on the tapering of the wire, distance from the seed particle to the first particle and the neck diameter. The data showed conclusively that the increased Sn caused more particles to form, larger tapering of the wires and particles positioned closer to the seed particles (smaller particle-free zone, indicating a reduced surface diffusion of Ga).

The in-house developed method of azimuthal mapping provided topological maps of the wires' surfaces and when correlated to the crystallography using single HRTEM

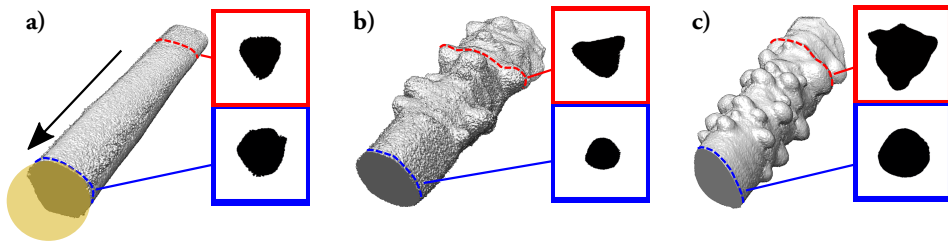


Figure 6.7: Tomograms of three wires with different Sn-doping. The cross-sections are shown for two sites for each wire and the surface particles can clearly be seen. The growth direction is towards the reader as indicated by the arrow.

images, the preferred positions of the particles could be found. The particles showed a preference for positions where $\{111\}$ B facets were found (threefold rotational symmetry, shown in the map in figure 6.8). This is the same facet polarity as the one in which the nanowires prefer to grow (V-terminated). Figure 6.8 shows both an azimuthal map with marked lines of preferred particle positions and crystallographic directions as well as a 3D drawing of a real case scenario with the particles on the preferred surfaces.

6.4 Conclusions

Coming to the conclusions of this thesis it is appropriate to relate back to the initial postulation on how the additional techniques of *in-situ* and tomographic application of transmission electron microscopy contribute to the understanding of nanowires. It is clear that *in-situ* measurements provide invaluable data on transient events and states not possible to record after growth. It was important for the determination of time dependencies of the two separate events (paper v) of incubation and layer completion time, which were not previously known. Additionally, if the method described in chapter 5 is used it is possible to correlate morphology to the composition as a function of position in the recorded frame.

When single projections of the nanowire are not conclusive enough, electron tomography provides the full 3D view, which can be a major benefit. In papers I and II the tomograms provide not only beautiful objects which one can observe from different angles, but also data on surface distribution, specific thicknesses, cross-sectional shapes, otherwise impossible to retrieve from single projections. In addition, the 3D data is possible to correlate to the other modes of the TEM (even though they are not used for the reconstruction), such as the HRTEM images and electron diffraction.

The acquisition of data made possible by *in-situ* and tomography aside, both ways of using the TEM data are demanding. They are time-consuming, require special setups,

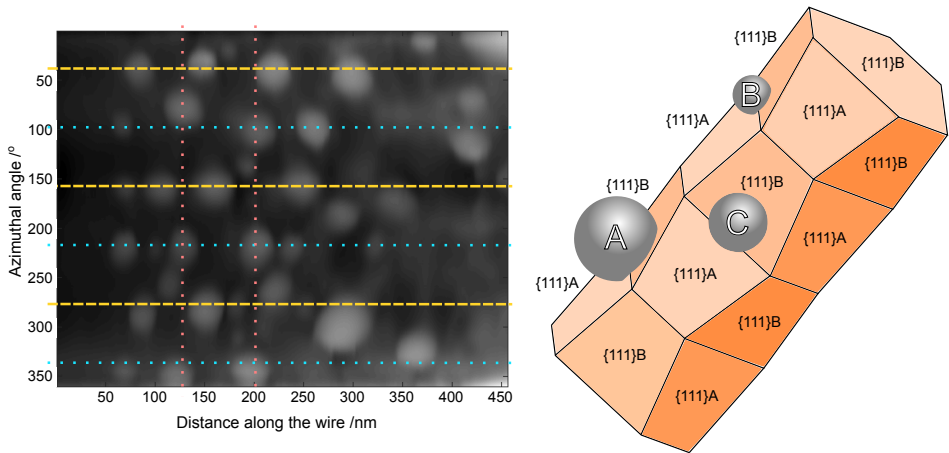


Figure 6.8: An azimuthal map showing the surface topology of a Sn-doped GaAs nanowire. The particles on the surface prefer certain crystallographic directions (yellow or blue lines) which were correlated to $\langle 211 \rangle$ directions of the ZB structure. Using HRTEM images for finding the crystallographic orientation, the particles were found to prefer to reside on $\{111\}B$ facets, which explains why there is a 60° rotation between the lines. Also, at a point along the wire the particles reside preferentially on the yellow or the blue lines (depending on the twinning direction at that point).

computing power and one or multiple expert operators, which can be unavailable or simply not possible on a large number of samples. Standard (single projection, *ex-situ*) use of TEM still provides large amounts of data, enough for most applications. The trend in microscopy sciences however is moving towards acquiring more and more data and correlative techniques such as these two fit right in. They can make use of different kinds of detectors and modes of operation in the TEM while adding either time-resolution or the third spatial dimension, which contribute to more data and clearer scientific results. The conclusion is therefore, maybe not unexpectedly, that both these techniques (*in-situ* and tomography using TEM) are extremely useful but only if applied on the types of nanowires and growth characteristics of nanowires that really require them. Hopefully, these two techniques will assist in understanding the complex cases of nanowires better, which in turn can result in brilliant innovations using them.

6.5 Outlook

Especially when analyzing nanowires using *in-situ* microscopy and tomography, I do not think it will ever be a problem finding additional aspects to investigate. Considering e.g. VLS-grown nanowires there is so much more to analyze, such as the behavior of the III-elements as they alloy with the metal particle. What concentration is needed in order to nucleate growth at different temperatures and how does this differ between the elements? As studied in chapter 5 (figure 5.5), In and Ga behave quite differently, in this case when combined. Similar combinations of multiple III-elements would also be interesting to study, finding which elements are preferentially forming the wire while the other remains in the particle (as for Ga and In respectively). Potentially, the addition of other components, such as dopants and how they change the nucleation conditions, would be interesting to study. For example, from paper 1 we know that the addition of TESn can affect the growth of GaAs, but how did the composition Au:Ga:Sn actually look during growth? As the surface diffusion of Ga was affected, was there any detectable Sn on the wire surface, that disappeared before *ex-situ* analysis? Some of these aspects have already been studied *ex-situ*, but *in-situ* investigations can further assist in understanding the processes, especially the composition as a function of time.

For the cases mentioned above, where composition is of interest, I see a benefit in using the elemental mapping from chapter 5, as it makes it possible to compare regions. The processes in figure 6.5, where layer removal rates temporarily changed, would be another interesting application of the mapping: to study the transient change in composition, not only the layer removal rate. Are there any gradients present in the particle when changing the conditions or during steady growth? The method itself could benefit from optimization in terms of how to get the most reliable quantification with as few counts as possible. More efficient detectors (e.g. larger collection angles) could also assist in producing more counts, hence making acquisition even shorter. Ideally, the method would benefit from more optimized choices of λ and γ , higher efficiency x-ray detectors and a small beam (high spatial resolution) with a dose producing enough signal but without affecting the sample. I think a technique such as this can help in better understanding the complex correlation between wire and particle in the future. In addition, the mapping algorithm has no limitations in the kind of spectroscopic data it uses, and could potentially also be applied to techniques such as EELS, x-ray photoelectron spectroscopy (XPS) or similar.

Tomography techniques, as they tell us about the third dimension, are useful for evaluating surfaces and interfaces. As the nanowire structures become more complex, I definitely see an application of tomography also in the future, especially when studying core-shell or other heterostructures. Higher resolution, as in atomically resolved

electron tomography, could then provide information on the atomic roughness of facets or compare interfaces with differing crystallographic directions. This could especially be interesting when studying how the nanowires interconnect with other parts of a larger electrical component, potentially needing sample preparation using FIB. Performing tomography *in-situ* (for instance by heating while acquiring multiple tilt-series) is also interesting as it combines *in-situ* with tomography and provide even more information, such as 3D melting behavior [119]. However, performing fast reliable tomographic acquisitions is not easy and in my experience, much better reconstructions are produced if the projection images are acquired in a slow and controlled manner. Using stable goniometers capable of performing the tilting and acquisition continuously, such as Vanropay et al. [119], what is considered "controlled manner" can be faster. However, I think that in most cases separate acquisitions (a time-resolved image-series and a couple of tomograms, one before, one after and potentially some during the experiment) would provide more useful information which can be correlated to each other. Separately these will have higher resolution in their respective domain, time and space, compared to producing something that finds a middle ground of acceptable resolution in both. This will of course change over time as optimizations of hardware and faster imaging algorithms will improve both resolutions.

References

- [1] E. Ruska and M. Knoll. “Die magnetische Sammelspule für schnelle Elektronenstrahlen.” *Z. techn. Phys.* 12 (1931), pp. 389–400.
- [2] D. B. Williams and C. B. Carter. *Transmission Electron Microscopy: A Textbook for Materials Science*. 2nd ed. Springer Science, 2009.
- [3] J. Wu, H. Shan, W. Chen, X. Gu, P. Tao, C. Song, W. Shang, and T. Deng. “In Situ Environmental TEM in Imaging Gas and Liquid Phase Chemical Reactions for Materials Research.” *Adv. Mater.* 28.44 (2016), pp. 9686–9712.
- [4] D. C. Martin and E. L. Thomas. “Experimental high-resolution electron microscopy of polymers.” *Polymer (Guildf)*. 36.9 (1995), pp. 1743–1759.
- [5] G. McMullan, A. Faruqi, D. Clare, and R. Henderson. “Comparison of optimal performance at 300 keV of three direct electron detectors for use in low dose electron microscopy.” *Ultramicroscopy* 147 (2014), pp. 156–163.
- [6] J. E. Evans, C. Hetherington, A. Kirkland, L.-Y. Chang, H. Stahlberg, and N. Browning. “Low-dose aberration corrected cryo-electron microscopy of organic specimens.” *Ultramicroscopy* 108 (2008), pp. 1636–1644.
- [7] D. Zhang, Y. Zhu, L. Liu, X. Ying, C.-E. Hsiung, R. Sougrat, K. Li, and Y. Han. “Atomic-resolution transmission electron microscopy of electron beam-sensitive crystalline materials.” *Science (80-.)*. 359.6376 (2018), pp. 675–679.
- [8] N. Yoshizawa, Y. Yamada, and M. Shiraishi. “TEM lattice images and their evaluation by image analysis for activated carbons with disordered microtexture.” *J. Mater. Sci.* 33 (1998), pp. 199–206.
- [9] M. Ziatdinov, O. Dyck, A. Maksov, X. Li, X. Sang, K. Xiao, R. R. Unocic, R. Vasudevan, S. Jesse, and S. V. Kalinin. “Deep Learning of Atomically Resolved Scanning Transmission Electron Microscopy Images: Chemical Identification and Tracking Local Transformations.” *ACS Nano* 11.12 (2017), pp. 12742–12752.

References

- [10] C. P. T. Svensson, T. Mårtensson, J. Trägårdh, C. Larsson, M. Rask, D. Hesselman, L. Samuelson, and J. Ohlsson. “Monolithic GaAs/InGaP nanowire light emitting diodes on silicon.” *Nanotechnology* 19.30 (2008), p. 305201.
- [11] M. S. Gudiksen, L. J. Lauhon, J. Wang, D. C. Smith, and C. M. Lieber. “Growth of nanowire superlattice structures for nanoscale photonics and electronics.” *Nature* 415.6872 (2002), pp. 617–620.
- [12] E. Memisevic, M. Hellenbrand, E. Lind, A. R. Persson, S. Sant, A. Schenk, J. Svensson, R. Wallenberg, and L.-E. Wernersson. “Individual Defects in InAs/InGaAsSb/GaSb Nanowire Tunnel Field- Effect Transistors Operating below 60 mV/decade.” *Nano Lett.* 17.7 (2017), pp. 4373–4380.
- [13] F. A. Ponce and D. P. Bour. “Nitride-based semiconductors for blue and green light-emitting devices.” *Nature* 386 (1997), pp. 351–359.
- [14] O.-P. Kilpi, J. Svensson, J. Wu, A. R. Persson, R. Wallenberg, E. Lind, and L.-E. Wernersson. “Vertical InAs/InGaAs Heterostructure Metal–Oxide–Semiconductor Field-Effect Transistors on Si.” *Nano Lett.* 17.10 (2017), pp. 6006–6010.
- [15] G. S. May and S. M. Sze. *Fundamentals of Semiconductor Fabrication*. 1st ed. John Wiley and Sons Inc., 2004.
- [16] K. A. Dick. “A review of nanowire growth promoted by alloys and non-alloying elements with emphasis on Au-assisted III–V nanowires.” *Prog. Cryst. Growth Charact. Mater.* 54 (2008), pp. 138–173.
- [17] A. Milnes and A. Polyakov. “Indium arsenide: a semiconductor for high speed and electro-optical devices.” *Mater. Sci. Eng. B* 18.3 (1993), pp. 237–259.
- [18] D. Danino. “Cryo-TEM of soft molecular assemblies.” *Curr. Opin. Colloid Interface Sci.* 17.6 (2012), pp. 316–329.
- [19] P. L. Stewart. “Cryo-electron microscopy and cryo-electron tomography of nanoparticles.” *Wiley Interdiscip. Rev. Nanomedicine Nanobiotechnology* 9.2 (2017).
- [20] J. Goldstein, D. E. Newbury, D. C. Joy, C. E. Lyman, P. Echlin, E. Lifshin, L. Sawyer, and J. R. Michael. *Scanning Electron Microscopy and X-ray Microanalysis*. 3rd ed. New York, NY: Springer, 2003.
- [21] M. H. F. Overwijk, F. C. van den Heuvel, and C. W. T. Bulle-Lieuwma. “Novel scheme for the preparation of transmission electron microscopy specimens with a focused ion beam.” *J. Vac. Sci. Technol. B Microelectron. Nanom. Struct. Process. Meas. Phenom.* 11.6 (1993), pp. 2021–2024.
- [22] M. Winey, J. B. Meehl, E. T. O’Toole, and T. H. Giddings. “Conventional transmission electron microscopy.” *Mol. Biol. Cell* 25.3 (2014), pp. 319–323.

- [23] D. F. Shriver and P. W. Atkins. *Inorganic Chemistry*. 3rd ed. Oxford: Oxford University Press, 1999.
- [24] L. E. Smart and E. A. Moore. *Solid State Chemistry: An Introduction*. 4th ed. Boca Raton, FL: CRC Press, 2012.
- [25] A. R. Persson. “Nanoscale electron tomography and compositional analysis of Aerotaxy nanowires.” Licentiate thesis. Lund University, 2018.
- [26] E. M. Conwell. “Properties of Silicon and Germanium.” *Proc. IRE* 40.11 (1952), pp. 1327–1337.
- [27] F. Yang, M. E. Messing, K. Mergenthaler, M. Ghasemi, J. Johansson, L. R. Wallenberg, M.-E. Pistol, K. Deppert, L. Samuelson, and M. H. Magnusson. “Zn-doping of GaAs nanowires grown by Aerotaxy.” *J. Cryst. Growth* 414 (2015), pp. 181–186.
- [28] R. Field and S. Ghandhi. “Doping of gallium arsenide in a low pressure organometallic CVD system: II. Hydrogen sulfide.” *J. Cryst. Growth* 74.3 (1986), pp. 551–558.
- [29] W. I. Wang, E. E. Mendez, T. S. Kuan, and L. Esaki. “Crystal orientation dependence of silicon dopning in molecular beam epitaxial AlGaAs/GaAs heterostructures.” *Appl. Phys. Lett* 47.8 (1985), pp. 826–828.
- [30] D. R. Askeland and P. P. Fulay. *Introduction to Materials Science and Engineering*. 2nd ed. Stamford: Cengage Learning, 2010.
- [31] F. Glas, J.-C. Harmand, and G. Patriarche. “Why Does Wurtzite Form in Nanowires of III-V Zinc Blende Semiconductors?” *Phys. Rev. Lett.* 99.14 (2007), p. 146101.
- [32] C.-Y. Yeh, Z. W. Lu, S. Froyen, and A. Zunger. “Zinc-blende - wurtzite polytypism in semiconductors.” *Phys. Rev. B* 46.16 (1992), p. 10086.
- [33] K. A. Dick, P. Caroff, J. Bolinsson, M. E. Messing, J. Johansson, K. Deppert, L. R. Wallenberg, and L. Samuelson. “Control of III-V nanowire crystal structure by growth parameter tuning.” *Semicond. Sci. Technol.* 25.2 (2010), p. 024009.
- [34] J. W. Faust and A. Sagar. “Effect of the Polarity of the III-V Intermetallic Compounds on Etching.” *J. Appl. Phys.* 31.2 (1960), pp. 331–333.
- [35] H. Barber and E. Heasell. “Polarity effects in III–V semiconducting compounds.” *J. Phys. Chem. Solids* 26.10 (1965), pp. 1561–1570.
- [36] M. De La Mata, R. R. Zamani, S. Martí-Sánchez, M. Eickhoff, Q. Xiong, A. Fontcuberta Morral, P. Caroff, and J. Arbiol. “The Role of Polarity in Non-planar Semiconductor Nanostructures.” *Nano Lett.* 19.6 (2019), pp. 3396–3408.

References

- [37] Y. Li, F. Qian, J. Xiang, and C. M. Lieber. “Nanowire electronic and optoelectronic devices.” *Mater. Today* 9.10 (2006), pp. 18–27.
- [38] R. Agarwal and C. Lieber. “Semiconductor nanowires: optics and optoelectronics.” *Appl. Phys. A* 85.3 (2006), pp. 209–215.
- [39] J. Wallentin, D. Jacobsson, M. Osterhoff, M. T. Borgström, and T. Salditt. “Bending and Twisting Lattice Tilt in Strained Core–Shell Nanowires Revealed by Nanofocused X-ray Diffraction.” *Nano Lett.* 17.7 (2017), pp. 4143–4150.
- [40] M. W. Larsson, J. B. Wagner, M. Wallin, P. Håkansson, L. E. Fröberg, L. Samuelson, and L. R. Wallenberg. “Strain mapping in free-standing heterostructured wurtzite InAs/InP nanowires.” *Nanotechnology* 18.1 (2007), p. 015504.
- [41] L. Samuelson. “Self-forming nanoscale devices.” *Mater. Today* 6.10 (2003), pp. 22–31.
- [42] R. R. LaPierre, A. C. E. Chia, S. J. Gibson, C. M. Haapamaki, J. Boulanger, R. Yee, P. Kuyanov, J. Zhang, N. Tajik, N. Jewell, and K. M. A. Rahman. “III-V nanowire photovoltaics: Review of design for high efficiency.” *Phys. status solidi - Rapid Res. Lett.* 7.10 (2013), pp. 815–830.
- [43] S. Lehmann, J. Wallentin, D. Jacobsson, K. Deppert, and K. A. Dick. “A general approach for sharp crystal phase switching in InAs, GaAs, InP, and GaP nanowires using only group V flow.” *Nano Lett.* 13.9 (2013), pp. 4099–4105.
- [44] D. Jacobsson, F. Panciera, J. Tersoff, M. C. Reuter, S. Lehmann, S. Hofmann, K. A. Dick, and F. M. Ross. “Interface dynamics and crystal phase switching in GaAs nanowires.” *Nature* 531 (2016), p. 317.
- [45] P. McIntyre and A. Fontcuberta i Morral. “Semiconductor Nanowires: To Grow or Not to Grow?” *Mater. Today Nano* 9 (2019), p. 100058.
- [46] R. S. Wagner and W. C. Ellis. “Vapor-liquid-solid Mechanism of Single Crystal Growth.” *Appl. Phys. Lett* 4 (1964), p. 89.
- [47] B. A. Wacaser, K. A. Dick, J. Johansson, M. T. Borgström, K. Deppert, and L. Samuelson. “Preferential Interface Nucleation: An Expansion of the VLS Growth Mechanism for Nanowires.” *Adv. Mater.* 21.2 (2009), pp. 153–165.
- [48] P. Caroff, K. A. Dick, J. Johansson, M. E. Messing, K. Deppert, and L. Samuelson. “Controlled polytypic and twin-plane superlattices in III – V nanowires.” *Nat. Nanotechnol.* 4.1 (2009), pp. 50–55.
- [49] S. C. Crawford, S. Ermez, G. Haberfehlner, E. J. Jones, and S. Gradečak. “Impact of nucleation conditions on diameter modulation of GaAs nanowires.” *Nanotechnology* 26.22 (2015), p. 225604.

- [50] M. Heurlin, M. H. Magnusson, D. Lindgren, M. Ek, L. R. Wallenberg, K. Deppert, and L. Samuelson. “Continuous gas-phase synthesis of nanowires with tunable properties.” *Nature* 492.7427 (2012), pp. 90–94.
- [51] W. Metaferia, A. R. Persson, K. Mergenthaler, F. Yang, W. Zhang, A. Yartsev, R. Wallenberg, M.-E. Pistol, K. Deppert, L. Samuelson, and M. H. Magnusson. “GaAsP Nanowires Grown by Aerotaxy.” *Nano Lett.* 16.9 (2016), pp. 5701–5707.
- [52] E. Barrigon, O. Hultin, D. Lindgren, F. Yadegari, M. H. Magnusson, L. Samuelson, L. I. M. Johansson, and M. T. Björk. “GaAs Nanowire pn-Junctions Produced by Low-Cost and High- Throughput Aerotaxy.” *Nano Lett.* 18.2 (2017), pp. 1088–1092.
- [53] W. Metaferia, S. Sivakumar, A. R. Persson, I. Geijselaers, L. R. Wallenberg, K. Deppert, L. Samuelson, and M. H. Magnusson. “n-type doping and morphology of GaAs nanowires in Aerotaxy.” *Nanotechnology* 29.28 (2018), p. 285601.
- [54] L. Reimer and H. Kohl. *Transmission Electron Microscopy*. 5th ed. New York, NY: Springer, 2008.
- [55] S. L. Bugby, L. K. Jambi, and J. E. Lees. “4D STEM: High efficiency phase contrast imaging using a fast pixelated detector.” *J. Phys. Conf. Ser.* 644.1 (2015).
- [56] R. Erni. “Aberrations.” *Aberration-Corrected Imaging Transm. Electron Microsc.* 2010. Chap. Aberration, pp. 189–228.
- [57] M. Haider, H. Rose, S. Uhlemann, E. Schwan, B. Kabius, and K. Urban. “A spherical-aberration-corrected 200kV transmission electron microscope.” *Ultramicroscopy* 75.1 (1998), pp. 53–60.
- [58] M. Haider, P. Hartel, H. Müller, S. Uhlemann, and J. Zach. “Current and future aberration correctors for the improvement of resolution in electron microscopy.” *Philos. Trans. R. Soc. A Math. Phys. Eng. Sci.* 367.1903 (2009), pp. 3665–3682.
- [59] L. Jones and P. D. Nellist. “Identifying and correcting scan noise and drift in the scanning transmission electron microscope.” *Microsc. Microanal.* 19.4 (2013), pp. 1050–1060.
- [60] S. J. Pennycook. “The impact of STEM aberration correction on materials science.” *Ultramicroscopy* 180 (2017), pp. 22–33.
- [61] J. Mayer, L. A. Giannuzzi, T. Kamino, and J. Michael. “TEM Sample Preparation and FIB-Induced Damage.” *MRS Bull.* 32.5 (2007), pp. 400–407.
- [62] S. M. Collins and P. A. Midgley. “Progress and opportunities in EELS and EDS tomography.” *Ultramicroscopy* 180 (2017), pp. 133–141.

References

- [63] M. Bosman, M. Watanabe, D. T. L. Alexander, and V. J. Keast. "Mapping chemical and bonding information using multivariate analysis of electron energy-loss spectrum images." *Ultramicroscopy* 106.11-12 (2006), pp. 1024–1032.
- [64] Y. Wu and P. Yang. "Direct observation of vapor-liquid-solid nanowire growth." *J. Am. Chem. Soc.* 123.13 (2001), pp. 3165–3166.
- [65] H. Tanaka, N. Hirashita, and R. Sinclair. "Kinetic analysis of the C49-to-C54 phase transformation in TiSi₂ thin films by in situ observation." *Jpn. J. Appl. Phys.* 37.8 (1998), pp. 4284–4287.
- [66] J. Li, J. Chen, H. Wang, N. Chen, Z. Wang, L. Guo, and F. L. Deepak. "In Situ Atomic-Scale Study of Particle-Mediated Nucleation and Growth in Amorphous Bismuth to Nanocrystal Phase Transformation." *Adv. Sci.* 5.6 (2018), p. 1700992.
- [67] Z. Zhang, N. Liu, L. Li, J. Su, P.-P. Chen, W. Lu, Y. Gao, and J. Zou. "In Situ TEM Observation of Crystal Structure Transformation in InAs Nanowires on Atomic Scale." *Nano Lett.* 18.10 (2018), pp. 6597–6603.
- [68] T. Yokota, M. Murayama, and J. M. Howe. "In situ Transmission-Electron-Microscopy Investigation of Melting in Submicron Al-Si Alloy Particles under Electron-Beam Irradiation." *Phys. Rev. Lett.* 91.26 (2003), p. 265504.
- [69] Y. Senda, K. Sasaki, and H. Saka. "Melting temperature of a wedge-shaped thin crystal of tin." *Philos. Mag.* 84.25-26 (2004), pp. 2635–2649.
- [70] J. A. Aguiar, S. Wozny, T. G. Holesinger, T. Aoki, M. K. Patel, M. Yang, J. J. Berry, M. Al-Jassim, W. Zhou, and K. Zhu. "In situ investigation of the formation and metastability of formamidinium lead tri-iodide perovskite solar cells." *Energy Environ. Sci.* 9.7 (2016), pp. 2372–2382.
- [71] M. Tornberg, D. Jacobsson, A. R. Persson, R. Wallenberg, K. A. Dick, and S. Kodambaka. "Kinetics of Au–Ga Droplet Mediated Decomposition of GaAs Nanowires." *Nano Lett.* 19.6 (2019), pp. 3498–3504.
- [72] R. Sarkar, C. Rentenberger, and J. Rajagopalan. "Electron Beam Induced Artifacts During in situ TEM Deformation of Nanostructured Metals." *Sci. Rep.* 5 (2015), p. 16345.
- [73] K. Hattar, J. Han, M. T. Saif, and I. M. Robertson. "In situ transmission electron microscopy observations of toughening mechanisms in ultra-fine grained columnar aluminum thin films." *J. Mater. Res.* 20.7 (2005), pp. 1869–1877.
- [74] K. S. Kumar, S. Suresh, M. F. Chisholm, J. A. Horton, and P. Wang. "Deformation of electrodeposited nanocrystalline nickel." *Acta Mater.* 51.2 (2003), pp. 387–405.

- [75] E. Spiecker, S. H. Oh, Z. W. Shan, Y. Ikuhara, and S. X. Mao. “Insights into fundamental deformation processes from advanced in situ transmission electron microscopy.” *MRS Bull.* 44.6 (2019), pp. 443–449.
- [76] Y. Zhao, Y. Tan, X. Ji, Z. Xiang, Y. He, and S. Xiang. “In situ study of cementite deformation and its fracture mechanism in pearlitic steels.” *Mater. Sci. Eng. A* 731 (2018), pp. 93–101.
- [77] J. B. Wagner, F. Cavalca, C. D. Damsgaard, L. D. Duchstein, and T. W. Hansen. “Exploring the environmental transmission electron microscope.” *Micron* 43.11 (2012), pp. 1169–1175.
- [78] C. Zhu, S. Liang, E. Song, Y. Zhou, W. Wang, F. Shan, Y. Shi, C. Hao, K. Yin, T. Zhang, J. Liu, H. Zheng, and L. Sun. “In-situ liquid cell transmission electron microscopy investigation on oriented attachment of gold nanoparticles.” *Nat. Commun.* 9.1 (2018), pp. 1–7.
- [79] D. Su. “Advanced electron microscopy characterization of nanomaterials for catalysis.” *Green Energy Environ.* 2.2 (2017), pp. 70–83.
- [80] P. Toth, D. Jacobsson, M. Ek, and H. Wiinikka. “Real-time, in situ, atomic scale observation of soot oxidation.” *Carbon N. Y.* 145 (2019), pp. 149–160.
- [81] M. Weyland, P. A. Midgley, and J. M. Thomas. “Electron Tomography of Nanoparticle Catalysts on Porous Supports: A New Technique Based on Rutherford Scattering.” *J. Phys. Chem. B* 105.33 (2001), pp. 7882–7886.
- [82] P. A. Midgley and M. Weyland. “3D electron microscopy in the physical sciences: the development of Z-contrast and EFTEM tomography.” *Ultramicroscopy* 96.3-4 (2003), pp. 413–431.
- [83] J. Frank. *Electron Tomography*. 2nd ed. New York, NY: Springer, 2006.
- [84] Z. Saghi and P. A. Midgley. “Electron Tomography in the (S)TEM: From Nanoscale Morphological Analysis to 3D Atomic Imaging.” *Annu. Rev. Mater. Res.* 42 (2012), pp. 59–79.
- [85] J. Radon. “Über die Bestimmung von Funktionen durch ihre Integralwerte längs gewisser Mannigfaltigkeiten.” *Berichte über die Verhandlungen der Königlich-Sächsischen Akad. der Wissenschaften zu Leipzig, Math. Klasse* 69 (1917), pp. 262–277.
- [86] J. Radon. “On the determination of functions from their integral values along certain manifolds.” *IEEE Trans. Med. Imaging* 5.4 (1986), pp. 170–176.
- [87] R. N. Bracewell. “Strip Integration In Radio Astronomy.” *Aust. J. Phys.* 9.2 (1956), pp. 198–217.
- [88] A. M. Cormack. “Representation of a Function by Its Line Integrals, with Some Radiological Applications.” *J. Appl. Phys.* 34.9 (1963), pp. 2722–2727.

References

- [89] J.-J. Fernandez. “Computational methods for electron tomography.” *Micron* 43.10 (2012), pp. 1010–1030.
- [90] J. R. Jinschek, K. J. Batenburg, H. A. Calderon, R. Kilaas, V. Radmilovic, and C. Kisielowski. “3-D reconstruction of the atomic positions in a simulated gold nanocrystal based on discrete tomography: Prospects of atomic resolution electron tomography.” *Ultramicroscopy* 108.6 (2008), pp. 589–604.
- [91] B. Goris, W. Van Den Broek, K. J. Batenburg, H. H. Mezerji, and S. Bals. “Electron tomography based on a total variation minimization reconstruction technique.” *Ultramicroscopy* 113 (2012), pp. 120–130.
- [92] Y. Chen, Y. Zhang, K. Zhang, Y. Deng, S. Wang, F. Zhang, and F. Sun. “FIRT: Filtered iterative reconstruction technique with information restoration.” *J. Struct. Biol.* 195.1 (2016), pp. 49–61.
- [93] R. Gordon, R. Bender, and G. T. Herman. “Algebraic Reconstruction Techniques (ART) for Three-dimensional Electron Microscopy and X-ray Photography.” *J. theor. Biol.* 29.3 (1970), pp. 471–481.
- [94] W. van Aarle, W. J. Palenstijn, J. De Beenhouwer, T. Altantzis, S. Bals, K. J. Batenburg, and J. Sijbers. “The ASTRA Toolbox: A platform for advanced algorithm development in electron tomography.” *Ultramicroscopy* 157 (2015), pp. 35–47.
- [95] W. van Aarle, W. J. Palenstijn, J. Cant, E. Janssens, F. Bleichrodt, A. Dabravolski, J. De Beenhouwer, K. J. Batenburg, and J. Sijbers. “Fast and flexible X-ray tomography using the ASTRA toolbox.” *Opt. Express* 24.22 (2016), pp. 25129–25147.
- [96] W. J. Palenstijn, K. J. Batenburg, and J. Sijbers. “Performance improvements for iterative electron tomography reconstruction using graphics processing units (GPUs).” *J. Struct. Biol.* 176.2 (2011), pp. 250–253.
- [97] R. Leary, P. A. Midgley, and J. M. Thomas. “Recent Advances in the Application of Electron Tomography to Materials Chemistry.” *Acc. Chem. Res.* 45.10 (2012), pp. 1782–1791.
- [98] P. A. Midgley and R. E. Dunin-Borkowski. “Electron tomography and holography in materials science.” *Nat. Mater.* 8.4 (2009), pp. 271–280.
- [99] A. Zürner, M. Döblinger, V. Cauda, R. Wei, and T. Bein. “Discrete tomography of demanding samples based on a modified SIRT algorithm.” *Ultramicroscopy* 115 (2012), pp. 41–49.
- [100] P. Gilbert. “Iterative Methods for the 3D reconstruction of an Object from Projections.” *J. Theor. Biol.* 36.1 (1972), pp. 105–117.

- [101] M.-h. Li, Y.-q. Yang, B. Huang, X. Luo, W. Zhang, M. Han, and J.-g. Ru. "Development of advanced electron tomography in materials science based on TEM and STEM." *Trans. Nonferrous Met. Soc. China* 24.10 (2014), pp. 3031–3050.
- [102] R. Leary, Z. Saghi, P. A. Midgley, and D. J. Holland. "Compressed sensing electron tomography." *Ultramicroscopy* 131 (2013), pp. 70–91.
- [103] M. Lustig, D. Donoho, and J. M. Pauly. "Sparse MRI: The application of compressed sensing for rapid MR imaging." *Magn. Reson. Med. An Off. J. Int. Soc. Magn. Reson. Med.* 58.6 (2007), pp. 1182–1195.
- [104] A. Kobayashi, T. Fujigaya, M. Itoh, T. Taguchi, and H. Takano. "Technical note: A tool for determining rotational tilt axis with or without fiducial markers." *Ultramicroscopy* 110.1 (2009), pp. 1–6.
- [105] T. Sanders, M. Prange, C. Akatay, and P. Binev. "Physically motivated global alignment method for electron tomography." *Adv. Struct. Chem. imaging* 1.1 (2015), pp. 1–11.
- [106] I. Arslan, J. R. Tong, and P. A. Midgley. "Reducing the missing wedge: High-resolution dual axis tomography of inorganic materials." *Ultramicroscopy* 106.11-12 (2006), pp. 994–1000.
- [107] N. Kawase, M. Kato, H. Nishioka, and H. Jinnai. "Transmission electron microtomography without the "missing wedge" for quantitative structural analysis." *Ultramicroscopy* 107 (2007), pp. 8–15.
- [108] C. Kübel, A. Voigt, R. Schoenmakers, M. Otten, D. Su, T.-C. Lee, A. Carlsson, and J. Bradley. "Recent Advances in Electron Tomography: TEM and HAADF-STEM Tomography for Materials Science and Semiconductor Applications." *Microsc. Microanal.* 11.5 (2005), pp. 378–400.
- [109] A. J. Koster, R. Grimm, D. Typke, R. Hegerl, A. Stoschek, J. Walz, and W. Baumeister. "Perspectives of Molecular and Cellular Electron Tomography." *J. Struct. Biol.* 120.3 (1997), pp. 276–308.
- [110] P. Burdet, Z. Saghi, A. N. Filippin, A. Borrás, and P. A. Midgley. "A novel 3D absorption correction method for quantitative EDX-STEM tomography." *Ultramicroscopy* 160 (2016), pp. 118–129.
- [111] J. Yuan, E. Bae, X.-C. Tai, and Y. Boykov. "A Study on Continuous Max-Flow and Min-Cut Approaches." *2010 IEEE Comput. Soc. Conf. Comput. Vis. Pattern Recognit.* 2010.
- [112] G. Haberfehlner, A. Orthacker, M. Albu, J. Li, and G. Kothleitner. "Nanoscale voxel spectroscopy by simultaneous EELS and EDS tomography." *Nanoscale* 6.23 (2014), pp. 14563–14569.

References

- [113] D. Rossouw, P. Burdet, F. de la Peña, C. Ducati, B. R. Knappett, A. E. H. Wheatley, and P. A. Midgley. “Multicomponent Signal Unmixing from Nanoheterostructures: Overcoming the Traditional Challenges of Nanoscale X-ray Analysis via Machine Learning.” *Nano Lett.* 15.4 (2015), pp. 2716–2720.
- [114] H. S. Seung and D. D. Lee. “Learning the parts of objects by non-negative matrix factorization.” *Nature* 401.6755 (1999), pp. 788–791.
- [115] X. Ying. “An Overview of Overfitting and its Solutions.” *J. Phys. Conf. Ser.* 1168.2 (2019), p. 22022.
- [116] S. Diamond and S. Boyd. “CVXPY: A Python-Embedded Modeling Language for Convex Optimization.” *J. Mach. Learn. Res.* 17.1 (2016), pp. 2909–2919.
- [117] A. Agrawal, R. Verschueren, S. Diamond, and S. Boyd. “A rewriting system for convex optimization problems.” *J. Control Decis.* 5.1 (2018), pp. 42–60.
- [118] F. de la Peña, E. Prestat, V. T. Fauske, P. Burdet, P. Jokubauskas, M. Nord, and A. Garmannslund. *HyperSpy v1.5.2*. 2019.
- [119] H. Vanrompay, E. Bladt, W. Albrecht, A. Béché, M. Zakhosheva, A. Sánchez-Iglesias, L. M. Liz-Marzán, and S. Bals. “3D characterization of heat-induced morphological changes of Au nanostars by fast: In situ electron tomography.” *Nanoscale* 10.48 (2018), pp. 22792–22801.
- [120] A. I. Kirkland and R. R. Meyer. ““Indirect” High-Resolution Transmission Electron Microscopy: Aberration Measurement and Wavefunction Reconstruction.” *Microsc. Microanal.* 10.4 (2004), pp. 401–413.
- [121] R. Meyer, A. Kirkland, and W. Saxton. “A new method for the determination of the wave aberration function for high resolution TEM: 1. Measurement of the symmetric aberrations.” *Ultramicroscopy* 92.2 (2002), pp. 89–109.

Scientific publications

My contributions

Paper I: Electron tomography reveals the droplet covered surface structure of nanowires grown by Aerotaxy

I did plan and lead the project as well as performed the electron microscopy and tomography. Also, I developed the 2D visualization technique of 3D rod samples (azimuthal mapping) and applied it to the samples. I also wrote the first draft of the manuscript.

Paper II: Kinetic engineering of wurtzite and zinc-blende AlSb shells on InAs nanowires

I did the tomographic reconstructions and related them to the crystallographic data obtained by conventional TEM, which solved the core-shell-shell structure. I also wrote the corresponding methods part and designed the corresponding figures and participated in writing of the manuscript.

Paper III: Kinetics of Au-Ga Droplet Mediated Decomposition of GaAs Nanowires

I participated in the *in-situ* measurements of the gold catalyst during decomposition in collaboration with MT and DJ, and participated in the writing of the manuscript.

Paper iv: In situ analysis of catalyst composition during gold catalyzed GaAs nanowire growth

I participated in the *in-situ* measurements of the gold catalyst during growth in collaboration with CBM, MT and DJ, and participated in the writing of the manuscript.

Paper v: Independent control of nucleation and layer growth in nanowires

I participated in the *in-situ* measurements of the nanowire growth in collaboration with CBM, MT and DJ, and participated in the writing of the manuscript.

Paper vi: GaAsP Nanowires Grown by Aerotaxy

I did the electron microscopy analysis of all samples, including investigation of crystallinity and crystallography as well as the compositional data of the wires. I wrote the corresponding methods and conclusions part, designed corresponding figures and participated in the writing of the remaining manuscript.

Paper vii: n-type doping and morphology of GaAs nanowires in Aerotaxy

I did the electron microscopy part of the project, analyzed all samples for their crystallographic structure and composition as a function of dopant concentration. I also wrote the corresponding methods part, designed the corresponding figures and participated in the writing of the remaining manuscript.

Appendix



Appendix A: Calculations of phase contrast in CTEM

This appendix is intended as a detailed explanation on the phase contrast of CTEM described a bit more briefly in section 3.3. Starting from what is finally recorded at the image the detected signal is the intensity of the collected electron wave:

$$I_i(\mathbf{r}') = |\psi_i(\mathbf{r}')|^2 = \psi_i(\mathbf{r}')\psi_i^*(\mathbf{r}') \quad (\text{A.1})$$

However, we know that the intensity will depend on how well the objective lens can transmit spatial frequencies (\mathbf{k}) since these will enter the lens differently. Hence, the expression is Fourier transformed (\mathcal{FT}) to be a function of \mathbf{k} :

$$\mathcal{I}_i(\mathbf{k}) = FT \left[I_i(\mathbf{r}') \right] \quad (\text{A.2})$$

So, what electron wave is reaching the image plane? The incoming wave of electrons is described as planar (parallel) and normalized as a function of \mathbf{r} on the object. A_ψ being amplitude and ϕ phase.

$$\psi_{in}(\mathbf{r}) = A_\psi(\mathbf{r})e^{i\phi(\mathbf{r})} = 1e^{i0} = 1 \quad (\text{A.3})$$

The sample is described as a projected potential $V_t(\mathbf{r})$ as a function of \mathbf{r} . For a thin sample an approximation is that no absorption occurs ($T(\mathbf{r}) = 1$) and that the sample potential causes a weak phase-shift to the wave ($e^{-i\sigma V_t(\mathbf{r})}$), σ being the interaction factor relating the potential to the phase shift. This approximation is called the *weak phase object approximation* (WPOA) and only holds for very thin samples [2, pp. 486-487]. The exiting wave is described as:

$$\psi_{out}(\mathbf{r}) = 1e^{i0} \cdot T(\mathbf{r})e^{-i\sigma V_t(\mathbf{r})} = e^{-i\sigma V_t(\mathbf{r})} \quad (\text{A.4})$$

If this exponential instead is described as a *Taylor expansion* and the higher order terms assumed very small (due to the phase shift $\sigma V_t(\mathbf{r})$ being small), the exiting wave can be described as:

$$\psi_{out}(\mathbf{r}) = e^{-i\sigma V_t(\mathbf{r})} \stackrel{\text{Taylor}}{=} 1 + (-i\sigma V_t(\mathbf{r})) + \frac{(-i\sigma V_t(\mathbf{r}))^2}{2!} + \dots \quad (\text{A.5})$$

$$\psi_{out}(\mathbf{r}) \approx 1 + (-i\sigma V_t(\mathbf{r})) = 1 + \psi_{out,s}(\mathbf{r}) \quad (\text{A.6})$$

This means the exiting wave is the direct wave ($\psi_{in}(\mathbf{r})$, which is equal to the incoming wave = 1) plus the scattered waves ($\psi_{out,s}(\mathbf{r})$). The waves are going to be affected by the objective lens depending on how far from the center they enter, which is a function of \mathbf{k} . The expression is hence Fourier transformed (as it would be going to the *back focal plane* (BFP) of the objective lens) and an *aperture function*, *dampening function* and an additional phase shift is introduced:

$$\Psi_{BFP}(\mathbf{k}) = \delta(\mathbf{k}) + A(\mathbf{k})D(\mathbf{k})e^{i\chi(\mathbf{k})}\Psi_{out,s}(\mathbf{k}) \quad (\text{A.7})$$

Continuing to the image plane, an inverse Fourier transform is performed and we get the image wave we were looking for from equation A.1:

$$\psi_i(\mathbf{r}') = \mathcal{FT}^{-1} \left[\Psi_{BFP}(\mathbf{k}) \right] = 1 + \psi_{i,s}(\mathbf{r}) \quad (\text{A.8})$$

Since we were interested in the intensity equation, A.1 is used and the approximation that the scattering is weak (in fact we still assume that all the intensity is left in the direct wave) leads to a final approximation, that the scattered beams are so weak in comparison to the direct beam that the interaction of scattered beams can be neglected:

$$\begin{aligned} I_i(\mathbf{r}') &= \psi_i(\mathbf{r}')\psi_i^*(\mathbf{r}') = (1 + \psi_{i,s}(\mathbf{r}))(1 + \psi_{i,s}^*(\mathbf{r})) \approx \\ &\approx 1 + \psi_{i,s}(\mathbf{r}) + \psi_{i,s}^*(\mathbf{r}) \end{aligned} \quad (\text{A.9})$$

This approximation makes the equation linear. A and D are assumed even and Ψ even or odd for \mathbf{k} . \hat{V}_t is the projected potential in the specified point \mathbf{r} :

$$\begin{aligned} \mathcal{I}_i(\mathbf{k}) &= \mathcal{FT} \left[I_i(\mathbf{r}') \right] = \\ &= \delta(\mathbf{k}) + A(\mathbf{k})D(\mathbf{k})e^{i\chi(\mathbf{k})}\Psi_{out,s}(\mathbf{k}) + \\ &+ A(-\mathbf{k})D(-\mathbf{k})e^{-i\chi(-\mathbf{k})}\Psi_{out,s}^*(-\mathbf{k}) \end{aligned} \quad (\text{A.10})$$

$$\begin{aligned} \mathcal{I}_i(\mathbf{k}) &= \\ &= \delta(\mathbf{k}) + \Psi_{out,s}(\mathbf{k})\hat{V}_t A(\mathbf{k})D(\mathbf{k}) \left(e^{i\chi(\mathbf{k})} - e^{-i\chi(-\mathbf{k})} \right) = \\ &= \delta(\mathbf{k}) + (-i\sigma\hat{V}_t)A(\mathbf{k})D(\mathbf{k}) \cdot \\ &\cdot \left(\cos(\chi(\mathbf{k})) + i\sin(\chi(\mathbf{k})) - \right. \\ &\left. - \cos(-\chi(-\mathbf{k})) - i\sin(-\chi(-\mathbf{k})) \right) = \\ &= \delta(\mathbf{k}) - i\sigma\hat{V}_t A(\mathbf{k})D(\mathbf{k}) \left(2i\sin(\chi(\mathbf{k})) \right) \end{aligned} \quad (\text{A.11})$$

$$\mathcal{I}_i(\mathbf{k}) = \delta(\mathbf{k}) + 2\sigma\hat{V}_t A(\mathbf{k})D(\mathbf{k})\sin(\chi(\mathbf{k})) \quad (\text{A.12})$$

I.e. the projected potential \hat{V}_t in point \mathbf{r} on the sample is contributing to the image contrast in a point \mathbf{r}' at the image as a function of $\chi(\mathbf{k})$, where \mathbf{k} is the spatial frequency [2, 120, 121].

Appendix B: Aberrations in a TEM

Table B.1: Reference table of different aberrations including their coefficient symbol, symmetry and the factor to be summed (how it scales with ω). $\bar{\omega}$ notates the conjugate of ω . Table from [56]

Aberration name	Variable	Value	Symmetry	Aberration factor
Beam/Image Shift	A_0	complex	1	$A_0\bar{\omega}$
Defocus	C_1	real	0	$\frac{1}{2}C_1\omega\bar{\omega}$
Twofold Astigmatism	A_1	complex	2	$\frac{1}{2}A_1\bar{\omega}^2$
Second-order axial coma	B_2	complex	1	$B_2\omega^2\bar{\omega}$
Threefold Astigmatism	A_2	complex	3	$\frac{1}{3}A_2\bar{\omega}^3$
Third-order spherical aberration	C_3	real	0	$\frac{1}{4}C_3(\omega\bar{\omega})^2$
Third-order star-aberration	S_3	complex	2	$S_3\omega^3\bar{\omega}$
Fourfold astigmatism	A_3	complex	4	$\frac{1}{4}A_3\bar{\omega}^4$
Fourth-order axial coma	B_4	complex	1	$B_4\omega^3\bar{\omega}^2$
Fourth-order three-lobe aberration	D_4	complex	3	$D_4\omega^4\bar{\omega}$
Fivefold astigmatism	A_4	complex	5	$\frac{1}{5}A_4\bar{\omega}^5$
Fifth-order spherical aberration	C_5	real	0	$\frac{1}{6}C_5(\omega\bar{\omega})^3$
Fifth-order star-aberration	S_5	complex	2	$S_5\omega^4\bar{\omega}^2$
Fifth-order rosette aberration	R_5	complex	4	$R_5\omega^5\bar{\omega}$
Sixfold astigmatism	A_5	complex	6	$\frac{1}{6}A_5\bar{\omega}^6$
Sixth-order axial coma	B_6	complex	1	$B_6\omega^4\bar{\omega}^3$
Sixth-order three-lobe aberration	D_6	complex	3	$D_6\omega^5\bar{\omega}^2$
Sixth-order pentacle aberration	F_6	complex	5	$F_6\omega^6\bar{\omega}$
Sevenfold astigmatism	A_6	complex	7	$\frac{1}{7}A_6\bar{\omega}^7$
Seventh-order spherical aberration	C_7	real	0	$\frac{1}{8}C_7(\omega\bar{\omega})^4$
Seventh-order star-aberration	S_7	complex	2	$S_7\omega^5\bar{\omega}^3$
Seventh-order rosette aberration	R_7	complex	4	$R_7\omega^6\bar{\omega}^2$
Seventh-order chaplet aberration	G_7	complex	4	$G_7\omega^7\bar{\omega}$
Eightfold astigmatism	A_7	complex	8	$\frac{1}{8}A_7\bar{\omega}^8$

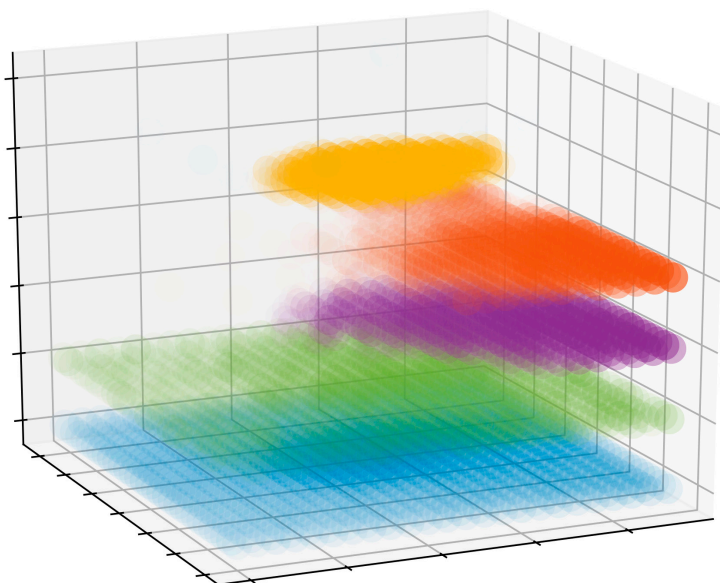
Appendix C: Matlab code for visualizing $\sin(\chi)$

```
1 function chi = aberrationCorrection(aberrations)
2 %Function that takes a vector of the aberration-values and ...
   plots a surface-plot of sin(X)
3 %The inputted vector: 'aberrations' has the dimensions (24,2)
4 %The order is from A0 to A7 according to the table given in ...
   Erni 2010, with the first value being the absolute ...
   number and the second the angle in degrees
5
6 %Changable parameters
7 r = 14; %mm-1, maximum r calculated
8 resolution = 50; %how many points per r in the mesh
9 lambda = 0.001968697; %nm, wavelength of electron
10 %Example: 0.001968697 for 300keV and 0.002507866 for 200 keV
11
12 %Read the inputted aberration factors, all in nm, and make ...
   them complex
13 for k = 1:24
14     abFactors(k) = ...
        aberrations(k,1)*exp(1i*2*pi/360*aberrations(k,2));
15 end
16
17 %Create the complex mesh to plot
18 kValues = zeros(r*resolution*2+1);
19 for a = 1:r*resolution*2+1
20     for b = 1:r*resolution*2+1
21         kValues(a,b) = (a/resolution-1/resolution-r)+...
            (b/resolution-1/resolution-r)*1i;
22     end
23 end
24 end
25
26 %Calculate each aberration component
27 A0_result = abFactors(1)*lambda.*conj(kValues);
28 C1_result = 1/2*abFactors(2)*lambda^2.*kValues.*conj(kValues);
29 A1_result = 1/2*abFactors(3)*lambda^2.*conj(kValues).^2;
30 B2_result = abFactors(4)*lambda^3.*kValues.^2.*conj(kValues);
31 A2_result = 1/3*abFactors(5)*lambda^3.*conj(kValues).^3;
32 C3_result = ...
    1/4*abFactors(6)*lambda^4.*kValues.^2.*conj(kValues).^2;
33 S3_result = abFactors(7)*lambda^4.*kValues.^3.*conj(kValues);
34 A3_result = 1/4*abFactors(8)*lambda^4.*conj(kValues).^4;
35 B4_result = ...
    abFactors(9)*lambda^5.*kValues.^3.*conj(kValues).^2;
36 D4_result = abFactors(10)*lambda^5.*kValues.^4.*conj(kValues);
37 A4_result = 1/5*abFactors(11)*lambda^5.*conj(kValues).^5;
38 C5_result = ...
    1/6*abFactors(12)*lambda^6.*kValues.^3.*conj(kValues).^3;
```

```

39 S5_result = ...
    abFactors(13)*lambda^6.*kValues.^4.*conj(kValues).^2;
40 R5_result = abFactors(14)*lambda^6.*kValues.^5.*conj(kValues);
41 A5_result = 1/6*abFactors(15)*lambda^5.*conj(kValues).^6;
42 B6_result = ...
    abFactors(16)*lambda^7.*kValues.^4.*conj(kValues).^3;
43 D6_result = ...
    abFactors(17)*lambda^7.*kValues.^5.*conj(kValues).^2;
44 F6_result = abFactors(18)*lambda^7.*kValues.^6.*conj(kValues);
45 A6_result = 1/7*abFactors(19)*lambda^7.*conj(kValues).^7;
46 C7_result = ...
    1/8*abFactors(20)*lambda^8.*kValues.^4.*conj(kValues).^4;
47 S7_result = ...
    abFactors(21)*lambda^8.*kValues.^5.*conj(kValues).^3;
48 R7_result = ...
    abFactors(22)*lambda^8.*kValues.^6.*conj(kValues).^2;
49 G7_result = abFactors(23)*lambda^8.*kValues.^7.*conj(kValues);
50 A7_result = 1/8*abFactors(24)*lambda^8.*conj(kValues).^8;
51
52 %calculated vectors
53 W = real(A0_result+C1_result+A1_result+B2_result+...
54     A2_result+C3_result+S3_result+A3_result+...
55     B4_result+D4_result+A4_result+C5_result+...
56     S5_result+R5_result+A5_result+B6_result+...
57     D6_result+F6_result+A6_result+C7_result+...
58     S7_result+R7_result+G7_result+A7_result);
59 chi = 2*pi/lambda*W;
60 realVec = real(kValues);
61 imVec = imag(kValues);
62 sinusChi = sin(chi);
63
64 %plot
65 figure();
66 hold on
67 surf(realVec,imVec,sinusChi,'EdgeColor','none');
68 xlabel('\bf{k_x}');
69 ylabel('\bf{k_y}');
70 zlabel('\bf{sin(\chi(k))}');
71 view(15,85);
72 hold off;

```

The topic of this thesis is to study semiconducting nanowires using transmission electron microscopy. More information about the samples is gained by acquiring multidimensional data such as spatial 3D, time and spectroscopy

... here presented in 2D.